Analysis of a Nonlinear vibration absorber for vibration control in a hand-held impact machine

Oreoluwa Alabi

Dissertation submitted to the Faculty of the
Virginia Polytechnic Institute and State University
in partial fulfillment of the requirements for the degree of

Doctor of Philosophy
in
Engineering Mechanics

Oumar Barry, Chair
Nicole Abaid
Bahareh Behkam
Romesh Batra

September 26, 2025
Blacksburg, Virginia

Analysis of a Nonlinear vibration absorber for vibration control in a hand-held impact machine

Oreoluwa Alabi

(ABSTRACT)

Hand-held impact machines (HIMs), such as jackhammers and chipping hammers, operate through the repetitive impacts of a percussive mechanism. Due to their widespread use, it is essential that these tools are designed for safe daily operation. This need is underscored by the fact that approximately 20% of operators risk developing vibration-related hand injuries, which can be career-ending. As a step toward improving the safety of these tools, this dissertation focuses on modeling their dynamic behavior to evaluate the effectiveness of vibration control strategies. The novelty of this work lies in the use of nonlinear mass–spring–damper models to describe tool dynamics, coupled with lumped-mass models of the hand–arm system. Traditionally, linear models have been employed for such evaluations; by contrast, this study introduces nonlinear modeling to capture the more realistic dynamics of HIMs. Furthermore, the role of a cubic nonlinear absorber in attenuating vibrations transmitted to the hand is systematically investigated through this framework. Key findings include the observation of nonlinear phenomena such as unstable periodic solutions, quasi-periodicity, chaos, and grazing. Frequency response analyses demonstrate the superiority of the cubic absorber over its linear counterpart, with notable improvements in performance when combined with an inerter. Parametric studies further reveal how the absorber can be tuned to enhance vibration attenuation across different nonlinear HIM models.

Analysis of a Nonlinear vibration absorber for vibration control in a hand-held impact machine

Oreoluwa Alabi

(GENERAL AUDIENCE ABSTRACT)

Hand-held impact machines like jackhammers and chipping hammers are widely used in construction, mining and manufacturing but can expose workers to harmful vibrations. Long-term use can cause hand–arm vibration syndrome (HAVS), a condition affecting nearly 20% of operators and leading to pain, loss of grip, and even permanent disability. This dissertation develops mathematical models to better understand how these vibrations occur and how they can be reduced. Unlike traditional studies that rely on simplified linear models, this work uses nonlinear models that more accurately capture the complex dynamics of impact tools and their interaction with the hand–arm system. A special focus is placed on testing cubic nonlinear absorbers — devices designed to counteract vibrations. Results show that these absorbers can outperform standard designs, especially when combined with an inerter element, and offer pathways for safer tool design. Ultimately, this work aims to guide engineering solutions that reduce injuries and extend worker careers.

Dedication

To my parents Adesola and Modupe Alabi

Acknowledgments

I am grateful to my advisor, Dr. Oumar Barry, who has helped me and given me the motivation to keep pushing and exploring the boundaries of research. I cannot express how much his advocacy and encouragement for my various endeavors have helped me. I am also very thankful to Dr. Sunit Kumar Gupta, who has continually provided support and much-needed technical insights through our discussions. I am grateful as well to my committee members — Dr. Behkam, Dr. Abaid, and Dr. Batra — who have been instrumental in refining the ideas presented in this dissertation. Last but certainly not least, I would like to thank my VibroLab teammates, whose camaraderie, encouragement, and collaborative spirit have helped ease the rougher edges of research.

Contents

List of Figures

Chapter 1

Introduction

This chapter was collaboratively developed by the following authors: **Ore Alabi**, **Dr. Sunit Kumar Gupta**, and **Dr. Oumar Barry**.

- **Conceptualization:** Ore Alabi, Dr. Oumar Barry
- **Writing – Original Draft:** Ore Alabi
- **Writing – Review & Editing:** Dr. Oumar Barry, Dr. Sunit Kumar Gupta
- **Supervision:** Dr. Oumar Barry

1.1 Overview

The mitigation of hand-arm vibrations (HAV) transmitted from power tools to the hand is crucial to prevent the onset of a disease termed hand-arm vibration syndrome (HAVS). This dissertation explores a passive vibration control method aimed at reducing dangerous vibration levels transmitted to the hand from power tools.

The need to reduce harmful vibrations becomes more pressing when considering the widespread use of power tools in industries such as mining, airplane manufacturing, and construction [1–4]. Approximately 20% of workers exposed to hand-transmitted vibration (HTV) from tools like impact screwdrivers and chipping hammers are at risk of developing finger blanching, a symptom of HAVS [5], making vibration reduction a critical objective.

To mitigate harmful vibrations transmitted to the hand, this dissertation focuses on curbing vibrations produced by the chipping hammer. Predicting vibrations from such tools is essential in understanding the underlying methods by which vibrations from the tool can be curbed. A conventional method often used to study the human-tool interaction is a linear vibration lumped parameter model [6–9]. As a departure from this conventional method, these dissertation will focus on creating more realistic chipping hammer model by including cubic and vibroimpact nonlinearities in the lumped parameter model to predict the behavior of the chipping hammer has as been widely used in literature to replicate the dynamics of percussive tools. [10–18].

After modeling the dynamic interaction within the tool, a lumped parameter model of the hand-arm system is also employed to monitor the effects of vibrations transmitted from the chipping hammer. The lumped mass model of the hand-arm is anatomically similar to the hand's clamp-like structure [19, 20] and is used in this study to assess the impact of vibrations.

With the tool and hand-arm models defined, the next focus is on evaluating the efficacy of passive vibration control methods. One common method is the tuned vibration absorber, which can suppress vibration amplitude at the frequency to which it is tuned [21–26]. However, due to its limitation in suppressing vibrations outside the tuned frequency range, this dissertation will explore a variation—the cubic nonlinear tuned vibration absorber—which offers a wider frequency band suppression range.

Given the background presented above, this dissertation presents novel work in the emphases of the use of nonlinear dynamical tools such as bifurcation diagrams and phase portraits to evaluate the efficacy of the cubic absorber in reducing vibrations transmitted to the hand from a chipping hammer.

The following sections detail the key elements of this dissertation: Section 1.2 highlighting the symptoms of HAVS, resulting from exposure to dangerous vibration levels; Section 1.3 reviews models for the hand-arm system; Section 1.4 overviews the models for the chipping hammer and discusses the model proposed for this study; Section 1.5 explores tuned vibration absorbers and the cubic absorber employed in this study. Section 1.6 gives a brief summary of the nonlinear dynamical tools used to assess the effectiveness of the cubic absorber, while Section 1.7 summarizes the research objectives and contributions. Finally, Section 1.8 outlines the remainder of the dissertation.

1.2 Hand–Arm Vibration Syndrome and Vibration Exposure

To motivate the need for studying methods to reduce vibrations, we begin by describing the detrimental effects of hand-arm vibration syndrome (HAVS) and highlight instances where the use of tools, such as chipping hammers, leads to excessive exposure to hand-arm vibrations (HAV), reinforcing the importance of our work.

HAVS often results from prolonged exposure to HAV, which refers to vibrations transmitted from hand-held power tools to the hands [27]. This disorder is characterized by vascular, musculoskeletal, and neurological issues [28–31]. One of the major symptoms of HAVS is vibration white finger (VWF), which can progress to disability in extreme cases [32–35]. Damage to the muscles and nerves of the hand can also lead to a loss of grip strength [36], and structural changes to the nerves around the wrist have been observed as a result of long-term vibration exposure [37]. Neurological symptoms such as tingling, paraesthesia, sensory loss, and decreased dexterity are also prevalent, affecting the quality of life and livelihood of those suffering from HAVS. Initially, these symptoms are intermittent, but if left unchecked, they can become persistent [38].

As noted by De Silva *et al* [39], HAVS remains a significant concern in various industries due to the inadequacies in regulating the duration and intensity of exposure, as recommended by international standards[30]. Two key metrics used to assess exposure are the 8-hour exposure value (A(8)) and the exposure limiting value (ELV). The A(8) value accounts for both the intensity and the duration of exposure, while the ELV defines the maximum daily limit beyond which workers should not be exposed.

In field measurements taken by De Silva *et al* for a chipping hammer, approximately 33% of operators exceeded the ELV, placing them at significant risk for developing HAVS. It was observed that reducing the time spent using the tool would not sufficiently lower the A(8) value, making it essential to introduce vibration control methods to mitigate vibrations reaching the hand. Similar findings were reported by López-Alonso *et al* [40], reinforcing that operators of chipping hammers are regularly exposed to vibrations exceeding the ELV. As such, reducing the magnitude of vibrations to lower the A(8) value becomes critical in preventing HAVS.

To address this issue, the next chapter will present background information on modeling the tool and hand-arm system to predict how vibrations are transferred to the hand-arm system.

Takeaway 1: Due to the detrimental effects of HAVS, it is vital that the appropriate vibration control methods are introduced to reduce an operators vibration exposure

1.3 Hand-arm Model

In assessing the vibration exposure risk posed to operators using a tool, it is crucial to consider the dynamics of the hand alongside those of the tool. Studies have shown that vibration characteristics—including magnitude and dominant frequencies—differ based on whether the hand-arm system is engaged with the tool [41]. This difference is attributed to the biodynamic response of the hand-arm, which influences the vibration characteristics of tools.

The biodynamic response of the hand-arm describes how vibrations are transmitted to the hand. Key biodynamic responses include apparent mass (AM), mechanical impedance (MI), apparent stiffness (AS), and vibration power. Each of these responses depends on dynamic factors such as force, acceleration, velocity, and displacement at the hand-tool interface. Physically, these biodynamic responses represent different characteristics of the system, with AM denoting the dynamic mass, MI representing system damping, and AS representing system stiffness [42].

To evaluate the effectiveness of a cubic absorber in reducing vibrations from a chipping hammer, it is essential to use a hand-arm model that captures the biodynamic response characteristics of the hand-arm. We considered several models proposed by Dong *et al.* [41], which are based on lumped mass parameters designed to represent the anatomical features of the hand. These models, both 2-DOF and 4-DOF, were characterized using the mechanical impedance and apparent mass of the hand-arm. While the 4-DOF model accurately predicted hand-arm responses across all frequencies, the 2-DOF model had limitations above 100 Hz. However, by focusing on parameters that matched the experimental apparent mass, the 2-DOF model could be tuned to simulate hand-arm responses at lower frequencies, making it more suitable for applications with resonance frequencies below 100 Hz.

For this study, we chose the 2-DOF model to evaluate hand-arm dynamics, as the chipping hammer operates at frequencies causing resonance below 100 Hz. This selection allows the 2-DOF model to effectively capture the response of the hand-arm at the tool's operating frequency.

Next, we discuss models considered when trying to analyze the dynamics of the chipping hammer

Take away 2: A 2-DOF model that captures the biodynamic response of the hand-arm can be used to evaluate vibration control methods for a chipping hammer.

1.4 Chipping Hammer Model

One of the most widely used models in the literature to describe the dynamics of percussive tools is a lumped parameter model. Lumped parameter models are often preferred due to their ability to capture the major dynamics of a system with relatively low computational cost. Examples of such models range from representations with simple visco-elastic connections to models incorporating cubic and nonsmooth nonlinearities, which describe the vibro-impact nature of percussive tool operation [10–18]. For example, Alabi *et al.* [13, 14] examined the qualitative dynamics of a hand-held impact tool, where the dominant form of nonlinearity was cubic, and demonstrated the effectiveness of a nonlinear absorber in reducing vibrations transmitted to the hand.

In applications such as drill-string drilling, Pavlovskaia *et al.* proposed vibro-impact models to predict optimal static and dynamic forces for achieving maximum drilling efficiency [11, 12]. Additionally, Aguiar *et al.* showed that a 7DOF vibro-impact system could reproduce experimental relationships between axial vibration peaks and mud flow rate in drilling systems [10]. In a similar vein, Franca and Weber developed a mathematical model considering only the percussive action of a resonance hammer, which successfully replicated both qualitative and quantitative experimental results [43]. Despite the widespread effectiveness of vibro-impact models in capturing the dynamics of percussive tools, existing studies have not addressed how to mitigate vibrations transmitted to the hand when modeling tool dynamics as a vibro-impact system.

We base part of our modeling philosophy on the work by Pavlovskaia *et al.* (2003), who successfully used an idealized vibro-impact oscillator to model ground moling dynamics and demonstrated how periodic and chaotic behaviors relate to experimentally observed performance metrics, such as penetration progression. Because that modeling approach (effectively a one-degree-of-freedom impact oscillator) can capture core nonlinear features and performance trends, we extend the concept by adopting a two-degree-of-freedom (2-DOF) model—leveraging an additional degree of freedom to represent the coupling between the tool and hand–arm system while preserving conceptual simplicity.

This study seeks to address how to mitigate vibrations transmitted to the hand when modeling tool dynamics as a vibro-impact system by studying a low-order vibro-impact model of a chipping hammer coupled to the hand, thereby demonstrating that lower-degree-of-freedom models can capture essential experimental trends while enabling the analysis of vibration transmission and control strategies.

Takeaway 3: A vibroimpact model which captures the dynamics of percussive tools can be used to understand the dynamics of a chipping hammer tool

1.5 Vibration Control Methods and the Tuned Vibration Absorber

One of the methods to reduce the level of transmitted vibration to the human hand is through anti-vibration gloves. However, designing an optimal anti-vibration glove that performs well across various users is challenging due to user-specific requirements, imposing a design limitation for broader, global applicability [44, 45]. Another common approach in mechanical systems to attenuate transmitted vibration is the use of a tuned vibration absorber (TVA). A TVA, typically consisting of a spring-mass-damper system tuned to the primary system's frequency, effectively suppresses vibrations by operating at the primary system's resonant frequency [46]. While the use of TVAs has shown effectiveness across various applications [21–26], a deviation from the tuned frequency of the TVA can result in amplified vibrations rather than suppression.

To address this limitation, a TVA can be modified by introducing a nonlinear stiffness element, producing a nonlinear tuned vibration absorber (NLTVA) that demonstrates a wider vibration suppression bandwidth than a standard TVA [47–50]. Using a nonlinear stiffness element increases the device's effective bandwidth, making it more applicable than a linear TVA [47–51]. Given that the operating frequency of the chipping hammer may vary during its operation, an NLTVA is proposed as a more effective solution to control vibrations from a vibro-impact chipping hammer model. Thus, a nonlinear absorber incorporating cubic nonlinearity is explored in this work, as this choice aligns with the hardening-type nonlinearity commonly observed in vibro-impact systems [52, 53].

The following section will describe the methods used to study the proposed nonlinear models.

Takeaway 4: A cubic absorber is employed in this study due to it's wider bandwith attenuation *ability as noted in literature.*

1.6 Nonlinear Dynamical Tools

In order to evaluate the efficacy of a cubic absorber, we have decided to study a nonlinear lumped parameter model with nonlinearities introduced via a cubic absorber and a nonlinear chipping hammer model, both coupled to a linear model of the hand. This setup aims to investigate 1) how the vibro-impact and cubic nonlinearity manifest in the behavior of the chipping hammer and 2) how the cubic nonlinearity of the absorber can be leveraged to reduce vibrations transmitted to the hand. To achieve these goals, we employ nonlinear dynamical tools such as bifurcation diagrams, phase portraits, and Poincaré maps.

Bifurcation diagrams are used to track changes in the qualitative structure of a dynamical system's flow while varying one or more system parameters [54]. For systems with vibro-impact nonlinearity, bifurcation diagrams are particularly useful for providing an overview of system dynamics. Martinelli *et al.* found that bifurcation diagrams were instrumental in understanding chaos and identifying stable period-doubling orbits in piecewise systems [55]. This insight is echoed in similar studies that highlight the effectiveness of bifurcation diagrams in capturing dynamic phenomena in piecewise systems [56, 57]. For vibro-impact systems, these diagrams are crucial for identifying abrupt changes in solutions, stability shifts, and the emergence of quasi-periodic and chaotic responses [58–60].

To gain a more detailed understanding of the bifurcations indicated in bifurcation diagrams, phase portraits are used. These portraits capture system trajectories by mapping the displacement and velocity of a system's degree of freedom in steady state [61]. In systems featuring both cubic and vibro-impact nonlinearities, phase portraits help visualize periodicity and chaotic regimes [62]. They can also highlight grazing events, a hallmark of vibro-impact systems [63].

To distinguish between quasi-periodic and chaotic motion shown in phase portraits and to visualize periodic and quasi-periodic behavior in a simpler way, Poincaré maps are utilized. These maps are generated by sampling a phase portrait at discrete times, typically at intervals corresponding to the system's excitation period [64–72]. On these maps, a period-n orbit is represented by n points on the attractor, while quasi-periodic motion forms a closed loop, and chaotic motion is depicted as a cloud of disorganized points [73, 74].

Analyzing our nonlinear system with these tools is essential for capturing the complex dynamics of the chipping hammer model. This understanding allows us to utilize the cubic absorber's nonlinearity to minimize vibrations transmitted to the hand. Thus, the combination of bifurcation diagrams, phase portraits, and Poincaré maps provides a comprehensive analysis of the system's behavior.

Takeaway 5: Due to the complementary insights provided by bifurcation diagrams, phase portraits, and Poincaré maps, we will use all three methods to analyze the system's dynamics.

1.7 Research Objectives and Contributions

This dissertation will be to the best of our knowledge, the first to study the nature of vibration transmission to the hand-arm system from various nonlinear models of a chipping hammer. Another key novelty of this work is the exploration of a cubic nonlinear absorber as a vibration control method to mitigate vibrations transmitted to the hand. Finally, we will validate one of the nonlinear models using experimental data. This experimentally verified model will additionally be used to evaluate the effectiveness of the cubic absorber in controlling vibrations.

The specific research objectives of this dissertation are:

- Enhance the understanding of vibration transmission to the hand from a cubic nonlinear model of a chipping hammer through numerical and analytical approaches.
- Deepen the understanding of vibration transmission to the hand from a vibro-impact model of a chipping hammer using numerical analysis.
- Investigate the efficacy of a cubic absorber compared to a linear absorber in reducing vibration magnitude to the hand when coupled with both cubic and vibro-impact chipping hammer models.
- Validate the proposed nonlinear vibro-impact models by comparing its predictions with experimental data and evaluate the potential effectiveness of the cubic absorber in experimental settings.

The objectives of this dissertation lay the groundwork for several significant contributions to the literature. Specifically, these contributions include to the best of our knowledge a first-of-its-kind investigation of a unique nonlinear lumped parameter model of a chipping hammer to analyze the nature of vibrations transmitted to the hand. Also, this dissertation investigates, for the first time, the efficacy of a cubic absorber in reducing vibrations to the hand from the chipping hammer model. Finally, the dissertation explores the ability of the vibro-impact nonlinear model to replicate experimental findings. The experimental validation of the nonlinear model is a novel contribution that has not been explored in the context of hand-tool interaction. Specifically, the novelty of the contributions of the dissertation to the best of our knowledge is as highlighted below:

- Introducing the first study on vibrations transmitted to the hand when a nonlinear chipping hammer model is coupled with a hand model. Prior studies have focused on linear models, neglecting the inherent nonlinearity in percussive tools. This dissertation leverages the advantages of nonlinear models to more accurately represent the dynamics of chipping hammers.

- Investigating, for the first time, the potential of cubic nonlinear absorbers to attenuate vibrations transmitted to the hand. The superiority of nonlinear absorbers such as the cubic absorber has been demonstrated in the literature for other applications; however, the efficacy of this vibration control method in tool-hand interaction has not been explored. This study contrasts the performance of cubic absorbers against traditional linear absorbers for vibration control in chipping hammers, demonstrating the utility of the cubic absorber in curbing vibrations to the hand.
- Emphasizing the experimental validation of the vibroimpact nonlinear model of the combined chipping hammer-hand-arm system. In existing research, more emphasis has been placed on identifying lumped mass parameters of a linear tool-hand model. However, studies have revealed that percussive tools such as the chipping hammer are better described using nonlinear models due to the nonlinear restoring force between the tool tip and ground. Thus, this work aims to determine whether a nonlinear model offers a better predictive capability for vibration transmission compared to conventional linear models.

1.8 Dissertation Layout

Following the introduction chapter — which presents the background, problem statement, objectives, and contributions of the dissertation — Chapter 2 examines a hand-held impact machine modeled as an oscillator with cubic nonlinearities. The performance of both linear and nonlinear tuned vibration absorbers in suppressing vibrations transmitted from the tool to the hand is investigated. Chapter 3 builds on this work by employing nonlinear dynamical tools such as Poincaré maps, phase portraits, and bifurcation diagrams to further analyze the absorber's effectiveness in vibration suppression. In Chapter 4, the chipping hammer is modeled as a vibro-impact system, and the absorber's performance is again evaluated using nonlinear dynamical tools. Chapter 5 develops a vibro-impact model of the chipping hammer that is closely aligned with experimental findings and focuses on grazing phenomena, a hallmark characteristic of systems with vibro-impact nonlinearities. Finally, Chapter 6 presents a summary of key findings along with suggestions for future progression of this work.

Chapter 2

Effectiveness of a Cubic Nonlinear Absorber on Curbing Vibrations to the Cubic Model of an Impact Tool via Linear Analysis

This chapter was collaboratively developed by the following authors: **Ore Alabi**, **Dr. Sunit Kumar Gupta**, and **Dr. Oumar Barry**. The contributions, categorized according to the *CRediT (Contributor Roles Taxonomy)*, are as follows:

- **Conceptualization**: Ore Alabi, with guidance from Dr. Oumar Barry.
- **Methodology**: Ore Alabi, with feedback from Dr. Oumar Barry and Dr. Sunit Kumar Gupta.
- **Formal Analysis**: Ore Alabi.
- **Investigation**: Ore Alabi.
- **Writing – Original Draft**: Ore Alabi.
- **Writing – Review & Editing**: Dr. Oumar Barry and Dr. Sunit Kumar Gupta.

- **Supervision**: Dr. Oumar Barry.

This chapter is edited from: Alabi, O., & Barry, O. (2020, October). On the nonlinear vibration analysis of a hand-held impact machine. In Dynamic Systems and Control Conference (Vol. 84287, p. V002T29A004). American Society of Mechanical Engineers.

2.1 Introduction

Hand-held impact tools are ubiquitous in industrial sectors such as mining, airplane manufacturing and construction [1–4]. A major problem with HIM's is that workers who use these tools may be exposed to hand transmitted vibrations (HTV). Severe exposure to hand-arm vibrations puts these workers at risk of developing hand-arm vibration syndrome(HAVS). It has been shown that approximately 20% of workers who are exposed to HTV through tools such as impact screwdrivers and chipping hammers are at risk of developing finger blanching, [5] a symptom of HAVS.

Hand-arm vibration syndrome (HAVS) is a disorder characterized by vascular, musculoskeletal and neurological disorders [28–31]. One of the major symptoms of HAVS is vibration white finger (VWF) which in extreme cases can lead to disability [32–35]. As a result, two main methods have been proposed to attenuate hand transmitted vibrations from HIM's. These methods are vibration isolation and dynamic absorption [75]. The incorporation of vibrational isolators to mitigate vibrations at the tool handle has been investigated in [76, 77]. In these studies, the isolator was devised as a material placed between the tool handle and hands of an operator. The problem with such isolators is that large masses are required at the handle for the isolator to be effective [78]. Also, there is a trade-off between the controllability of the tool and vibration isolation effectiveness when making use of such isolators

[79]. Isolators in the form of anti-vibration gloves have also been explored as a means of attenuating vibrations from a tool's handle. However, studies have shown that these gloves are effective in high-frequency ranges ($> 150Hz$) and ineffective in low-frequency ranges [80, 81].

The second method for mitigating unwanted vibrations from HIMs is the use of vibration absorbers. Linear absorbers have been used in [79]. However, a common problem with using linear tuned vibrational absorbers is that slight variations from the frequency from which these absorbers have been tuned can lead to amplification rather than suppression of vibrations. As a result, nonlinear tuned vibration absorbers (NVA) have been studied to increase the operating frequency range of vibrational absorbers. Wang et al. [49] used a NVA to reduce machine chatter suppression and obtained a 30 percent improvement in machine performance when compared to a TVA. With regards to the implementation of a NVA in a HIM, Lindell et al. [50] showed that an NVA in a pneumatic impact machine could suppress vibrations in a broader range of frequency than the TVA.

To further improve vibration attenuation mechanisms, more emphasis should be put on nonlinear vibration attenuation mechanisms due to the improvement they offer over linear vibration attenuation mechanisms. The (nonlinear)vibro-impact dynamics of a HIM makes it vital that vibration attenuation from HIMs be done with nonlinear mechanisms [82]. Habib et al. have shown that vibration attenuation mechanisms are more effective when they have the same functional form of the system on which they are acting on [53]. The addition of inerters to nonlinear absorbers is also a topic that should be explored as inerters improve the performance of vibration absorbers by increasing the effective mass of the absorbers while having small physical masses. This is true because a larger absorber mass improves the vibration suppression characteristics of an absorber. The effective mass boosting effects realized with a small physical mass, characteristic of an inerter, has been realized through a

2kg inerter that produces an effective mass of 300kg [83]. Various case studies have shown the effectiveness of inerters coupled with linear absorbers to reduce vibrations in cars and civil engineering structures [84–88].

As a result of these findings, the present paper presents, for the first time, the study of a HIM with a nonlinear vibrational absorber and an inerter (NVAI). The addition of an inerter to the dynamic absorber is expected to improve the vibration mitigation properties of the absorber. While the addition of a nonlinear absorber will result in a wider bandwidth vibration suppression in these HIMs. To realize this goal, this paper will study a nonlinear oscillator equipped with a NVAI. The oscillator is assumed to be the mass of the vibrating HIM. The main mass of the HIM is coupled to the HAS so the level of vibration attenuation to the HIM is assessed by considering the level of vibration mitigation at the HAS. We then use the harmonic balance and continuation method to obtain plots that will highlight the effectiveness of the different absorbers.

2.2 Mathematical Modelling

In this paper, the vibration response of the HAS connected to a HIM is analyzed while the HIM is equipped with a nonlinear tuned vibration absorber–inerter (NVAI). The model of the HAS used in this study is adapted from the paper by Dong et al. [41], in which the HAS is coupled at a single point to the HIM. This model was used in this study because it can provide a reasonable response of the HAS for frequencies less than 100 Hz. The HIM evaluated in this paper operates in a frequency range of 30–60 Hz; hence the HAS model used is appropriate for our study.

The schematic of the HAS and HIM coupled with a NVAI is shown in Fig. 5.1. m_H, m_s, m_a, and m_n represent the mass of the HIM, tissue and skin covering the HAS, hand–arm, and absorber respectively. k_H, k_{HL}, and c_H represent the nonlinear and linear ground connection stiffness, and the damping coefficient of the HIM respectively. b represents the effective mass provided by an inerter which is grounded on one side and coupled to the mass of the absorber on the other side. In this study, the effective mass provided by the inerter is taken to be two times its mass.

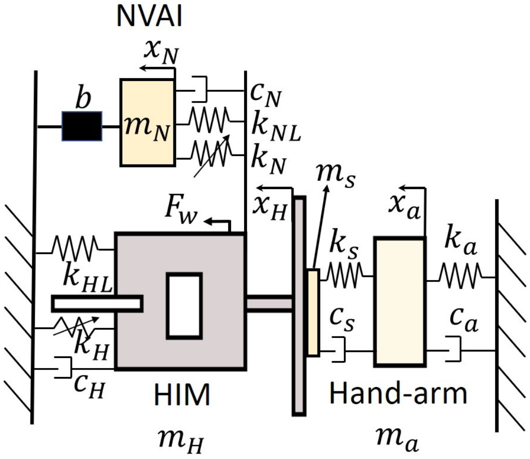

Figure 2.1: Schematic of the HIM and HAS system with a NVAI

For this analytical model, F_w represents the excitation force of the HIM due to the reciprocating motion of the piston which causes it to function. The analytical form of this excitation was adapted from the expression obtained experimentally in [78] and is shown below:

$$F_w = F_{ref} \left(\frac{\omega}{\omega_{ref}} \right)^2 \sin(\omega t) \tag{2.1}$$

In this expression, ω represents the excitation frequency of the excitation force while ω_{ref} represents a reference frequency needed to describe the analytical form of the excitation force.

The HIM system with a NVAI has three degrees of freedom represented as the motion of the HIM x_H, HAS x_a, and the absorber x_N. The governing equations of motion are obtained using Newton's second law to give:

$$\begin{aligned}(m_H+m_s)\ddot{x}_H-c_s\dot{x}_a-k_sx_a+(c_H+c_N+c_s)\dot{x}_H-c_N\dot{x}_N\\+(k_{\mathrm{HL}}+k_{\mathrm{NL}}+k_s)x_H+k_N(x_H-x_N)^3+k_Hx_H^3-k_{\mathrm{NL}}x_N=\frac{\omega^2F_{\mathrm{ref}}\sin(\omega t)}{\omega_{\mathrm{ref}}^2},\end{aligned} \tag{2.2a}$$

$$m_a\ddot{x}_a+(c_a+c_s)\dot{x}_a+(k_a+k_s)x_a-c_s\dot{x}_H-k_sx_H=0, \tag{2.2b}$$

$$\begin{aligned}(m_N+b)\ddot{x}_N-c_N\dot{x}_H+c_N\dot{x}_N+k_N(x_N-x_H)^3\\-k_{\mathrm{NL}}x_H+k_{\mathrm{NL}}x_N=0.\end{aligned} \tag{2.2c}$$

These equations are then written in a compact form to obtain

$$[\mathbf{M}]\,\ddot{\mathbf{x}}+[\mathbf{C}]\,\dot{\mathbf{x}}+[\mathbf{K}]\,\mathbf{x}+\mathbf{N}=\mathbf{F_{eq}} \tag{2.3}$$

where $\mathbf{x}=[x_H,\,x_a,\,x_N]^\top$. $\mathbf{M}$, $\mathbf{C}$, and $\mathbf{K}$ are 3×3 inertia, damping, and stiffness matrices respectively; $\mathbf{N}$ is a 3×1 vector containing the nonlinear terms; and $\mathbf{F_{eq}}$ is a 3×1 force vector. These matrices are presented in Appendix A.

2.3 Analytical Solution

The method of harmonic balance is used to formulate a set of equations from which we can obtain explicit expressions for the displacement amplitude of the systems. This is done so that the nonlinear amplitude-frequency response of the HIM can be plotted using the arc-length continuation method as numerical simulations cannot capture all of the points on a nonlinear amplitude-frequency response plot. Via the method of harmonic balance, the solution of the system with a NVAI is synonymous with the external excitation acting on the system. Therefore the solutions of Eqs. (2.2) are assumed to be of the form:

$$\{\mathbf{x}\}(t) = \{\mathbf{A}\}\cos(\omega t) + \{\mathbf{B}\}\sin(\omega t) \tag{2.4}$$

where $\{\mathbf{A}\}$ and $\{\mathbf{B}\}$ are (3×1) columns vectors with unknown coefficients a_1, c_1, e_1 and b_1, d_1, f_1 respectively. After substituting the expression above for $x_H(t)$, $x_N(t)$ and $x_a(t)$ into Eqs. (2.2), we obtain,

$$\begin{aligned}
&-\omega^2[\mathbf{M}]\{\mathbf{A}\}\cos(\omega t) - \omega^2[\mathbf{M}]\{\mathbf{B}\}\sin(\omega t)\\
&-\omega[\mathbf{C}]\{\mathbf{A}\}\sin(\omega t) + \omega[\mathbf{C}]\{\mathbf{B}\}\cos(\omega t) + [\mathbf{K}]\{\mathbf{A}\}\cos(\omega t)\\
&+[\mathbf{K}]\{\mathbf{B}\}\sin(\omega t) + [\mathbf{N_1}] = \{\mathbf{F_{eq}}\},
\end{aligned} \tag{2.5}$$

where $[\mathbf{N_1}]$ is a (3×1) column vector defined in Appendix A. From Eqs. (2.2), we obtain 6 sets of equations by equating the coefficients of sine and cosine from these expressions to zero. The variables a_1, b_1, c_1, d_1, e_1 *and* f_1 can then be calculated from these equations.

2.4 Results and Discussion

In this section, the analytical solution for the HIM and HAS system with a NVAI is obtained and verified via a numerical method, and the performance of the NVAI is evaluated and compared to the performance of the classical TVA and NVA. Parametric studies are also carried out to understand the effects of viscous damping and inertance of the NVAI, and HIM nonlinear stiffness on the performance of the NVAI.

The numerical properties of the NVAI used for validating the NVAI's analytical solution are presented in Table 5.1. The value for the mass of the HIM is chosen to represent the mass of a typical pneumatic chipping hammer, while the other properties of the HIM are chosen arbitrarily. The other systems being studied also use the same parameters listed in Table 5.1 except the parameter m_N which is set to $0.05m_H$ for the NVA and TVA. It should be noted that for a model of the HIM-HAS system with a NVA, b will be set to zero while for a TVA both b and k_N will be set to zero. The linear parameters of the absorbers are determined using the second order approximations obtained when the properties of a dynamic absorber, with linear stiffness and damping, attached to a linear oscillator are optimized by the H_∞ optimization method as done in [89]. The nonlinear stiffness of the NVA and NVAI are determined using the proposed principal of similarity by [90], wherein the mathematical form of the NVA's restoring force is a mirror image of the restoring force of the primary system.

As mentioned above, the first part of our analysis involves the validation of our system's analytical solutions by comparing the solutions of our system obtained via the harmonic balance method with the solution of our system obtained using the numerical ode solver, ode45, in Matlab. At $\omega = 10,\ 360,\ 510,\ and\ 700$, we obtain a mean percentage difference between our analytical and numerical solution of $0.26\%,\ 0.71\%,\ 1\%,\ and\ 0.27\%$ respectively. We consider these errors to be negligible and determine that there is a good agreement between the solutions obtained using the numerical method and the harmonic balance method. Therefore, further analysis of the response of all systems presented in this study will be done using the harmonic balance method and arc-length continuation method.

In the remaining part of this section we compare the effectiveness of the absorbers in attenuating vibrations at different forcing amplitudes. The amplitude-frequency plots of the HIM with and without the three different absorbers at an excitation forcing amplitude of $300\,N$ and $500\,N$ are shown in Fig. 2.3.

Table 2.1: Parameters of the HIM system equipped with a NVAI.

Parameter	Value	Units	Parameter	Value	Units	Parameter	Value	Units
m_H	1.7	kg	k_{HL}	$3(10^5)$	N/m	c_H	50	Ns/m
m_a	1.5546	kg	k_a	4279	N/m	c_a	76.1	Ns/m
m_s	0.0493	kg	k_s	62804	N/m	c_s	192.9	Ns/m
m_N	$0.02m_H$	kg	k_{NL}	13280	N/m	c_N	9.3	Ns/m
F_{ref}	300	N	ω_{ref}	26.1	Hz	b	$0.04m_H$	kg
k_H	$3(10^8)$	Ns/m^3	k_N	$2.5(10^6)$	Ns/m^3	–	–	–

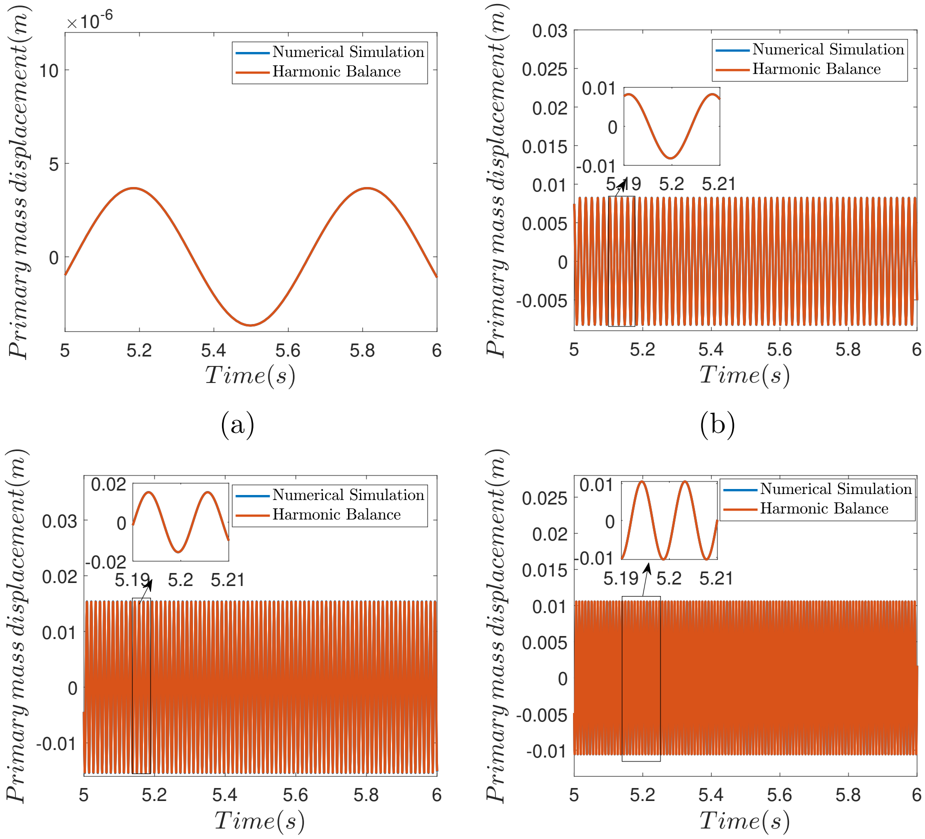

(a) (b)

(c) (d)

Figure 2.2: Comparison of numerical and analytical solutions for the responses of the HIM (primary mass) at (a) 10 rad/s, (b) 360 rad/s, (c) 510 rad/s and (d) 700 rad/s.

For F_{ref} of our excitation forcing amplitude set to 300 N, all the absorbers are able to effectively mitigate vibrations produced by the HIM. This is highlighted by the difference in displacement of the HAS with and without an absorber for different frequencies in Fig. 2.3a.

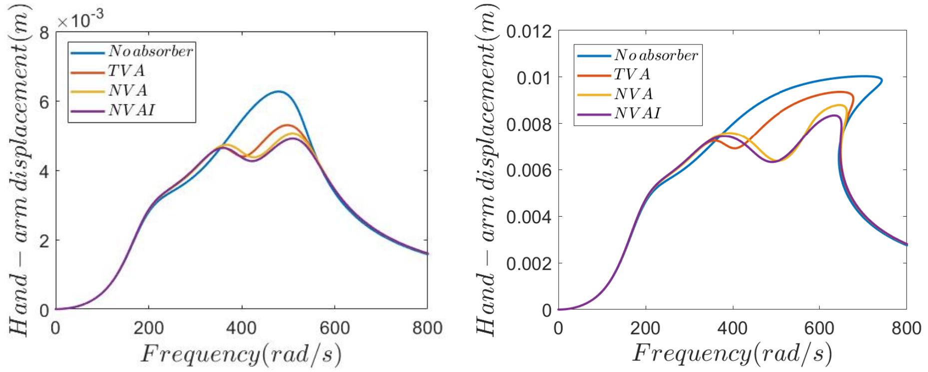

(a) (b)

Figure 2.3: Frequency response of HAS for excitation forcing amplitude of (a) $300N$ and (b)$500N$

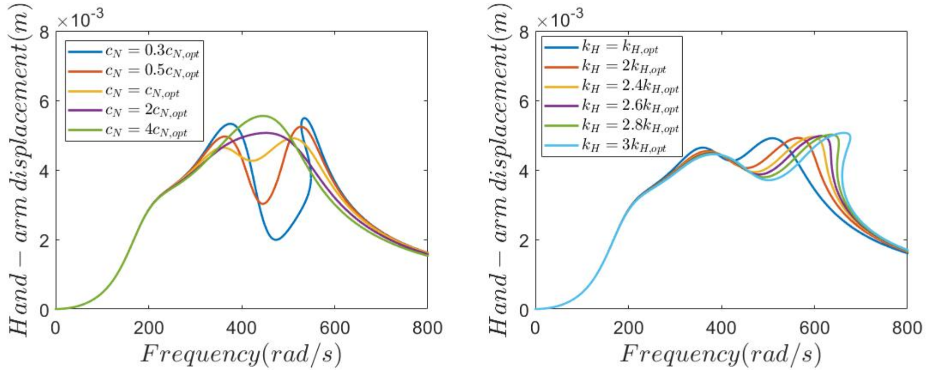

(a) (b)

Figure 2.4: Frequency response of HAS for a) varying absorber damping parameters and b) varying HIM non-linear stiffness parameters.

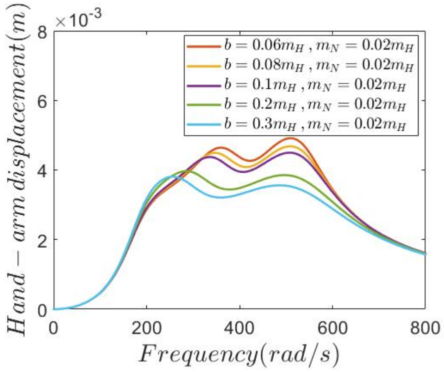

Figure 2.5: Frequency response of HAS for varying inerter values.

Fig. 2.3a also shows that the NVA and NVAI are more effective at attenuating vibrations than the TVA. When the excitation force is increased by setting F_{ref} to 500N, the nonlinear characteristic of the HIM appears as the hardening trait of the cubic spring becomes more apparent (Fig. 2.3b). It can also be seen that the TVA becomes detuned. With detuning observed when one of the TVA's frequency peaks begins to obtain a shape similar to the peak of the displacement of the HAS without an absorber. Similar observations have been seen in [53]. This happens because the TVA does not contain a spring which has the same nonlinear form as the nonlinear spring of the vibrating HIM.

Based on these observations, we can narrow down our options of the most effective absorbers to the NVA and NVAI which do not get detuned for strongly nonlinear motions of the HIM, which become apparent with an increase in forcing amplitude. The advantage which the NVAI holds over the NVA is a potential reduction in weight of the vibration attenuation mechanism. A well known theory in the design of absorbers is that an increase in the mass of an absorber makes for a more effective absorber. As mentioned before, the NVAI employed in this study has a total mass of $0.068kg$ where its inerter's effective mass is two times the inerters original mass. This assumption seems fair given that an inerter can provide an inertance about 3 times its mass [91]. Given this fact, we can conclude that the NVAI is a better option for attenuating vibrations as it possesses a mass less than the mass of the NVA($0.085kg$) while also suppressing vibrations better as seen in Fig 2.3b.

Next, we analyze the changes in the response of the HAS while the damping of our ideal absorber, the NVAI, is varied. Our results, shown in Fig. 2.4a, indicate that as the damping of the absorber is increased, the maximum peak of the response of the HAS initially decreases then increases. We also observe that the absorber has smaller magnitudes of minimal displacement of the HAS for smaller values of damping. This can be seen in the region between 400 rad/s and 500 rad/s of Fig. 2.4a. This pattern observed is similar to changes in the frequency response of a damped linear oscillator for varying damping parameters of an attached absorber. For the smallest value of c_N employed, the frequency response breaks away from what looks like a fixed point at 508 rad/s.

Further, the effect of changing the non-linear ground connection stiffness k_H on the frequency response of the HAS is studied. Fig. 2.4b, shows that an increase in k_H leads the system to operate in its nonlinear regime as shown through the appearance of the hardening resonance curve for the largest value of k_H. It is worth noting that the peaks of the frequency response curves vary slightly as the HIM moves from operating in a linear to nonlinear region.

The effect of changing the inertance of the NVAI is also studied. An increase in the inertance of the NVAI which corresponds to an increase in the mass of the absorber albeit without a substantial increase in the weight of the absorber leads to an increase in the effectiveness of the absorber. Fig. 2.5 shows that an increase in the inertance of the NVAI, reduces the resonance peaks of the frequency response curves and makes the absorber more effective.

2.5 Conclusion

Based on the results obtained from the study of the HIM-HAS system with different absorbers, we made the following observations. The NVAI and NVA were better at suppressing vibrations of our system than the TVA. This was because for higher forcing amplitudes, when the frequency response curve of the HAS begins to show a hardening resonance, the TVA becomes detuned while the NVA and NVAI are still able to effectively supress vibrations. This indicates that the NVAI and NVA are effective options for maintaing a wide suppression band for a system with nonlinearities.

We also observed that the NVAI performed better than the NVA because the NVAI suppresses vibrations better than the NVA while having a smaller mass. The NVAI was able to achieve this feat as it could provide a large effective mass by virtue of its inerter which can simulate an effective mass more than twice its mass. Given that the effectiveness of absorbers is limited by the mass which they can possess, it is vital that an absorber such as the NVAI, which provides an effective mass larger than its mass, is adopted. We showed that increasing the mass of an absorber, by increasing the inertance of the NVAI, does indeed increase the vibration suppression characteristics of the absorber(NVAI). This result supports the claim that an increase in the effective mass of an absorber is an ideal way to improve its performance.

Finally we varied the nonlinear stiffness of the HIM and the damping of the absorber. We discovered that increasing the nonlinear stiffness of the HIM made the systems frequency response curve more likely to exhibit a nonlinear hardening resonance. We also discovered that as the damping of the absorber was increased, the maximum peak of the response of the HAS initially decreased then increased. We also observed that the absorber had smaller magnitudes of minimal displacement of the HAS for smaller values of damping, as seen in the region between 400 rad/s and 500 rad/s.

To design a better NVAI for the HIM, it is recommended that the nonlinearity apparent in a HIM during its operation be studied. This is so that the absorber can be modelled to possess the nonlinear features apparent in the system and hence be effective. The absorber in our work was effective at mitigating vibrations because it possessed the same assumed cubic nonlinearities as the HIM system.

Chapter 3

Effectiveness of a Cubic Nonlinear Absorber on Curbing Vibrations to the Cubic Model of an Impact Tool via Nonlinear Analysis

This chapter was collaboratively developed by the following authors: **Ore Alabi**, **Dr. Sunit Kumar Gupta**, and **Dr. Oumar Barry**. The contributions, categorized according to the *CRediT (Contributor Roles Taxonomy)*, are as follows:

- **Conceptualization**: Ore Alabi, with guidance from Dr. Oumar Barry.
- **Methodology**: Ore Alabi and Dr. Sunit Kumar Gupta, with feedback from Dr. Oumar Barry.
- **Formal Analysis**: Ore Alabi.
- **Investigation**: Ore Alabi.
- **Writing – Original Draft**: Ore Alabi.
- **Writing – Review & Editing**: Dr. Oumar Barry and Dr. Sunit Kumar Gupta.

- **Supervision**: Dr. Oumar Barry.

This chapter is edited from: Alabi, O., Gupta, S. K., Barry, O. (2022, August). Dynamics of a Nonlinear Absorber and Hand-Held Impact Machine. In International Design Engineering Technical Conferences and Computers and Information in Engineering Conference (Vol. 86304, p. V009T09A022). American Society of Mechanical Engineers.

and

Alabi, O., Gupta, S. K., Barry, O. R. (2023). Vibration analysis of a nonlinear absorber coupled to a hand-held impact machine. Journal of Computational and Nonlinear Dynamics, 18(8), 081006.

3.1 Introduction

The use of a hand-held impact machine (HHIM) is widespread in the construction industry. These HHIMs use a vibrating tool that impacts the surface in a continuous manner and simultaneously transmits reactive vibrating forces to the operators' hand. Excessive exposure of the operators' hands to severe levels of vibrations can lead to hand-arm vibration syndrome (HAVS) [27]. HAVS is a series of disorders which can be characterized as vascular, neurological and musculoskeletal [28–32]. The debilitating effects of HAVS may include numbness and pain at hand, decreased tactile perception at the fingers, and in extreme cases, the development of gangrene and eventually amputation [80]. Therefore, to attenuate these transmitted vibrations and prevent the development of HAVS, it is essential to develop methods to reduce vibrations transmitted to the hand-arm system.

One of the methods to reduce the level of transmitted vibration to the human hand is anti-vibration gloves. However, designing an optimum anti-vibration glove for better performance is user-specific and hence, imposes a design limitation for global use [44, 45]. Another common practice in the mechanical system to attenuate the transmitted vibration is using a tuned vibration absorber (TVA). A TVA consists of a spring-mass-damper system tuned to the primary system. Hence, it effectively suppresses the vibrations by operating at a resonant frequency of the primary system [46]. Although the use of TVA has been shown to be effective for various applications [21–26], a slight deviation from the tuned frequency of the TVA can lead to the amplification of vibrations. To address this issue, a TVA can be modified by including a nonlinear stiffness element in the system. This variation of a TVA has often been termed a nonlinear tuned vibration absorber (NLTVA) and has been shown to have a wider vibration suppression bandwidth than the TVA [47–50].

Furthermore, it has been observed that an increase in the mass of an absorber increases its vibration suppression bandwidth [92–94]. However, an excessive increase in the absorber mass is often undesirable due to the design constraints in the primary system. Therefore, devices known as Inerters can be added to the absorber system to circumvent this issue as they can provide an effective mass more than double its original mass. This further implies that with the addition of an Inerter, the effective mass of an absorber system can be increased without any significant increase in the absorber mass. The effectiveness of an Inerter can be illustrated through the use of 2kg inerter to provide an effective mass of 300kg [83]. In the current work, an absorber system with an inerter will be termed as nonlinear vibration absorber inerter (NVAI).

The preliminary analysis of the hand-arm system with a HHIM along with NVAI showed the effectiveness of NVAI in comparison to the linear TVA [94]. However, a detailed nonlinear analysis of the system, which can further guide the optimum design of NVAI, has not been performed. Therefore, this work, for the first time, presents a detailed nonlinear analysis of the system. To achieve this, we model the combined HAS-HHIM-NVAI as a lumped parameter model. The HAS will be modeled as a 2DOF proposed by Dong *et al.* [41]. Due to nonlinearities exhibited in an impact tools operation, via friction between contact surfaces or loss of contact between tool and material, the nonlinearities in the HHIM are modeled as cubic. Given the nonlinearities introduced to the system, nonlinear analysis techniques will be employed to study the system.

The rest of the paper is organized as follows. In section 5.1, the Mathematical model of the HAS-HHIM-NVAI system is presented. In section 5.2 a bifurcation analysis of the system is presented. Also, Poincare maps and phase portraits are used to analyze the dynamics of the system. Finally, some conclusions are drawn on the study in section 5.3.

3.2 The Mathematical Model of a HIM–HAS–NVAI System

In this section, we formulate a lumped parameter model to analyze the dynamics of a Hand-arm System (HAS) coupled with an HIM and a NVAI. The schematic of the combined system is shown in Fig. 5.1. In the current analysis, we employ the HAS proposed by Dong *et al.* [41]. Also nonlinearity is introduced in the lumped parameter model of the system by including nonlinearity in the HIM and NVAI, as shown in Fig. 5.1. For the sake of simplicity in the analysis, we consider the nonlinearity in the HIM as cubic. Due to nonlinearities exhibited in an impact tools operation, via friction between contact surfaces or loss of contact between tool and material, the nonlinearities in the HIM are modeled as cubic. Therefore, the nonlinearity of the NVAI should also be cubic for better vibration suppression [53]. In Fig. 5.1, m_H, m_s, m_a, and m_n represent the masses of the HIM, human-hand skin in contact with the handle of HIM, hand-arm system, and the absorber, respectively. k_H and k_{HL}

represent the nonlinear and linear ground connection stiffness, respectively, whereas, k_N and k_{NL} represent the nonlinear and linear stiffness of the NVAI respectively. c_H and c_N represent the linear viscous damping coefficient of the HIM and NVAI, respectively. Further, k_s and c_s are the linear spring and viscous elements connecting the masses m_a and m_s, respectively, while k_a and c_a are the linear spring and viscous elements connecting the mass m_a to the body/trunk (modelled as a fixed surface), respectively. The inertance, which is grounded on one side and coupled to the mass of the absorber on the other side, is represented by b.

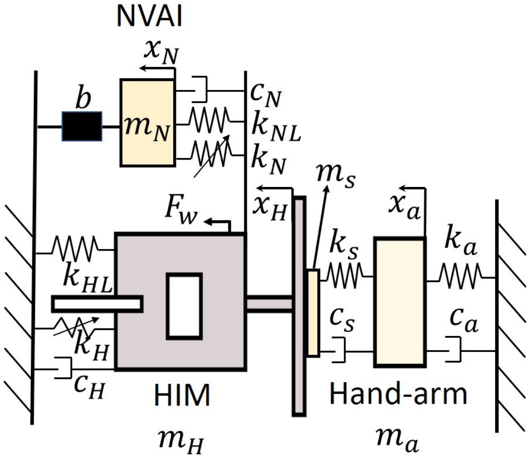

Figure 3.1: Schematic of the combined system of HIM-HAS system with a NVAI

If x_H, x_a, and x_N represent the motion of HIM, HAS, and NVAI, respectively, then the governing equations of motion are given by

$$[\mathbf{M}]\{\ddot{\mathbf{x}}\} + [\mathbf{C}]\{\dot{\mathbf{x}}\} + [\mathbf{K}]\{\mathbf{x}\} + \{\mathbf{f_{nl}}\} = \{\mathbf{F_{eq}}\} \tag{3.1}$$

where $[\mathbf{M}]$, $[\mathbf{C}]$, and $[\mathbf{K}]$ are (4×4) inertia, damping and stiffness matrices, respectively, $\{\mathbf{f_{nl}}\}$ represents the nonlinear force terms for the system, $\{\mathbf{F_{eq}}\}$ is a (3×1) force vector and $\{\mathbf{x}\} = [x_H,\, x_a,\, x_N]'$ is a (3×1) displacement coordinate vector. These matrices are defined in Appendix A.

In the above governing equations of motion, F_w represents the excitation force acting on the

HIM due to the reciprocating motion of the piston inside the HIM. The analytical form of F_w is adapted from the experiments reported in [78] and is given by

$$F_w = F_{ref} \left(\frac{\omega}{\omega_{ref}} \right)^2 \sin\left(\omega t\right). \tag{3.2}$$

To reduce the effective number of parameters, we nondimensionalize the governing equations of motion, and accordingly, introduce the following scales and nondimensional parameters

$m_1 = m_H + m_s$, $m_2 = m_N + b$, $m_3 = m_a$, $\omega_1 = \frac{k_{HL}}{m_1}$, $\tau = t\omega_1$, $x_0 = \frac{g}{w_1^2}$, $y = \frac{x}{x_0}$, $\Omega = \frac{\omega}{\omega_1}$, $\zeta_1 = \frac{c_H}{2\sqrt{m_1 k_{HL}}}$, $\zeta_2 = \frac{c_s}{2\sqrt{m_1 k_{HL}}}$, $\zeta_3 = \frac{c_N}{2\sqrt{m_1 k_{HL}}}$, $k_{r1} = \frac{k_s}{k_{HL}}$, $k_{r2} = \frac{k_{NL}}{k_{HL}}$, $k_{rnl1} = \frac{k_H\, x_0^2}{k_{HL}}$, $k_{rnl2} = \frac{k_N\, x_0^2}{k_{HL}}$, $F = \frac{F_{ref}}{m_1\, x_0\, \omega_{ref}^2}$, $\alpha = \frac{m_1}{m_2}$, $k_{r3} = \frac{k_a}{k_{HL}}$, $\alpha_2 = \frac{m_1}{m_3}$, $\zeta_4 = \frac{c_a}{2\sqrt{m_1 k_{HL}}}$.

Using above mentioned scales and nondimensional parameters, Eq. (3.1) can be nondimensionalized as

$$\left[\mathbf{M1}\right]\left\{\mathbf{y''}\right\} + \left[\mathbf{C1}\right]\left\{\mathbf{y'}\right\} + \left[\mathbf{K1}\right]\left\{\mathbf{y}\right\} + \left\{\mathbf{f1_{nl}}\right\} = \left\{\mathbf{F1_{eq}}\right\} \tag{3.3}$$

where $[\mathbf{M1}]$, $[\mathbf{C1}]$, and $[\mathbf{K1}]$ are (4×4) matrices with nondimensional parameters, $\{\mathbf{f1_{nl}}\}$ represents the nonlinear force terms for the system, $\{\mathbf{F1_{eq}}\}$ is a (3×1) force vector and $\{\mathbf{y}\} = [y_H,\, y_N,\, y_a]'$ is a (3×1) displacement coordinate vector. These matrices are defined in Appendix A.

Prime ($'$) denotes the derivative with respect to the nondimensional time τ. For the analytical treatment of the coupled system, we rewrite Eqs. (3.3) in a compact state-space form as

$$y_1' = y_2\,, \tag{3.4a}$$

$$\begin{aligned} y_2' =& 2\zeta_1 y_2 - y_1 - 2\zeta_2 \left(y_2 - y_4\right) - k_{r1}\left(y_1 - y_3\right) - k_{r2}\left(y_1 - y_5\right) - 2\zeta_3\left(y_2 - y_6\right) - k_{rnl1} y_1^3 \\ & - k_{rnl2}\left(y_1 - y_5\right)^3 + F\Omega^2 \sin\left(\Omega\tau\right), \end{aligned} \tag{3.4b}$$

$$y_3' = y_4\,, \tag{3.4c}$$

$$y_4' = -\,2\zeta_3\alpha\left(y_6 - y_2\right) - k_{r2}\alpha\left(y_5 - y_1\right) - k_{rnl2}\alpha\left(y_5 - y_1\right)^3 \tag{3.4d}$$

$$y_5' = y_6\,, \tag{3.4e}$$

$$y_6' = -k_{r3}\alpha_2 y_3 - 2\zeta_4\alpha_2 y_4 - k_{r1}\alpha_2\left(y_3 - y_1\right) - 2\zeta_2\alpha_2\left(y_4 - y_2\right)\,, \tag{3.4f}$$

where $[y_1, y_2, y_3, y_4, y_5, y_6] = [y_H, y_H', y_N, y_N', y_a, y_a']$. Having established the nondimensional governing equations of motion, next we present the analytical solution procedure along with the linear stability analysis in the subsequent section.

3.3 Analytical Solution and Stability Analysis

The linear stability analysis of a nonlinear system is an important step and has to be performed carefully as it provides the critical values of the control parameters at which steady states lose or gain stability. Note that the coupled nonlinear system in the current analysis, i.e., Eq. (3.4), is a nonautonomous system with a harmonic excitation; therefore, the steady states will always be periodic in nature instead of being constants as in the case of an autonomous system. Since a linear stability analysis uses steady-state solutions, we first obtain the steady-state periodic solutions of the coupled nonlinear system using the method of harmonic balance, as presented next.

3.3.1 Analytical Solution Using the Method of Harmonic Balance

As mentioned earlier, we use the method of harmonic balance to get the steady-state periodic solutions of the current nonlinear system. Since linear methods are not sufficient to analyze systems expressing nonlinearity, the method of harmonic balance is employed to study the cubic nonlinearity embedded in our system. The method of harmonic balance works by representing a steady-state periodic solution of an ordinary or differential-algebraic equation system by a Fourier series, i.e., a combination of sinusoids [95]. The implementation of the method of hamronic balance for this system is presented below.

To proceed with the method of harmonic balance, we assume that the steady-state periodic solutions of Eq. (3.4) are synchronous with the external forcing on the system. The analysis of a duffing oscillator by Krack and Gross [95] revealed that a single harmonic term in the harmonic balance method could sufficiently capture the response of a forced duffing oscillator. Therefore, since our system contains the same form of nonlinearity, the solution of Eq. (3.4) can be assumed as

$$\{\mathbf{y}\}(\tau) = \{\mathbf{C}\}\cos(\Omega\,\tau) + \{\mathbf{D}\}\sin(\Omega\,\tau)\,, \tag{3.5}$$

with coefficient vector **C** and **D** are defined as

$$\mathbf{C} = \begin{bmatrix} C_1 & C_2 & C_3 & C_4 & C_5 & C_6 \end{bmatrix}^T\,, \quad \mathbf{D} = \begin{bmatrix} D_1 & D_2 & D_3 & D_4 & D_5 & D_6 \end{bmatrix}^T\,.$$

On substituting the assumed form of the solution in Eq. (3.4) we get

$$-\,\Omega\,\{\mathbf{C}\}\sin(\Omega t) + \Omega\,\{\mathbf{D}\}\cos(\Omega t) + \Omega[\mathbf{A}]\,\{\mathbf{C}\}\cos(\Omega t) + \Omega[\mathbf{A}][\mathbf{D}]\sin(\Omega t) + [\mathbf{N_1}] = \{\mathbf{F_{eq}}\}\,. \tag{3.6}$$

where $[\mathbf{A}]$ is a (6×6) matrix and both $[\mathbf{N_1}]$ and $[\mathbf{F_{eq}}]$ are (6×1) column vectors. $[\mathbf{N_1}]$ contains the nonlinear terms of the equation. These matrices are defined in Appendix B.

By equating the coefficients of sine and cosine to zero in Eqs. (3.6), we get the set of 12 simultaneous nonlinear algebraic equations in terms of coefficients of $\mathbf{C}$ and $\mathbf{D}$. These equations can be solved for $C_i s$ and $D_i s$, which further provide us the solution to nonlinear coupled system (Eq. (3.4)) by utilizing Eq. (3.5). Having obtained the steady-state solution to the nonlinear system, next, we present the linear stability analysis.

3.3.2 Linear Stability Analysis

To perform the linear stability analysis of steady-state periodic solutions, we provide a small perturbation to all steady-states as

$$y_i(\tau) = y_{is}(\tau) + \epsilon z_i(\tau)\,, \quad \text{for} \quad i = 1,\, 2,\, 3,\, 4,\, 5,\, 6 \tag{3.7}$$

where $y_{is}s$ are the steady-state solutions of the system (obtained using the method of harmonic balance) and $\epsilon z_i s$ ($<< 1$) represents small perturbations around the steady-states. Since the steady-state periodic solutions, i.e., $y_i(\tau)s$, of Eq. (3.4) satisfy Eq. (3.4), we get linearized equations in terms of perturbed and steady-state quantities as

$$z_1' = z_2\,, \tag{3.8a}$$

$$\begin{aligned} z_2' =& - z_1 k_{\mathrm{r1}} + z_3 k_{\mathrm{r1}} - z_1 k_{\mathrm{r2}} + z_5 k_{\mathrm{r2}} - 3y_{1s}^2 z_1 k_{\mathrm{rnl1}} - 3y_{1s}^2 z_1 k_{\mathrm{rnl2}} + 3y_{1s}^2 z_5 k_{\mathrm{rnl2}} + 6y_{5s} y_{1s} z_1 k_{\mathrm{rnl2}} \\ & - 6y_{5s} y_{1s} z_5 k_{\mathrm{rnl2}} - 3y_{5s}^2 z_1 k_{\mathrm{rnl2}} + 3y_{5s}^2 z_5 k_{\mathrm{rnl2}} + 2\zeta_1 z_2 - 2\zeta_2 z_2 + 2\zeta_2 z_4 - 2\zeta_3 z_2 + 2\zeta_3 z_6 - z_1\,, \end{aligned} \tag{3.8b}$$

$$z_3' = z_4\,, \tag{3.8c}$$

$$\begin{aligned} z_4' =& 3\alpha y_1^2 z_1 k_{\mathrm{rnl2}} - 3\alpha y_1^2 z_5 k_{\mathrm{rnl2}} - 6\alpha y_5 y_1 z_1 k_{\mathrm{rnl2}} + 6\alpha y_5 y_1 z_5 k_{\mathrm{rnl2}} + 3\alpha y_5^2 z_1 k_{\mathrm{rnl2}} - 3\alpha y_5^2 z_5 k_{\mathrm{rnl2}} + \alpha \mathrm{kr2} z_1 \\ & - \alpha \mathrm{kr2} z_5 + 2\alpha\zeta_3 z_2 - 2\alpha\zeta_3 z_6\,, \end{aligned} \tag{3.8d}$$

$$z_5' = z_6\,, \tag{3.8e}$$

$$z_6' = \alpha_2 z_1 k_{\mathrm{r1}} - \alpha_2 z_3 k_{\mathrm{r1}} - \alpha_2 z_3 k_{\mathrm{r3}} + 2\alpha_2\zeta_2 z_2 - 2\alpha_2\zeta_2 z_4 - 2\alpha_2\zeta_4 z_4\,. \tag{3.8f}$$

It should be noted here that the linearized equations, i.e., Eq. (3.8) involve time-periodic coefficients in terms of steady states, so it is difficult to get the closed-form expressions for the critical values of the control parameters. Therefore, we use Floquet theory to determine the stability of the steady-state periodic solutions numerically. A detailed discussion on the linear stability along with nonlinear tools to explore the dynamics of the coupled system is presented in the subsequent section.

3.4 Results and Discussions

In this section, we first compare the analytical solution (Eq. (3.5)) with the numerical simulation of the coupled HIM-HAS-NVAI system to establish the accuracy of the analytical approach. The analytical solution presented earlier is used to generate a linear stability curve of the system in parametric space. Afterwards, numerical bifurcation analyses of the system are used to examine the nonlinear dynamics of the system for the different values of the operating parameters, i.e., F and Ω. Finally, a parametric analysis is conducted to identify key design parameters of the system.

3.4.1 Validation of the Analytical Results from Method of Harmonic Balance

Table 3.1: Parameter values of the HIM–HAS–NVAI system (part 1).

Parameter	Value	Unit
m_H	1.7	kg
m_a	1.55	kg
m_s	0.049	kg
m_N	$0.02m_H$	kg
F_{ref}	300	N
ω_{ref}	26.1	Hz
b	$0.04m_H$	kg
k_H	3.0×10^8	Ns/m^3
k_N	2.5×10^6	Ns/m^3
x_0	5.72×10^{-5}	–

As mentioned earlier, the first part of this analysis involves the validation of the analytical results obtained using the harmonic balance method (HBM) (Eq. (3.5)) by comparing it against the direct numerical simulations of the coupled HIM-HAS-NVAI system (Eq. (3.4)). For this purpose, we compare the frequency-response curve of the primary system, i.e., HAS (y_a) obtained using HBM and numerically for the parameter values listed in Table 5.1. The mass of the HIM is chosen to represent the mass of a typical pneumatic chipping hammer, the other parameters of the Kelvin-Voigt model for the ground-stiffness interaction are chosen to represent parameters of a material acted on by a tool-bit. Furthermore, the linear and nonlinear parameters of the NVAI are determined by the H_∞ optimization method [89] and the principle of similarity [90, 94], respectively.

Since it is difficult to get the closed-form expressions of the coefficients in the analytical solution (Eq.(3.5)), we use the fixed arc-length continuation method [96] to get numerical values of the coefficients, of the analytical solution, at different values of the excitation frequency

Table 3.2: Parameter values of the HIM–HAS–NVAI system (part 2).

Parameter	Value	Unit
k_{HL}	3.0×10^5	N/m
k_a	4279	N/m
k_s	62804	N/m
k_{NL}	13280	N/m
c_H	50	Ns/m
c_a	76	Ns/m
c_s	192.90	Ns/m
c_N	9.3	Ns/m
w_1	414.12	–
α_2	1.12	–
ζ_4	0.052	–
α	17.15	–
ζ_1	0.034	–
ζ_2	0.13	–
k_{r1}	0.21	–
k_{r2}	0.052	–
ζ_3	0.0083	–
k_{rnl1}	3.27×10^{-6}	–
k_{rnl2}	1.90×10^{-8}	–
k_{r3}	0.014	–

for a given value of excitation amplitude. While for the numerical simulations, we have used MATLAB's numerical ode solver 'ode45' with high relative and absolute tolerance values. To get the amplitude-frequency response numerically, we uniformly divide the nondimensional excitation frequency, Ω, in a given range. For each value of Ω, numerical simulations are run for a sufficient time to get rid of the system's transient response. Thereafter, the peaks of the time response y_a are plotted for each value of Ω. The comparison between both approaches has been shown in Fig. 3.2. From Fig. 3.2, we observe that the response of the system using the analytical approach, HBM, excellently matches with the response of the system using the numerical approach. Having shown that the steady state responses of the system can be approximated using HBM, we will use the analytical solution (Eq. (3.5)) in the remainder of the analysis unless otherwise stated.

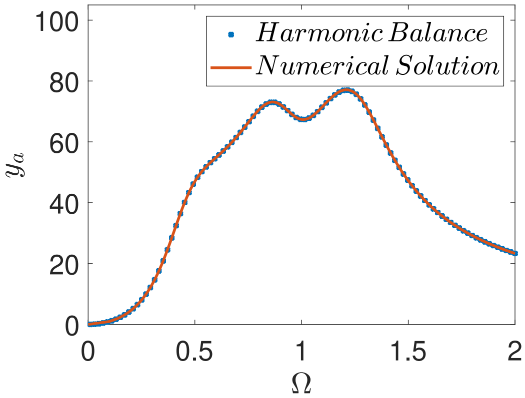

Figure 3.2: Comparison of analytical and numerical solution for $F = 100$ and parameter values listed in Table 5.1.

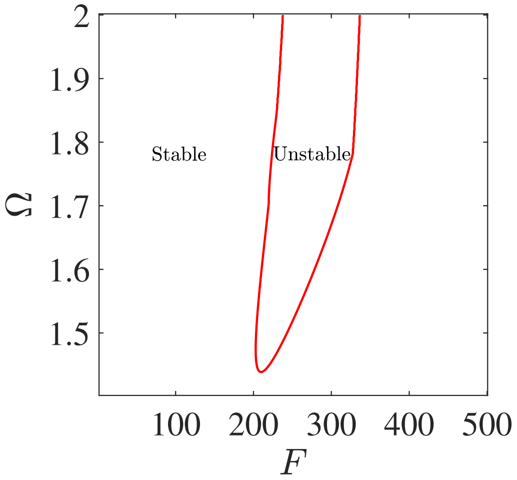

Figure 3.3: Stability curve in $F - \Omega$ space for the parameter values listed in Table 5.1.

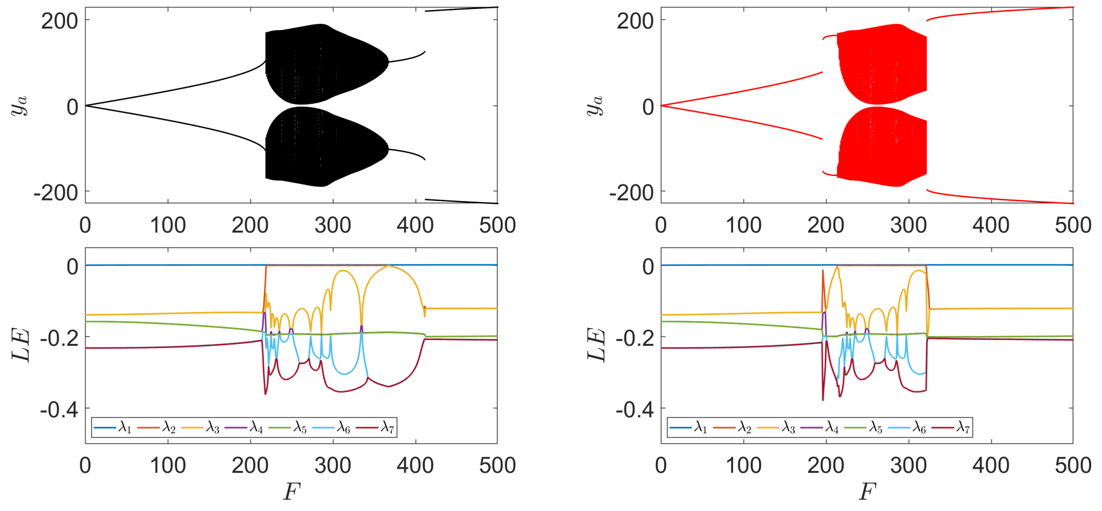

(a)

(b)

Figure 3.4: Bifurcation diagram and its corresponding Lyapunov exponent spectrum for (i)forward sweep and (ii)backward sweep with $\Omega = 1.6903$ and parameter values listed in Table 5.1.

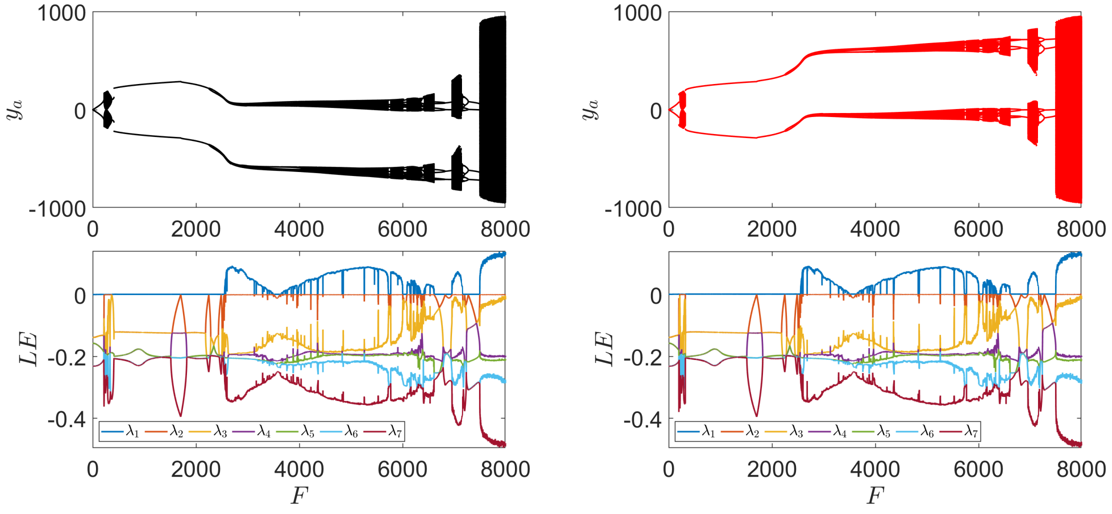

(a)

(b)

Figure 3.5: Bifurcation diagram and its corresponding Lyapunov exponent spectrum for (i)forward sweep and (ii)backward sweep with Ω set to 1.6903.

3.4.2 Linear Stability Curves

To perform the linear stability analysis of the current system, the complete set of linear ODE's from Eq. (3.8) can be written in a compact form as

$$\dot{\mathbf{x}}(\tau) = \mathbf{F}(\tau)\mathbf{x}(\tau)$$

where $\mathbf{F}(\tau)$ is a Jacobian matrix with time-periodic coefficients (due to the appearance of periodic steady-states) and $\mathbf{x}(\tau)$ is a state vector with components $\mathbf{x}(\tau) = [y_1, y_2, y_3, y_4, y_5, y_6]^T$.

To study the stability characteristics of the coupled system, we use Floquet theory. To generate the stability plot in $F - \Omega$ space, we divide the given range of F and Ω in 1000×500 sub-regions with 1000 discrete points along the $F-$axis and 500 discrete points along the $\Omega-$axis. Next, we run the simulation to generate the fundamental matrix and obtain the Floquet multipliers, $f_i s$, as the eigenvalues of the fundamental matrix. For each point, we check the magnitude of the dominant Floquet multiplier. If the magnitude of the dominant Floquet multiplier is less than one, then the system is stable, and if it is greater than one, it becomes unstable. Therefore, the stability boundary is defined as the locus of operating points corresponding to the dominant Floquet multiplier with magnitude one. After evaluating the dominant Floquet multiplier at every point, the boundary, separating the stable and unstable region, is plotted and shown in Fig. 3.3. From Fig. 3.3, we observe the transitions in the stability of the periodic steady-states after certain threshold frequencies. To understand the dynamics involved with these transitions, bifurcation diagrams and Lyapunov spectrums are generated and discussed in the next section.

3.4.3 Bifurcation Analysis

For the numerical bifurcation analysis, we have used MATLAB's ODE solver 'ode45' with high values of relative and absolute tolerances, '10^{-8}', to solve our first-order system of ODE's. These bifurcation diagrams can be plotted by fixing either of the control parameters, i.e., F or Ω, and varying the other. In the current work, we fix Ω ($\Omega = 1.6903$), and vary F in forward/increasing and backward/decreasing directions. To perform the above-mentioned step, we uniformly divide the bifurcation parameter, F, in a given range and run the numerical simulations for a sufficient time to capture the steady-state response of the system at each value of F in both directions. Note that for both forward and backward sweeps, the system's final response for a previous bifurcation parameter is used as the initial condition for the numerical simulation corresponding to the next value of the bifurcation parameter. These bifurcation diagrams, showing the extrema of the hand-arm system's motion, i.e., y_5 (corresponding to $y_6 = 0$) are depicted in Figs. 3.4 and Fig. 3.5 for relatively low and high values of F, respectively.

Figure 3.4 shows the bifurcation diagram for $F : 0 - 500$ in forward and backward direction. From Fig. 3.4, we can observe that the system loses and regains lyapunov stability. The Lyapunov stable region is also asymptotically stable as predicted by the stability plots (Fig. 3.3). We further observe the appearance of quasi-periodic motions in the unstable region. The appearance of these quasi-periodic motions can be further confirmed by plotting the variation of Lyapunov exponents. The Lyapunov exponents (LE) of the system are obtained using the method proposed by Wolf et al.[97]. The Lyapunov exponents for this system are obtained with the equations of motion transformed to an autonomous form.

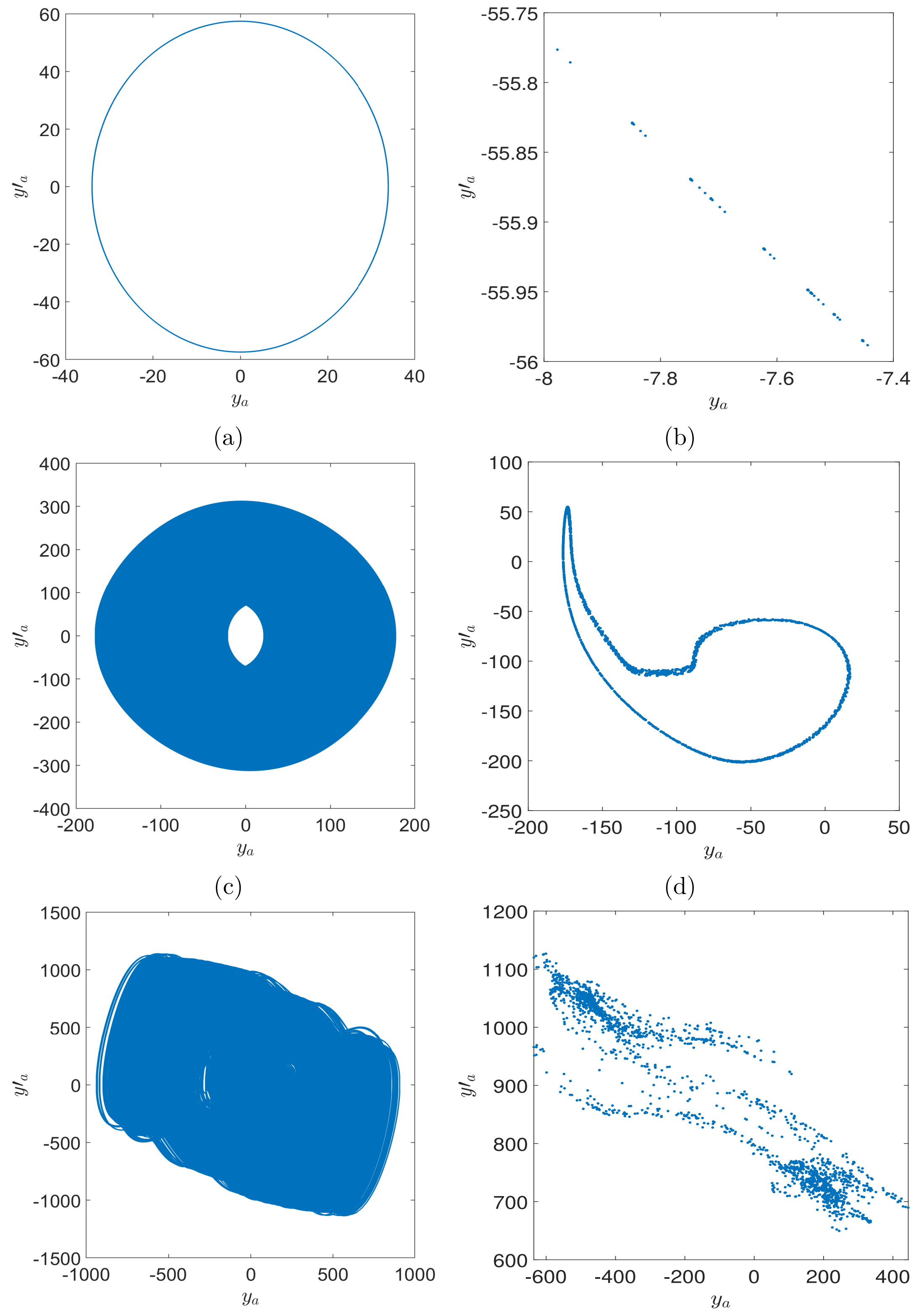

(a) (b)

(c) (d)

(e) (f)

Figure 3.6: Phase potraits for (i)periodic($F = 100$), (iii)quasi-periodic($F = 300$) and (v) chaotic motion($F = 7900$), and their corresponding Poincare maps for (ii)periodic, (iv)quasi-periodic and (vi) chaotic motion for Ω set to 1.6903 are shown. These dynamics correspond to the dynamics obtained via a forward sweep.

The regions of F for which the largest LE is zero and the other LE's are negative correspond to periodic solutions. While the values of F where the two largest LE's are zero and the other LE's are negative correspond to quasi-periodic solutions [98, 99]. From the Lyapunov spectrum shown in Fig. 3.4, we can observe that the two largest Lyapunov exponents become zero in the unstable regions, signifying the existence of the quasi-periodic solutions. This observation further verifies our bifurcation and linear stability analyses.

Having established the existence of quasi-periodic solutions in the unstable region, next, we present systems' dynamics for larger values of excitation amplitude (F) $\Omega = 1.6903$, and is shown in Fig. 3.5 for forward and backward sweeps. This step is performed to explore the dynamics resulting from a change in the stability of the steady periodic solution. From Fig. 3.5, we can observe that the steady periodic solutions lose stability at higher values of F through quasi-periodic solutions, as two of the dominant Lyapunov exponent becomes zero. Furthermore, chaotic attractors begin to appear in the system when the quasi-periodic solutions lose their stability. The existence of a chaotic attractor can be further confirmed by the Lyapunov exponent, as the dominant Lyapunov exponent becomes greater than zero. To further confirm the appearance of periodic, quasi-periodic, and chaotic solutions, as indicated by the numerical bifurcation diagrams and Lyapunov exponents, phase portraits and Poincare sections are generated and are shown in Fig. 3.6. From Fig. 3.6, the appearance of periodic motion is confirmed through a closed circular curve on the phase portrait and a set of points on the Poincare section. Also, quasi-periodic and chaotic motions are correctly depicted as a closed curve and a scattered group of points on the Poincare section, respectively. Phase portraits aptly describe quasi-periodic and chaotic motion as dense attractors; however, the Poincare section provides a map that shows a clearer distinction between chaotic and quasi-periodic motions. Next, we explore the effects of different absorber parameters on the performance of the system.

3.5 Parametric Analysis

In this section, we examine the effects of the absorber parameters on the safe operating region in the parametric space of $F - \Omega$ to avoid the appearance of quasi-periodic and chaotic motion in the coupled HIM-HAS-NVAI system.

Note that if the HAS was modeled as a continuous system, it would consist of multiple natural frequency components. Therefore, when the system is in operation, it would be unsatisfactory if one of the natural frequency components of the HAS matches with one of the frequency components of quasi-periodic or chaotic motion exhibited by the system. Such occurrences could lead to resonance and increase the risk of injury to the HAS. Based on bifurcation diagrams and Lyapunov spectrums for the system (Fig. 3.4 and 3.5), it has been observed that it is indeed possible for the system to exhibit quasi-periodic and chaotic motion and hence, the possibility of resonance. Therefore, it is desirable to select the absorber parameters such that the appearances of quasi-periodic or chaotic motion can be avoided.

Since Floquet multipliers only provide the information about the stability of steady-state periodic solutions of the system, we use the Lyapunov exponents to characterize the systems' behavior in the parametric space of $F - \Omega$. This further helps us to determine safe (only periodic solutions) and unsafe (quasi-periodic and chaotic attractors) regions in the parametric space. As mentioned earlier, for periodic motions, the largest LE is zero, and the other LE's are negative, and for quasi-periodic motions, the two largest LE's are zero, and the other LE's are negative. Whereas, for chaotic motions, the leading Lyapunov exponent is positive. Therefore, the boundary separating the safe and unsafe region corresponds to the set of parameters for which the condition for periodic motion is not satisfied. This parametric space within which the system's safe and unsafe operating region is identified will be referred to as a Lyapunov chart.

From Fig. 3.5i and ii, we observe that for the forward and backward sweeps, both the Lyapunov spectrums and bifurcation diagrams detect different ranges of F for the onsets of quasi-periodic and chaotic motions. Therefore, to determine the safe operating region in the parametric space of $F - \Omega$, the Lyapunov chart is obtained by both forward and backward sweeps for the system parameter values listed in Table 5.1. To obtain the Lyapunov charts in both forward and backward sweeps, we divide the parametric space into 60 discrete points along the Ω-axis and 50 discrete points along the F-axis. For each value of Ω between 1.4 and 2, the Lyapunov exponents are obtained for different values of F between 0 and 500 in both forward and backward sweeps. Finally, with the use of these Lyapunov exponents, we obtain the boundary between the safe and unsafe operating region of the system.

Based on Figures 3.7i and ii, we can observe that the Lyapunov chart in backward sweep detects the onset of chaotic or quasi-periodic motion earlier (with regards to F) than the Lyapunov chart obtained by forward sweep. In this study, we would like to detect the early onset of the unsafe operation region of the system. Therefore, the Lyapunov chart obtained by a backward sweep will be used for further analysis. Next, the effect of different absorber parameters on the system's performance is characterized using the Lyapunov chart.

The effect of k_{rnl2} on the performance of the absorber is shown in Fig. 3.8. From this figure, we observe that the area of the unsafe operating region increases with an increase in k_{rnl2} till the value of $k_{rnl2} = 1.9e - 8$. When k_{rnl2} is increased past $1.9e^{-8}$, the area of the unsafe operating region starts decreasing. This observation implies that for given system parameters, there is a critical value of k_{rnl2}, which maximizes the unsafe operating region.

In this work, we set two criteria for an efficient design of the NVAI: delay of the onset of the unsafe operating region as the primary criteria and minimization of the area of the unsafe operating region as the secondary criterion. From Fig. 3.8, we can observe that smaller values of k_{rnl2} satisfy the criteria set, and hence can be selected for an efficient absorber

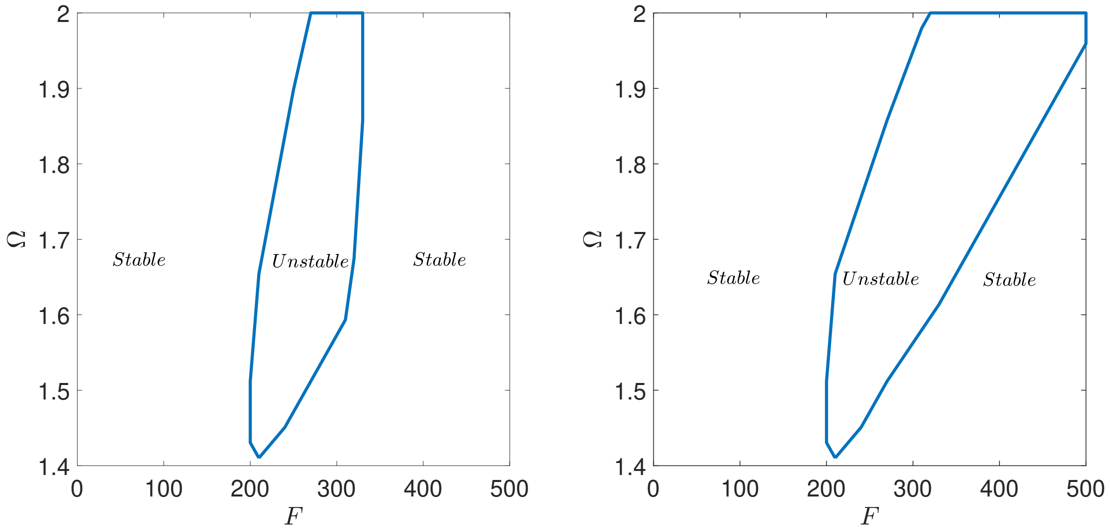

(a) (b)

Figure 3.7: Lyapunov chart used to highlight different regimes of motion of the system in the parametric space Ω-F obtained via i)a backward sweep and ii)a forward sweep.

design.

Next, a quantitative examination of the effect of varying values of k_{rnl2} on the system's dynamics is shown through bifurcation diagrams (Fig. 3.8). From Fig. 3.8 (ii), (iii) and (iv), we can observe that the value of F (x-coordinate) corresponding to the first instance of a significant jump in the amplitude of a periodic solution (A_1, B_1 and C_1) increases with increase in k_{rnl2}. Furthermore, the point corresponding to the second jump to higher amplitude periodic motion from quasi-periodic or periodic oscillations (A_2, B_2 and C_2) decreases with increase in k_{rnl2}. Further, the value of F corresponding to the onset of quasi-periodic motion begins to move towards the first location of the sudden jump in the amplitude of periodic solutions as k_{rnl2} increases. This further implies the early onset of the unsafe operating region as the k_{rnl2} increases.

Next, the effect of ζ_3 on the performance of the absorber is shown through Fig. 3.9. From Fig. 3.9, we can observe that the area of the unsafe operating region of the system increases with an increase in ζ_3 up to $\zeta_3 = 0.0083$. After this value of ζ_3, the area of the unsafe operating region starts decreasing. This further implies that for the system parameter values listed in Table 5.1, the critical value of ζ_3 is 0.008, which maximizes the unsafe operating region. Also, as ζ_3 increases, the value of F corresponding to the onset of unsafe operating region increases. This observation further implies that the larger values of the absorber nondimensional damping, ζ_3, satisfy the subjective criteria defined earlier for an efficient absorber design.

Similar to the case of k_{rnl2}, bifurcation diagrams are used to assess the quantitative effect of varying values of ζ_3 on the performance of the system. Based on Figures 3.9 ii, iii and iv, we can observe that an increase in value of ζ_3 results in an increase in the distance between the values of F corresponding to the first (D_1, E_1, G_1) and second instance (D_2, E_2, G_2) of the sudden jump in the response of the system. Furthermore, the higher value of ζ_3 delays the onset of the quasi-periodic motions and hence, satisfies the design criteria for an efficient absorber.

Finally, the role of α on the performance of the system is presented through Fig. 3.10. The results show that decreasing values of α from 22.2 to 17.2 causes an increase in the area of the unsafe operating region of the system. However, when the value of α is decreased past 17.2, the size of the unsafe operating region of the system starts decreasing. Also, as the value of α decreases, the values of F spanned by the unsafe operating region increase. Thus, it can be seen that the smaller values of the α satisfy the subjective criteria defined earlier for having an efficient absorber design. Similar to the previous parametric studies, we now explore the effects of varying α on the system's performance using bifurcation diagrams. As α is increased from 13.3 to 14.7, the distance between the F values for the first and second location where there is a jump to higher amplitude motion decreases. Then at $\alpha = 22.2$, only one location now exists where there is a significant jump to high amplitude motion, i.e., at K_2.

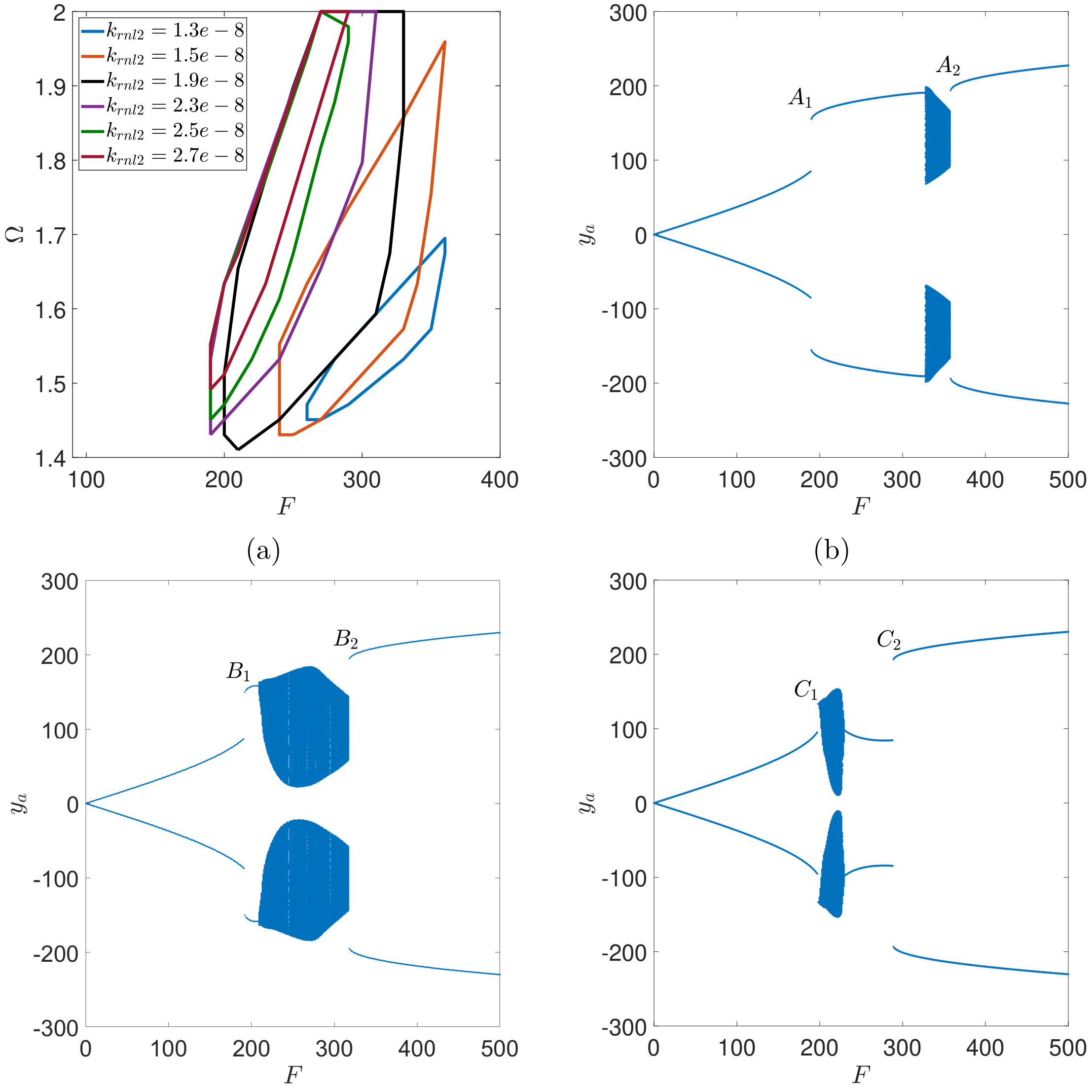

(a) (b)

(c) (d)

Figure 3.8: i) Comparison of Lyapunov chart for different values of k_{rnl2}. Bifurcation diagrams for $\Omega = 1.64$ and k_{rnl2}= ii)$1.3e-8$, iii)$1.9e-8$ and iv)$2.7e-8$. The values of the x-coordinates of A_1, A_2, B_1, B_2, C_1 and C_2 are 189, 358, 192, 318, 198 and 289 respectively.

The results of this parametric study imply that the absorber properties related to the above studied nondimensional parameters, i.e., the absorber's stiffness, damping and inertance, can be appropriately tuned to increase the safe operating region in the parametric space of $F-\Omega$.

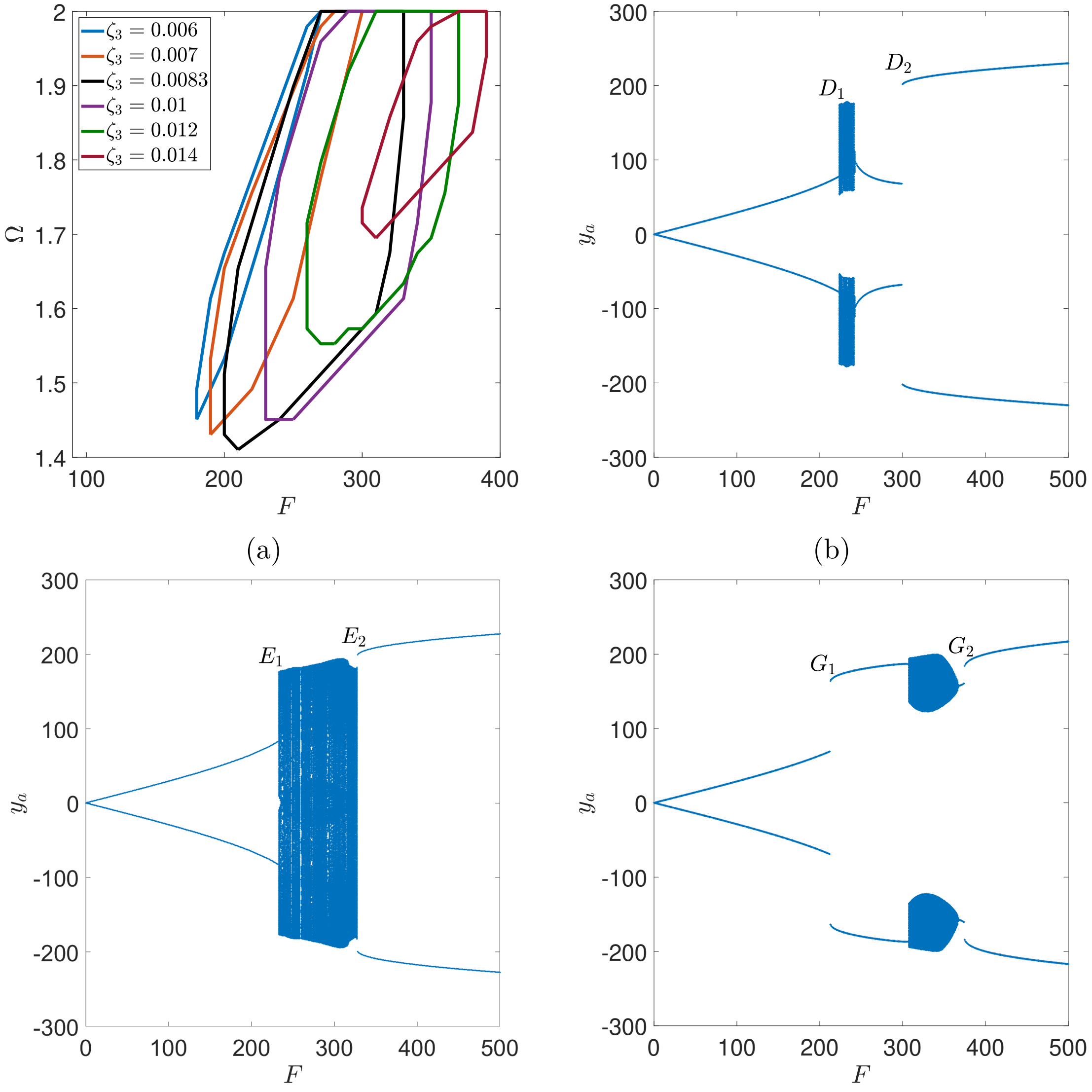

(a) (b)

(c) (d)

Figure 3.9: i) Comparison of Lyapunov chart for different values of ζ_3. Bifurcation diagrams for $\Omega = 1.8$ and ζ_3= ii)0.006, iii)0.0083 and iv)0.014. The values of the x-coordinates of D_1, D_2, E_1, E_2, G_1 and G_2 are 224, 300, 233, 328, 213 and 375 respectively

Also, as revealed by the bifurcation diagrams, the absorber parameters can be appropriately selected to delay or hasten the onset of a jump in the amplitude of the system's motion when F is used as a bifurcation parameter.

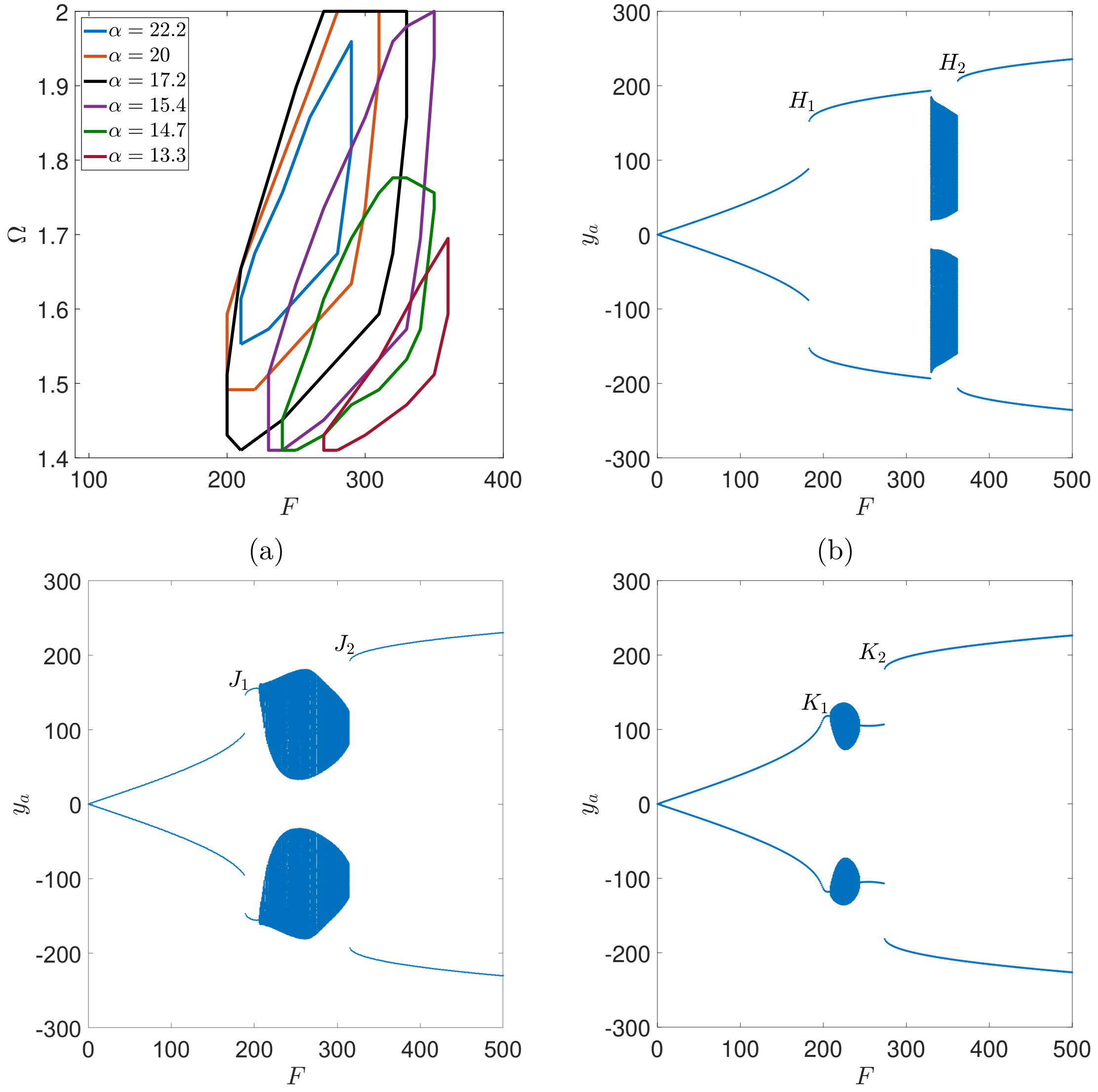

(a) (b)

(c) (d)

Figure 3.10: i) Comparison of Lyapunov chart for different values of α. Bifurcation diagrams for $\Omega = 1.6$ and α= i)13.3, ii)17.5 and iii)22.2. The values of the x-coordinates of H_1, H_2, J_1, J_2, K_1 and K_2 are 183, 362, 189, 315, 209 and 274 respectively.

3.6 Conclusion

In this study, a nonlinear absorber's ability to eliminate or reduce harmful transmission of vibrations from an HIM to the HAS was explored. The method of harmonic balance was used to get an analytical solution for the system. A linear stability analysis, which uses the analytical solution, was performed using Floquet theory. The system's linear stability analysis revealed unstable and stable regions in the parametric space of excitation amplitude vs. excitation frequency $(F-\Omega)$. Further exploration of the stable and unstable regions using bifurcation diagrams and a Lyapunov spectrum revealed periodic motion in the stable region and quasi-periodic motion in the unstable space. For a broader range of forcing amplitude parameters, i.e., for $F : 0-8000$, bifurcation diagrams, Lyapunov exponents, Phase portraits, and Poincare maps revealed the existence of chaotic solutions. These results also confirmed that Poincare maps better distinguish between quasi-periodic and chaotic motions than phase portraits.

Further, Lyapunov exponents were used to identify quasi-periodic and chaotic motion regions, also referred to as unsafe operating regions, in the excitation force amplitude-frequency $(F - \Omega)$ parametric space. Subsequently, a parametric study was performed to observe the effect of varying the absorber's parameters, k_{rnl2}, ζ_3 and α, on the area of the unsafe operating region of the system and on the delay of the onset of the unsafe operating region. This parametric study revealed that the largest value of the nondimensional parameter ζ_3, and the smallest value of α and k_{rnl2} meet the criteria for having the best absorber design parameters. A parametric study using bifurcation diagrams, with bifurcation parameter F, also revealed that a change in k_{rnl2}, ζ_3 and α could control the points at which a sudden jump in the nondimensional amplitude related to the displacement of the HAS occurs.

Chapter 4

Effectiveness of a Cubic Nonlinear Absorber on Curbing Vibrations to the Vibro-Impact Model of an Impact Tool via Nonlinear Analysis

This chapter was collaboratively developed by the following authors: **Ore Alabi**, **Dr. Sunit Kumar Gupta**, and **Dr. Oumar Barry**. The contributions, categorized according to the *CRediT (Contributor Roles Taxonomy)*, are as follows:

- **Conceptualization**: Ore Alabi, with guidance from Dr. Oumar Barry.
- **Methodology**: Ore Alabi, with feedback from Dr. Oumar Barry.
- **Formal Analysis**: Ore Alabi.
- **Investigation**: Ore Alabi.
- **Writing – Original Draft**: Ore Alabi.
- **Writing – Review & Editing**: Dr. Oumar Barry and Dr. Sunit Kumar Gupta.
- **Supervision**: Dr. Oumar Barry.

This chapter is edited from:

Alabi, O., Gupta, S. K., Barry, O. (2022, August). Dynamics of a Nonlinear Absorber and Hand-Held Impact Machine. In International Design Engineering Technical Conferences and Computers and Information in Engineering Conference (Vol. 86304, p. V009T09A022). American Society of Mechanical Engineers.

and

Alabi, O., Gupta, S. K., Barry, O. R. (2023). Vibration analysis of a nonlinear absorber coupled to a hand-held impact machine. Journal of Computational and Nonlinear Dynamics, 18(8), 081006.

4.1 Introduction

In various industries, including the construction and transportation industries, hand-held percussion machines such as chipping hammers, jackhammers, and rotary hammers are extensively utilized due to their adaptability, efficiency, and convenience in service. These machines rely on sequential impacts for the demolition or treatment of hard materials. However, during the operation of heavy hand-held impact machines (HHIM), a significant level of vibrations can be transmitted to the human hands, which can further cause severe injury to the operator's hands [100]. Prolonged exposure to such vibrations may lead to episodes of vascular, musculoskeletal, and neurological disorders termed hand-arm vibration syndromes (HAVS). In severe instances, HAVS can result in a loss of blood supply to the fingers, leading to gangrene and, eventually, amputation [80]. Therefore, the reduction of these vibrations transmitted to the human hand from the HHIM is essential. To mitigate the occurrence of HAVS, it is important to have a thorough understanding of the dynamics of the HHIM to aid in the development of methods to reduce vibrations from the hand-arm system (HAS). This is the focus of the current work.

When formulating control strategies to reduce or mitigate vibrations from the HHIM, it is often essential to incorporate a model for both the human hand-arm system and the HHIM. The lumped parameter model of the hand-arm system combined with the HHIM stands as one of the popular models in the existing literature, capturing the dynamics of the whole system [7, 8, 101]. This model's widespread acceptance stems from its ability to determine the principal dynamics of a system with less expensive computational resources. Further, another critical element in this analysis is the selection of a model that can precisely represent the qualitative dynamics between a percussive tool and the ground. The interaction models in the literature describing the vibro-impact nature of a percussive tool span from simple visco-elastic connections between ground and a tool to more intricate models, featuring cubic and nonsmooth nonlinearities [10–18]. In a step towards analyzing the complex dynamics of the HHIM, Alabi et al. [13, 14] employed a nonlinear lumped parameter model for an HHIM and hand-arm system, with visco-elastic ground interaction model consisting of spring and damping elements. Their model predominantly focused on cubic nonlinearity to represent the interactions between the HHIM and ground. They observed that a nonlinear vibration absorber could effectively diminish vibrations transmitted to the hand from such tools. However, given that the interaction between the HHIM and ground is characterized by intermittent impacts rather than continuous contact, a vibro-impact model might provide a more comprehensive depiction of the dynamics than the visco-elastic model.

Pavlovskaia *et al.* presented the vibro-impact models to predict the optimal static and dynamic force to obtain an optimal progression rate for drilling [11, 12]. Later, Aguiar *et al.* showed that a 7DOF vibro-impact system could reproduce experimental relations obtained between axial vibration peaks and mud flow rate for a drilling system [10]. Franca and

Weber presented a mathematical model, which considered only the percussive action of a resonance hammer, and were able to capture qualitative and quantitative results similar to experimental results [43]. Despite the acknowledged efficiency of the vibro-impact model in describing the accurate interactions between a percussive tool and the ground, there have been no attempts to control transmitted vibrations to the hand while modeling the interaction as the vibro-impact system. Therefore, this work, for the first time, seeks to understand system dynamics more accurately by incorporating a vibro-impact model of the interaction between a chipping hammer and the hand.

One of the prevalent methods to control undesirable vibrations is the tuned vibration absorber (TVA) [46]. A conventional tuned vibration absorber consists of a spring-mass system tuned to the dominant resonant frequency of a primary system. The efficacy of a TVA has been established in dynamical systems such as grass trimmers, power lines, and in manufacturing processes including milling and boring [21–26] due to its robust design, cost-effectiveness and ease of installation. However, a limitation of the TVA is its narrow frequency suppression bandwidth. This shortcoming in the TVA can be addressed by introducing a nonlinear element, resulting in a nonlinear tuned vibration absorber (NLTVA). The NLTVA has been found to have a wider suppression bandwidth in comparison to its linear counterpart [47, 48]. Since the operating frequency of the chipping hammer could vary during its operation (implying a broader frequency spectrum operation), an NLTVA is considered to be more effective in controlling vibrations from a vibro-impact chipping hammer model. Hence, a nonlinear absorber, more specifically with cubic nonlinearity, is explored in this work to determine its efficacy in suppressing the transmitted vibrations to the hand. The choice of cubic nonlinearity in the NLTVA is made to accommodate the fact that nonlinear behavior for vibro-impact systems is similar to that of a basic hardening system [52, 53].

Furthermore, studies have shown that the nonlinear vibration absorber is more effective in controlling the vibrations in HHIM [13, 14]. However, the effectiveness of the nonlinear vibration absorber has not been examined in scenarios where the HHIM-ground interactions are modeled as vibro-impact systems. Therefore, this study conducts a detailed nonlinear analysis to explore vibration control at the hand of a tool modeled with vibro-impact nonlinearities.

In this study, a lumped parameter model is proposed to describe the HHIM-HAS-NLTVA system dynamics in the axial direction as the dominant axis of the tool considered is in the axial direction[100]. A reduced order model of the percussive tool is introduced as a 2-DOF vibro-impact lumped parameter model, while the hand-arm system is modeled as a 2-DOF parameter model. The non-smooth system is smoothed via Filippov's method, and the system is analyzed qualitatively using nonlinear tools for different design parameters of the NLTVA.

It should be noted that the traditional method of selecting optimized absorber parameters using linear fixed point theory is not viable in our analysis. This conventional approach is suitable for linear absorbers in contrast to a non-smooth primary system studied in the current analysis. Consequently, our research aims to conduct a comprehensive parametric analysis, enabling us to assess the absorber's effectiveness in this novel application.

Towards addressing the aims listed above, the rest of the paper is organized as follows. In Section 5.1, a lumped parameter model of the HAS-HHIM-NLTVA system is presented along with the vibro-impact model of the ground-tool interaction. The smoothing of the non-smooth system and the bifurcation analysis of the system for different parameters are presented in Section 5.2. In Section 5.3, the significance of the results from Section 5.2 is discussed. Finally, some conclusions are drawn on the study in Section 5.3.

4.2 Model Development of HHIM–HAS–NLTVA System

A mathematical model showing how vibrations are transmitted from the HHIM to the HAS necessitates a model for both the combined HHIM-HAS-NLTVA system and the interaction forces between the HHIM piston and ground. The efficacy of lumped parameter models in capturing the dynamics of the HHIM, HAS, and NLTVA is well-established in the literature [9, 14, 19, 102]. However, it's pivotal to model the interaction forces between the HHIM piston and the ground accurately. Traditional models of interaction forces use a visco-elastic connection between the piston and the ground in the form of a spring and damper system. However, in the context of HHIM, the contact with the ground is intermittent rather than continuous. Thus, this study adopts the vibro-impact model for more precise modeling of the system.

4.2.1 Lumped Parameter Model of HHIM–HAS–NLTVA

Figure 4.1 illustrates the reduced-order model of the coupled HAS-HHIM-NLTVA system. In the schematic, the HHIM's bit/piston and housing are modeled as lumped masses, m_p and m_H. The buffer between the HHIM bit and casing is modeled as a visco-elastic connection with stiffness k_H and damping c_H. The numerical values of these parameters are adopted from [79]. In this model, we account for the feed force to press the machine against the material being worked on. The hand-arm system is depicted as a 2-DOF lumped-parameter model, which is accurate for frequencies below 100Hz [41]. Therefore, this model will be appropriate for our system, which operates at 45Hz. In the schematic, m_s and m_a signify the masses of the skin interfacing with the HHIM and the arm. The visco-elastic connection between them is modeled as spring and damper represented by k_s and c_s, respectively. The arm m_a connects to the body/trunk via spring (k_a) and damper (c_a). Parameters for the HHIM bit and casing are drawn from the model by Golysheva *et al.*[79] for a Hilti TE 74 operating at 45Hz. Additionally, the NLTVA is depicted as a lumped spring-mass-damper system, where m_N and c_N designate the absorber mass and linear viscous damper, respectively. Meanwhile, k_{NL} and k_N denote the linear and nonlinear stiffness of the NLTVA. Following this, we detail the vibro-impact model of the HHIM-ground interaction.

4.2.2 Non-Smooth Model for HHIM–Ground Interaction

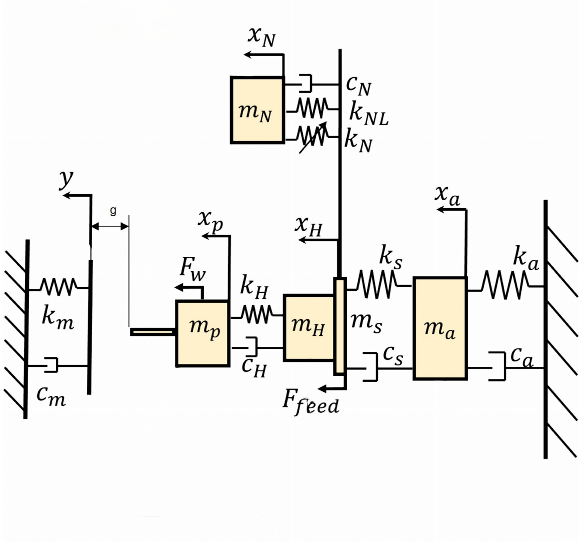

Figure 4.1: Schematic of the coupled system HHIM-HAS-NLTVA with vibro-impact model of interaction.

As mentioned earlier, to capture the HHIM dynamics associated with the percussive action of the HHIM bit, we adopt the vibro-impact model of the nonlinear interaction. This model specifies the interaction between the HHIM and ground material as a nonsmooth nonlinear process. Here, the ground material is represented as a linear spring-damper system with stiffness k_m and damping coefficient c_m [79, 103, 104], with an initial separation of g from the HHIM bit. Additionally, we assume that the ground material is restored before each successive impact, and the process of penetration of material is not taken into consideration. In this work, we consider concrete as the ground material with the stiffness and loss factors adopted from [79]. The modified coupled system of HHIM-HAS-NLTVA with this interaction model is depicted in Fig. 4.1.

Given the discontinuous nature of the HAS-HHIM-NLTVA system, its motion can be described by two distinct differential equation sets. One set of equations corresponds to the scenario when the HHIM bit is not in contact with the material, while the other set of equations corresponds to the case when the bit is in contact with the material. With f_m representing the contact force between m_p and the material and x_p as the motion of the HHIM bit, the interaction force f_m for these two different scenarios can be defined as

$$\begin{cases} x_p < g \text{ and } f_m = 0, \text{ without contact}, \\ x_p \geqslant g \text{ and } f_m = -\left(k_m y + c_m \dot{y}\right) < 0, \text{ with contact.} \end{cases} \tag{4.1}$$

Furthermore, similar to the discontinuous support system outlined by Leine [105], the ground in the current work achieves the equilibrium state if the HHIM bit is not in contact with the ground. Assuming that the relaxation time, the time period to attain the equilibrium state, of the ground is significantly shorter than the time between two successive contact events, we can disregard the free motion of the ground. Under these premises, if x_H, x_a, x_N, and y denote the motion of the HHIM casing, HAS, NVAI, and massless support/ground, respectively, then the governing equations of motion of the system are given by

$$\begin{aligned} &\left(m_H + m_s\right)\ddot{x}_H - \dot{x}_a c_s - x_a k_s - \dot{x}_p c_H - x_p k_H - \dot{x}_N c_N - k_{NL} x_N + \dot{x}_H \left(c_H + c_N + c_s\right) \\ &+ x_H \left(k_H + k_{NL} + k_s\right) + k_N \left(x_H - x_N\right)^3 = F_{feed}\,, \end{aligned} \tag{4.2a}$$

$$m_a\ddot{x}_a + \dot{x}_a\left(c_a + c_s\right) + x_a\left(k_a + k_s\right) - \dot{x}_H c_s - x_H k_s = 0\,, \tag{4.2b}$$

$$m_N\ddot{x}_N + c_N\left(\dot{x}_N - \dot{x}_H\right) + k_N\left(x_N - x_H\right)^3 + k_{NL}\left(x_N - x_H\right) = 0\,, \tag{4.2c}$$

$$\begin{aligned} &m_p\ddot{x}_p + \dot{x}_p\left(c_H + c_m\right) + \left(x_p - g\right)k_m + x_p k_H - \dot{x}_H c_H - x_H k_H = F_w \ (\text{with contact})\,,\\ &m_p\ddot{x}_p + \dot{x}_p c_H + x_p k_H - \dot{x}_H c_H - x_H k_H = F_w \ (\text{without contact})\,. \end{aligned} \tag{4.2d}$$

In the aforementioned governing equations of motion, F_{feed} represents the feed force applied to the HHIM by the operator, while F_w signifies the excitation force acting on the HHIM from the piston's reciprocating motion within. The analytical representation of F_w is sourced from experimental findings [78] and is given by

$$F_w = F_{ref}\left(\frac{\omega}{\omega_{ref}}\right)^2 \sin\left(\omega t\right). \tag{4.3}$$

Given the discontinuous nature of the contact force, an analytical solution of this set of coupled differential equations, Eq. (4.2), is complex. Hence, to comprehend the system's dynamics, a numerical method is employed for Eq. (4.2). To obtain numerical solutions for Eq. (4.2), the system is convexified into a differential inclusion by the Filippov theory [106] before numerically simulating the system using the switch model suggested by Leine [105]. Within this formulation, the state space $\mathbb{R}^n$ is split into two sub-spaces $\mathcal{V}_-$ and $\mathcal{V}_+$ by a hyper-surface Σ such that $\mathbb{R}^n = \mathcal{V}_- \cup \Sigma \cup \mathcal{V}_+$. The hyper-surface Σ, known as the switching boundary, is characterized by a scalar switching boundary function $h(\boldsymbol{x})^2$. The state $\boldsymbol{x}$ is in Σ when

$$h(\boldsymbol{x}) = 0 \Longleftrightarrow \boldsymbol{x} \in \Sigma.$$

The subspaces $\mathcal{V}_-$ and $\mathcal{V}_+$ and the switching boundary Σ can be formulated as

$$\begin{aligned}
\mathcal{V}_- &= \{\boldsymbol{x} \in \mathbb{R}^n \mid h(\boldsymbol{x}) < 0\}\,,\\
\Sigma &= \{\boldsymbol{x} \in \mathbb{R}^n \mid h(\boldsymbol{x}) = 0\}\,,\\
\mathcal{V}_+ &= \{\boldsymbol{x} \in \mathbb{R}^n \mid h(\boldsymbol{x}) > 0\}\,.
\end{aligned}$$

Therefore, a discontinuous differential equation can be cast as:

$$\dot{\boldsymbol{x}}(t) \in \boldsymbol{F}(t, \boldsymbol{x}(t)) = \begin{cases} \boldsymbol{f}_-(t, \boldsymbol{x}(t)), & \boldsymbol{x} \in \mathcal{V}_-, \\ \overline{co}\left\{\boldsymbol{f}_-(t, \boldsymbol{x}(t)), \boldsymbol{f}_+(t, \boldsymbol{x}(t))\right\}, & \boldsymbol{x} \in \Sigma \\ \boldsymbol{f}_+(t, \boldsymbol{x}(t)), & \boldsymbol{x} \in \mathcal{V}_+ \end{cases}$$

where the convex set is defined as

$$\overline{\text{co}}\left\{\boldsymbol{f}_-, \boldsymbol{f}_+\right\} = \left\{(1-q)\boldsymbol{f}_- + q\boldsymbol{f}_+, \forall q \in [0, 1]\right\}.$$

It should be noted in this system that separate conditions are required for the HHIM bit mass (m_p) to initiate contact with the ground and for the bit mass to lose contact with the ground. The switching boundary Σ is made up of the union of Σ_α and Σ_β. Further, the two boundary functions for the switching boundaries are defined as:

$$\begin{aligned}
h_\alpha(x_p, \dot{x_p}) &= x_p - g, \\
h_\beta(x_p, \dot{x_p}) &= k_m(x_p - g) + c_m \dot{x_p}
\end{aligned} \tag{4.4}$$

The mass is not in contact with the support if $\boldsymbol{x} \in \mathcal{V}_-$, with

$$\mathcal{V}_- = \left\{\boldsymbol{x} \in \mathbb{R}^2 \mid h_\alpha(x_p, \dot{x_p}) < 0 \text{ or } h_\beta(x_p, \dot{x_p}) < 0\right\} \qquad \text{no contact,}$$

and the mass is in contact with the support if $\boldsymbol{x} \in \mathcal{V}_+$, with

$$\mathcal{V}_+ = \left\{ \boldsymbol{x} \in \mathbb{R}^2 \mid h_\alpha(x_p, \dot{x_p}) > 0 \text{ and } h_\beta(x_p, \dot{x_p}) > 0 \right\} \qquad \text{contact.}$$

The switching boundary Σ_α is defined by

$$\Sigma_\alpha = \left\{ \boldsymbol{x} \in \mathbb{R}^2 \mid h_\alpha(x_p, \dot{x_p}) = 0, h_\beta(x_p, \dot{x_p}) \geq 0 \right\}.$$

While the switching boundary Σ_β is defined by

$$\Sigma_\beta = \left\{ \boldsymbol{x} \in \mathbb{R}^2 \mid h_\alpha(x_p, \dot{x_p}) \geq 0, h_\beta(x, \dot{x}) = 0 \right\}.$$

With f_+ and f_- obtained as:

$$f_+(\boldsymbol{x}, t) = \begin{bmatrix} \dot{x}_H \\ \frac{1}{m_H + m_s} \left(\dot{x}_a c_s + x_a k_s + \dot{x}_p c_H + x_p k_H + \dot{x}_N c_N \right. \\ + k_{NL} x_N - \dot{x}_H \left(c_H + c_N + c_s \right) - x_H \left(k_H + k_{NL} + k_s \right) \\ \left. - k_N \left(x_H - x_N \right)^3 + F_{feed} \right) \\ \dot{x}_a \\ \frac{1}{m_a} \left(-\dot{x}_a \left(c_a + c_s \right) - x_a \left(k_a + k_s \right) + \dot{x}_H c_s + x_H k_s \right) \\ \dot{x}_N \\ \frac{1}{m_N} \left(-c_N \left(\dot{x}_N - \dot{x}_H \right) - k_N \left(x_N - x_H \right)^3 - k_{NL} \left(x_N - x_H \right) \right) \\ \dot{x}_p \\ \frac{1}{m_p} \left(-\dot{x}_p \left(c_H + c_m \right) - \left(x_p - g \right) k_m - x_p k_H + \dot{x}_H c_H \right. \\ \left. + x_H k_H + F_w \right) \end{bmatrix} \tag{4.5}$$

$$f_{-}\left(\boldsymbol{x},t\right)=\begin{bmatrix} \dot{x}_H \\ \frac{1}{m_H+m_s}\left(\dot{x}_a c_s + x_a k_s + \dot{x}_p c_H + x_p k_H + \dot{x}_N c_N + k_{NL} x_N\right. \\ -\dot{x}_H\left(c_H + c_N + c_s\right) - x_H\left(k_H + k_{NL} + k_s\right) \\ \left.-k_N\left(x_H - x_N\right)^3 + F_{feed}\right) \\ \dot{x}_a \\ \frac{1}{m_a}\left(-\dot{x}_a\left(c_a + c_s\right) - x_a\left(k_a + k_s\right) + \dot{x}_H c_s + x_H k_s\right) \\ \dot{x}_N \\ \frac{1}{m_N}\left(-c_N\left(\dot{x}_N - \dot{x}_H\right) - k_N\left(x_N - x_H\right)^3 - k_{NL}\left(x_N - x_H\right)\right) \\ \dot{x}_p \\ \frac{1}{m_p}\left(-\dot{x}_p\left(c_H\right) - x_p\left(k_H\right) + \dot{x}_H c_H + x_H k_H + F_w\right) \end{bmatrix} \tag{4.6}$$

The numerical solutions for our system are obtained using the switch model proposed by Leine *et al.* [107]. The Switch Model introduces a band of thickness 2η around Σ, thereby allowing the efficient numerical approximation of the system's dynamics.

Table 4.1: Parameter values of the HHIM-HAS-NLTVA system used for simulations.

Parameter	Value	Unit	Parameter	Value	Unit	Parameter	Value	Unit
m_H	8	kg	k_H	495020	N/m	c_H	212	Ns/m
m_a	1.55	kg	k_a	4279	N/m	c_a	76	Ns/m
m_s	0.049	kg	k_s	62804	N/m	c_s	193	Ns/m
m_N	$0.02m_H$	kg	k_{NL}	14549	N/m	c_N	9.3	Ns/m
F_{ref}	500	N	ω_{ref}	45	Hz	g	0.02	m
m_p	0.35	kg	k_N	2.5×10^6	N/m^3	F_{feed}	250	N
–	–	–	k_m	3×10^7	N/m	c_m	4536	Ns/m

4.3 Results

In this section, we investigate the capability of the NLTVA to control vibrations transmitted from the HHIM to the hand-arm system by simulating the system dynamics under various operational conditions. For this purpose, we use bifurcation diagrams and phase portraits, illustrating the transitions in the system dynamics with different operating parameters. In particular, a parametric analysis, focusing on the effect of the NLTVA parameters, is performed to investigate the bifurcation of the system with forcing (F_{ref}) as a bifurcation parameter for a given excitation frequency. Finally, we explore the impact of feed force on the dynamics of the system.

To get the bifurcation diagram, we employed MATLAB's ODE solver 'ode45' with the relative and absolute tolerances set to 10^{-8}. This step ensured an accurate numerical solution for our system of first-order ODEs. To plot the bifurcation diagram, we fixed one of the operating parameters, in this case, operating frequency (ω), and evolved the system numerically to a steady state for different values of another parameter, in this case F_{ref} or F_{feed}. Following this, we obtained the Poincaré section by synchronously sampling the system's motion with the excitation frequency (ω). These sampled points, representing the system's steady state, were plotted on the y-axis of the bifurcation diagram, while the corresponding bifurcation parameter values were plotted on the x-axis. Unless specified differently in the figure captions, the parameters employed for the analysis are listed in Table 5.1.

In the first step, we evaluate the effect of the addition of the NLTVA to the HHIM on controlling hand-arm vibration.

4.3.1 Effect of Absorber Addition

As an initial step towards evaluating the effectiveness of the NLTVA to reduce hand-arm vibrations, we present a bifurcation analysis of the system, both with and without the absorber attached to the HHIM. For the current analysis, we use F_{ref} as the bifurcation parameter and set the excitation frequency at $\omega = 47$ Hz. From the results, illustrated in

Fig.4.3, we can observe that for lower values of F_{ref}, the absorber controls vibrations to a degree of 0.035mm, indicating moderate effectiveness. However, in the range of $F_{ref} = 445 - 536N$, the NLTVA significantly reduces the amplitude of hand-arm vibrations to a degree of 0.7mm (see Figs 4.3(ii) and (iv)), making the absorber more effective for higher values of F_{ref}. Additionally, the inclusion of the NLTVA in the HHIM decreases the onset point of period doubling cascades beyond $F_{ref} = 536N$. It should be noted that these simulations are performed for the given set of parameters in Table 5.1, suggesting the need for a parameteric analysis of the absorber parameters to identify key design parameters.

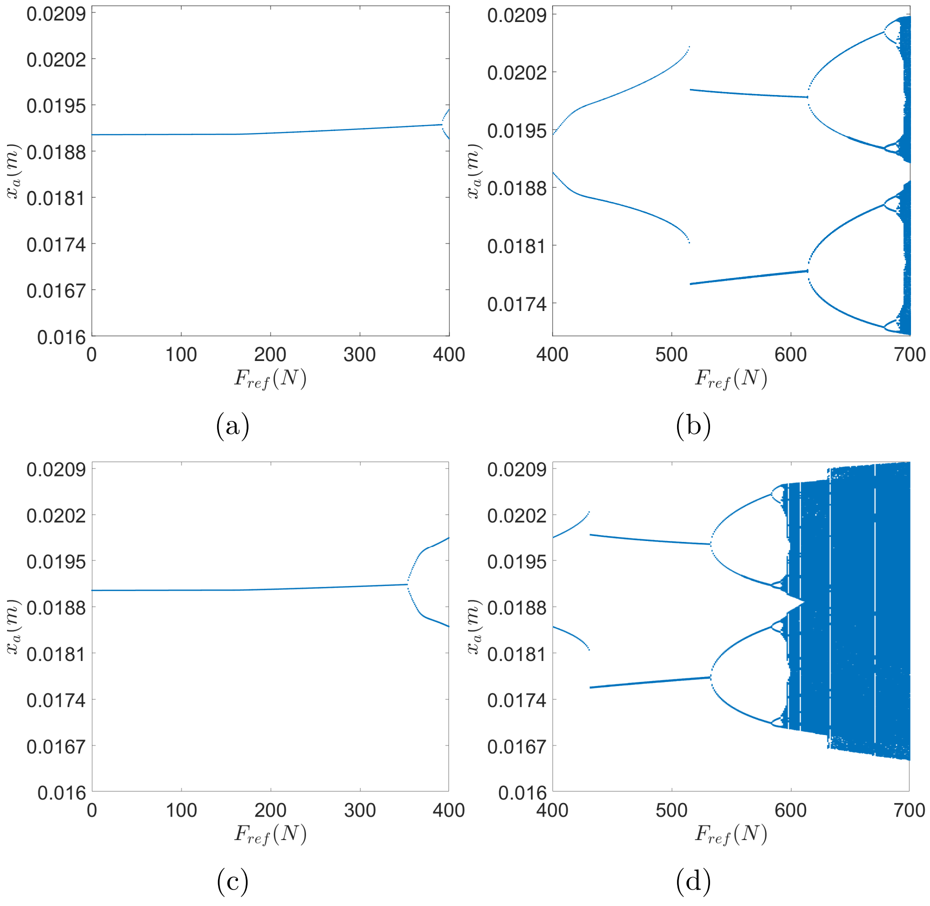

(a) (b)

(c) (d)

Figure 4.2: Bifurcation diagrams for $\omega = 47$ Hz with (i), (ii) no absorber, (iii) and (iv) absorber. These diagrams show the bifurcation parameters at which the periodicity and amplitude of the system changes with the addition of the NLTVA.

4.3.2 Parametric Study of k_N

The bifurcation diagrams for the hand-arm system response, with F_{ref} as the bifurcation parameter, are illustrated in Fig.4.3. For this analysis, we fixed the excitation frequency at $\omega = 47$ Hz and plotted bifurcation diagrams for two distinct values of k_N: $k_N = 0$ and $k_N = 2.5 \times 10^6, \text{N/m}^3$. From Fig.4.3, it is evident that for both values of k_N at $\omega = 47$ Hz, the period-1 solution loses stability, transitioning to a period-2 and eventually an aperiodic solution via period-doubling bifurcations. A detailed examination of Fig.4.3 reveals that the value of F_{ref} corresponding to the period-doubling bifurcation (e.g., point A) decreases with an increase in the cubic stiffness of the absorber. Specifically, in the absence of the cubic nonlinearity, the first period-doubling bifurcation occurs from period-1 to period-2 solutions at $F_{\text{ref}} = 390\,\text{N}$, and then from period-2 to period-4 at $F_{\text{ref}} = 613\,\text{N}$. Introducing the nonlinear absorber reduces these thresholds to $F_{\text{ref}} = 350\,\text{N}$ and $F_{\text{ref}} = 532\,\text{N}$ for period-1 to period-2 and period-2 to period-4, respectively. Additionally, the value of the excitation force corresponding to the jump in the amplitude of the period-2 solution, i.e., point B, decreases with the addition of the absorber from $F_{\text{ref}} = 514\,\text{N}$ to $F_{\text{ref}} = 431\,\text{N}$. Interestingly, depending on the forcing amplitudes, the absorber can either amplify or mitigate the hand-arm vibration amplitude. For instance, at point C, introducing the nonlinearity in absorber increases the amplitude by 0.3 mm, whereas at $F_{\text{ref}} = 500\,\text{N}$ (point D), it reduces the amplitude by 0.8 mm. To better understand this transition, we present the phase portraits showing the progression from periodic to aperiodic solutions via period-doubling bifurcation in Figs.4.4 and 4.5 for $k_N = 0$ and $k_N = 2.5 \times 10^6\,\text{N/m}^3$, respectively.

Furthermore, in pneumatically-controlled HHIM operations, the operating frequency may deviate due to manufacturing variances. To provide a comprehensive analysis, we investigate the system dynamics at the lower bound of frequency for this equipment, i.e., $\omega = 43\,\text{Hz}$ for the two distinct k_N values mentioned above. The resulting bifurcation diagram is shown in Fig. 4.6. It is noteworthy that at this frequency, the system maintains periodicity across a broad spectrum of excitation amplitudes for both values of k_N. However, with increasing excitation force, this periodic motion becomes unstable via period-doubling bifurcation. Notably, similar to the trends observed at $\omega = 47\,\mathrm{Hz}$, introducing nonlinearity into the absorber lowers the threshold for period-doubling bifurcation and may also lead to a reduced system amplitude within the periodic domain.

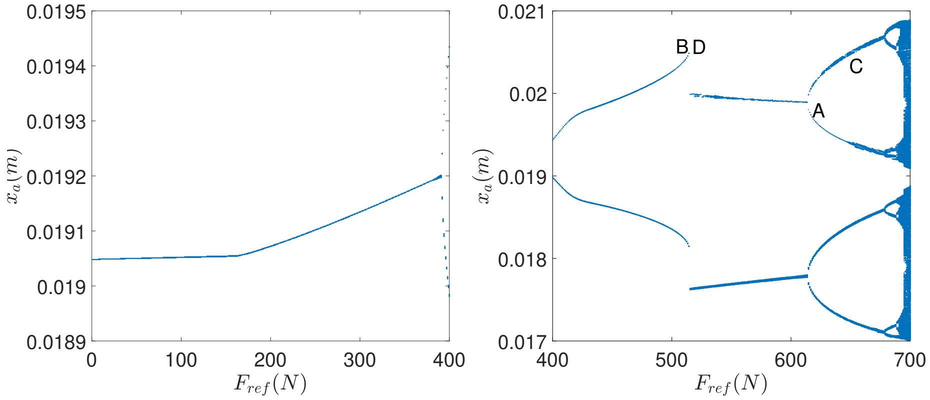

(a) $k_N = 0$ (b) $k_N = 0$

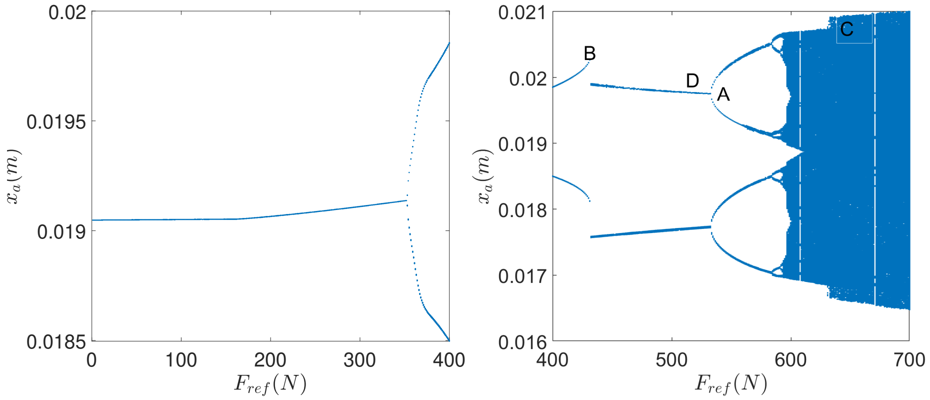

(c) k_N=2.5 × 10^6 N/m^3 (d) k_N=2.5 × 10^6 N/m^3

Figure 4.3: Bifurcation diagrams for $\omega = 47$ Hz with (i), (ii) k_N= 0, (iii) and (iv) k_N=2.5 × 10^6 N/m^3. These diagrams show points at which period doubling occurs with the change in bifurcation parameters for different values of the cubic nonlinear stiffness k_N of the absorber.

These observations suggest that the selection of the nonlinear stiffness of the NLTVA and operating frequency significantly influences both the amplitude and the onset of complex motions in the system. From the bifurcation diagrams, we further conclude that although the addition of nonlinearity can reduce the amplitude of transmitted vibrations, it may also introduce complex motions, such as period-2 and quasi-periodic solutions. Since such complex motions like quasi-periodic and period-4 solutions appear at the higher bound of the operating frequency, the rest of the analysis is performed at $\omega = 47$ Hz. In the next step, we will evaluate the effect of changing the absorbers' damping, c_N, on the system's response.

4.3.3 Parametric Study of c_N

Similar to the analysis conducted for k_N, both bifurcation diagrams and phase portraits are used to elucidate the effect of the absorber's damping on the vibrations transmitted to the hand-arm system. These bifurcation diagrams are shown in Fig. 4.7 with the hand-arm response as the variable of interest and F_{ref} as the bifurcation parameter. It is evident from Fig. 4.7 that as absorber damping increases, the excitation force value corresponding to the transition from periodic to aperiodic motions, which is denoted by point F, also increases. This observation implies that a higher damping value in the NLTVA expands the F_{ref} range where the HHIM manifests aperiodic behavior. Notably, during HHIM operations, such as with a chipping hammer, a region characterized by periodic motions (either period-1 or period-2) is generally more favorable than an aperiodic region. This can be attributed to more efficient operational metrics like higher penetration rates being achieved in the periodic region [11]. Therefore, integrating an NLTVA with higher damping values can enhance the effectiveness of HHIM operations.

A closer inspection of Fig. 4.7 further shows that an increase in absorber damping can cause an increase in the amplitude of transmitted vibration of approximately 0.1 mm. This observation suggests that lower damping values in the NLTVA can effectively mitigate vibrations

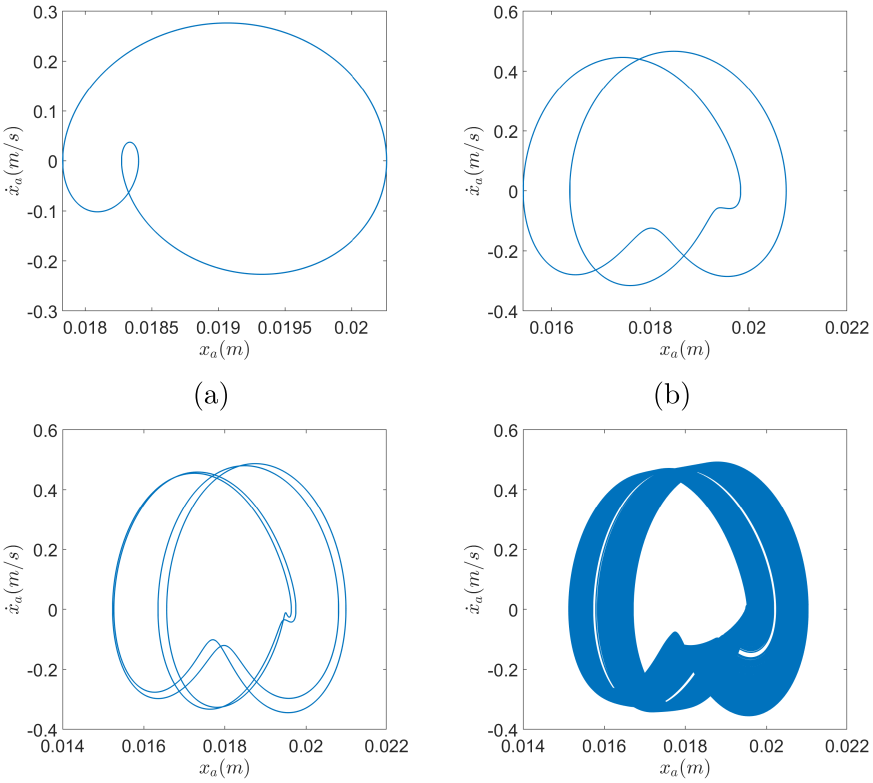

(a) (b)

(c) (d)

Figure 4.4: Phase portrait for $\omega = 47Hz$, $k_N = 0$ and $F_{ref} =$ i)500 N ii) 650 N iii) 685 N and iv) 695 N. These diagrams reveal the changing periodicity of the hand-arm response, with changing 'F_{ref}', through orbits that visualize the state space thereby allowing one to observe the periodicity of the system.

transmitted to the hand-arm system. Hence, the damping of NLTVA can enhance or deteriorate the performance of HHIM depending on the objectives, and similar to k_N, a careful selection of c_N is needed for the efficient operation of HHIM.

Phase portraits further highlighting other transitions in the dynamics of the system due to the change in the absorber's damping value are shown in Fig. 4.8 and Fig. 4.9. Subsequently, we will evaluate the impact of the feed force on absorber performance.

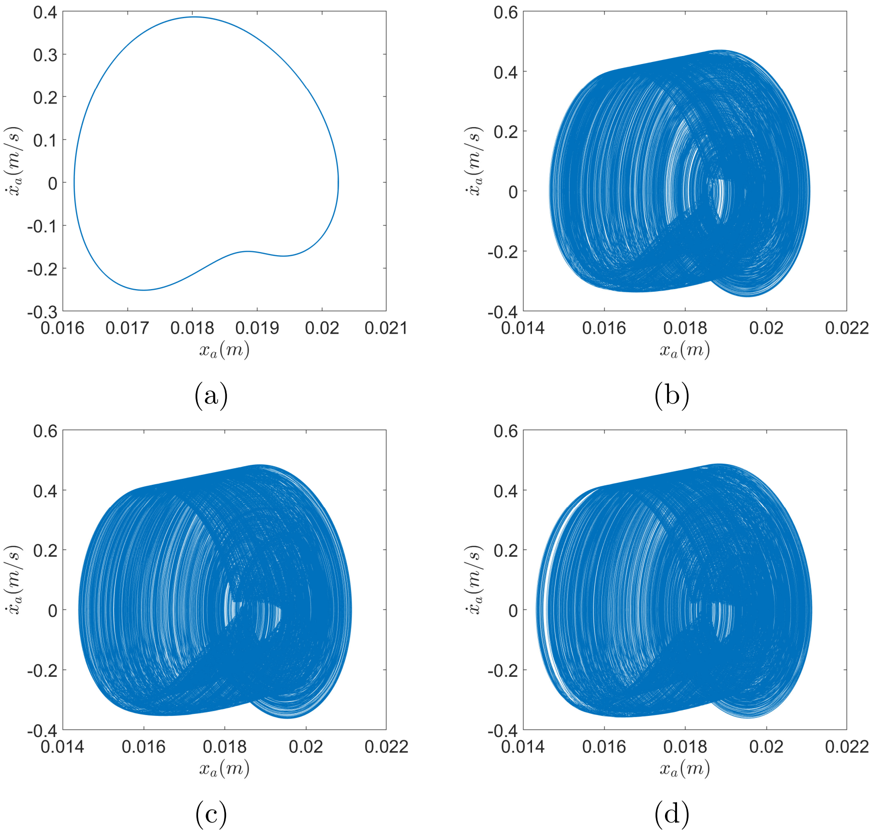

(a) (b) (c) (d)

Figure 4.5: Phase portrait for $\omega = 47$ Hz, $k_N = 2.5 \times 10^6$ N/m^3 and F_{ref}= a) 500N b) 650 N c) 685 N and d) 695 N. These portraits show the state of the system at different bifurcation parameters,F_{ref}

4.3.4 Effect of Feed Force (F_{feed}) on Absorber Performance

It should be noted that Dong *et al.* [100] observed that the feed force applied to an HHIM significantly influences the vibrations transmitted by the tool. Therefore, having established the effects of the absorber parameters k_N and c_N, it is essential to investigate the impact of feed force on the response of the hand-arm system in HHIM applications.

To explore the effect of feed force on absorber performance, we employ bifurcation plots and phase portraits, considering two different values of k_N. The results are illustrated in Figs. 4.4 and 4.11. From Fig. 4.4, it can be observed that higher values of feed force lead to periodic motions for both considered values of k_N. As F_{feed} decreases, the system transitions

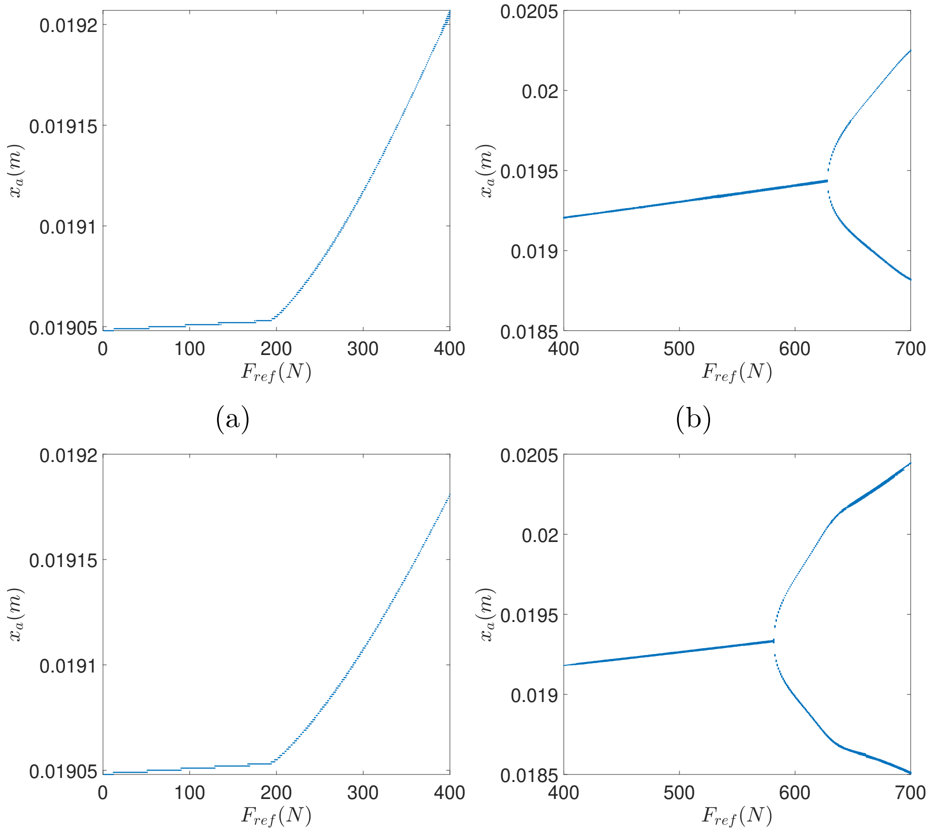

(a) (b)

(c) (d)

Figure 4.6: Bifurcation diagrams for ω = 43 Hz with (i), (ii) k_N= 0, and (iii), (iv) k_N=2.5×10^6 N/m^3. These diagrams shows the change in bifurcation parameters at which period-doubling occurs when the cubic nonlinear stiffness k_N of the absorber is changed. Varying k_N also reveals changes in the amplitude of the hand arm at various bifurcation points.

from periodic to high-amplitude aperiodic motions via period-doubling bifurcation. The corresponding phase portraits are shown in Fig 4.11. The introduction of nonlinearity in the absorber (i.e., nonzero values of k_N) elevates the threshold value of F_{feed} for period-doubling bifurcation but concurrently reduces the amplitude of vibrations transmitted to the human hand at higher feed forces. For example, at $F_{\text{feed}} = 260\,\text{N}$, the inclusion of nonlinearity in the absorber reduces the vibration amplitude by 0.1 mm.

These observations further imply the need for a careful selection of the absorber parameters

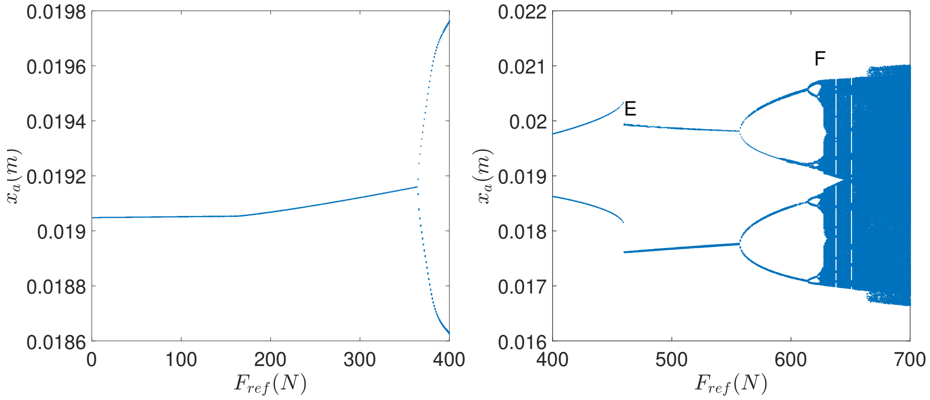

(a) $c_N = 18.6$ N-s/m (b) $c_N = 18.6$ N-s/m

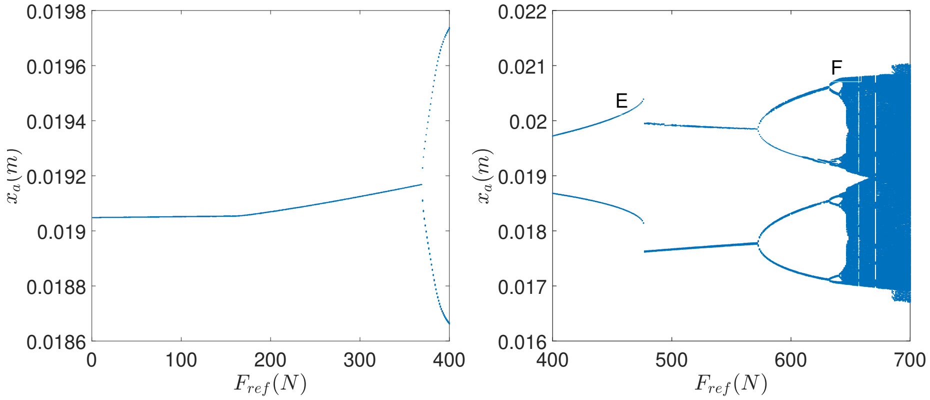

(c) $c_N = 27.9$ N-s/m (d) $c_N = 27.9$ N-s/m

Figure 4.7: Comparison of bifurcation diagram for different values of c_N and with $\omega = 43Hz$. (i) and (ii) $c_N = 18.6$ N-s/m, (iii) and (iv) $c_N = 27.9$ N-s/m. These diagrams show the periodic and aperiodic motions that emerge as a result of varying the damping of the absorber.

depending on the feed force being applied to the system.

4.4 Discussion

The results from our comprehensive parametric study indicate that the performance of the proposed NLTVA in the HHIM depends on the specific forcing range in which the vibro-impact system, such as the HHIM, operates. As mentioned earlier, in the context of per-

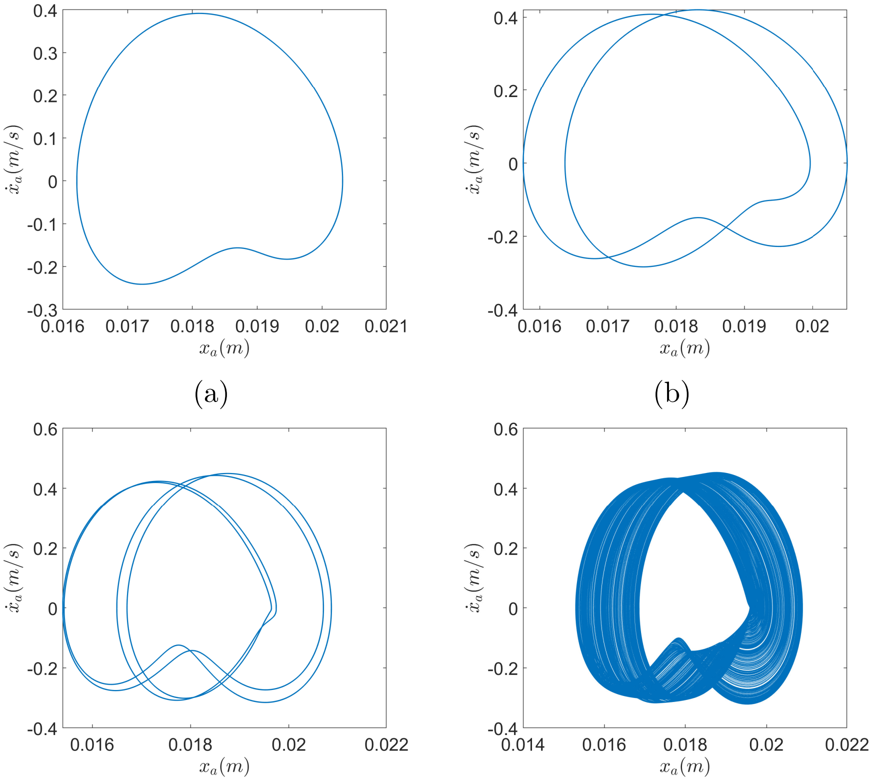

(a) (b)

(c) (d)

Figure 4.8: Phase portrait for $\omega = 47Hz$, c_N= 18.6 $\frac{Ns}{m}$ and $F_{ref} = a)\,500N$ b) $570N$ c) $620N$ and d) $630N$. These portraits present a visual description of the changing state of the system at different bifurcation parameters, F_{ref}.

cussive tools like the chipping hammer, optimal operation is achieved in a periodic regime. Hence, the parameters of NLTVA should be calibrated according to the forcing conditions inherent to the HHIM to provide periodic solutions. Our findings confirm that the NLTVA is particularly effective in mitigating hand-transmitted vibrations in this state.

Our research further unveils the significant influence of feed force and excitation frequency on the system's dynamics. Specifically, variations in the feed force (from high to low values) were found to induce a transition from periodic to aperiodic motion in the system, accompanied by amplification of vibrations transmitted to the hand. Moreover, the damping capabilities of the NLTVA were observed to be sensitive to changes in feed force, necessitating the need for

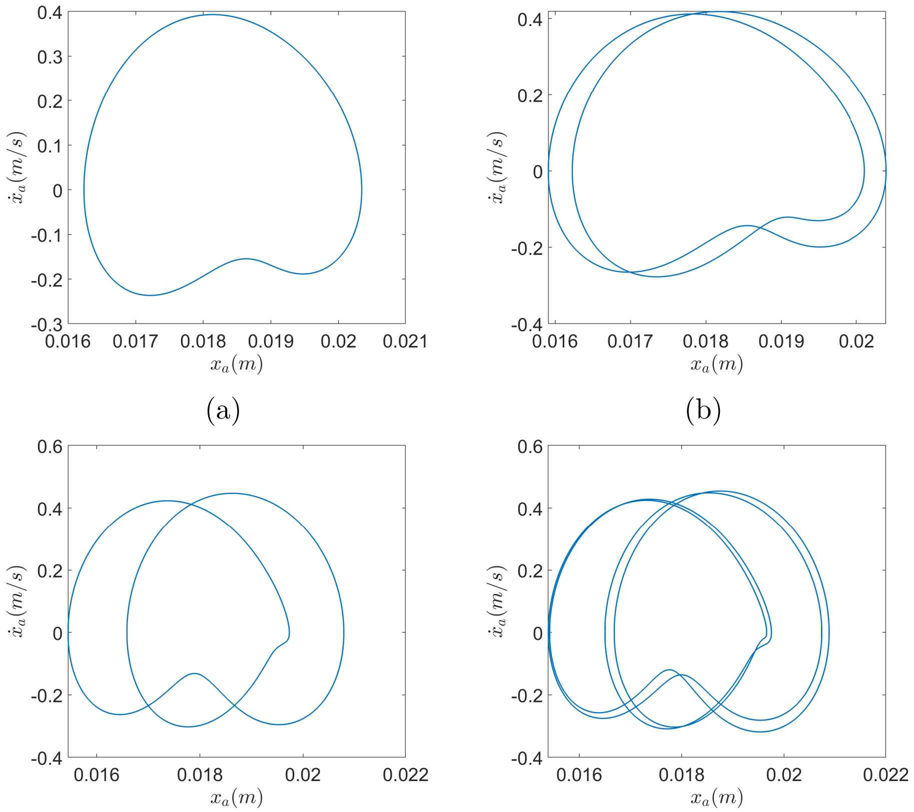

(a) (b)

(c) (d)

Figure 4.9: Phase portrait for $\omega = 47Hz$, c_N= 27.9 $\frac{Ns}{m}$ and $F_{ref} = a)500N$ b)$570N$ c)$620N$ and d)$630N$.These portraits present a visual description of the changing periodicity of the system at different bifurcation parameters, F_{ref}.

adaptive design strategies in the absorber to accommodate varying operational conditions.

These observations show that the parameters of the NLTVA would need to be appropriately tuned based on the working feed force for the HHIM being used.

4.5 Conclusion

We investigated the efficacy of a nonlinear tuned vibration absorber (NLTVA) in mitigating the vibrations transmitted to the hand-arm system from hand-held power tools, specifically

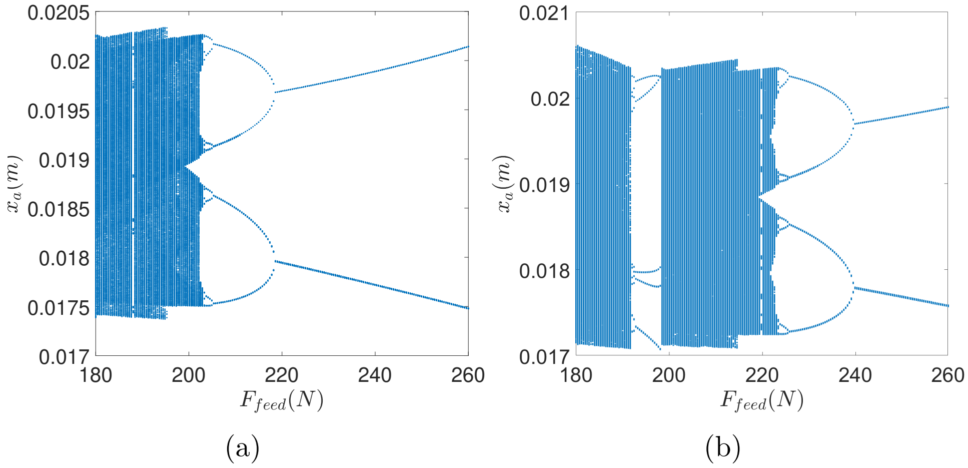

(a) (b)

Figure 4.10: Bifurcation diagram with F_{feed} as bifurcation parameter with (i) k_N= 0, and (ii) k_N=2.5 × 10^6 N/m^3. These diagrams show the periodic and aperiodic motions that disappear and emerge as a result of varying the feed-force applied to the tool model.

focusing on a chipping hammer. The chipping hammer was modeled using a vibro-impact framework to emulate realistic operating conditions. A thorough parametric analysis through bifurcation analysis was conducted to study the absorber's effectiveness. Key parameters such as the absorber's stiffness, damping, and applied feed force were examined in detail. Our analysis revealed that the NLTVA could either attenuate or amplify hand-transmitted vibrations, depending upon the excitation forcing range of the hand-held impact machine (HHIM). Undesired amplification was observed during transitions from periodic to aperiodic motion regimes. Notably, the absorber reduced hand-transmitted vibrations when the HHIM operated efficiently within a periodic regime. Moreover, we observed that changes in feed force or excitation frequency necessitate a recalibration of the absorber parameters for optimal performance. These findings validate the potential of a nonlinear cubic absorber as a robust vibration control solution for HHIM applications. These findings also highlight the need for future studies entailing parameter optimization to ensure consistent absorber effectiveness across varying HHIM operating conditions. Furthermore, this study introduces a nonlinear dynamic framework for assessing the effectiveness of a cubic absorber in a non-

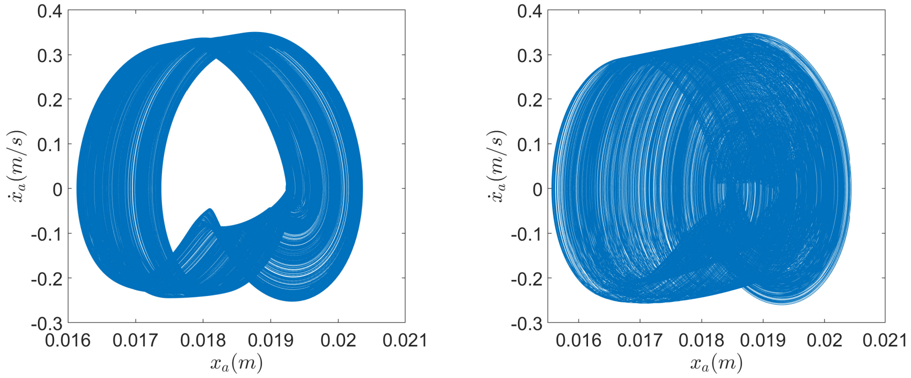

(a) (b)

Figure 4.11: Comparison of Phase portraits for $F_{feed} = 200N$ and different values of k_N. Phase portrait for $\omega = 47Hz$, $F_{ref} = 500N$ and k_N= a)$0N/m$ and b)2.5 $\times 10^6 N/m$.These portraits present a visual description of the change in state of the system at different bifurcation parameters, F_{ref}.

smooth system, facilitating experimental evaluation

Chapter 5

Impact of Grazing on the Experimentally Validated Vibro-Impact Model Coupled to a Cubic Absorber

This chapter was collaboratively developed by the following authors: **Ore Alabi**, **Dr. Sunit Kumar Gupta**, and **Dr. Oumar Barry**. The contributions, categorized according to the *CRediT (Contributor Roles Taxonomy)*, are as follows:

- **Conceptualization**: Ore Alabi, with guidance from Dr. Oumar Barry.
- **Methodology**: Ore Alabi, with feedback from Dr. Oumar Barry.
- **Formal Analysis**: Ore Alabi.
- **Investigation**: Ore Alabi.
- **Writing – Original Draft**: Ore Alabi.
- **Writing – Review & Editing**: Dr. Oumar Barry and Dr. Sunit Kumar Gupta.
- **Supervision**: Dr. Oumar Barry.

This chapter is edited from:

Alabi, O., Gupta, S. K., and Barry, O. (2025, August). Analytical Exploration of the Nonlinear Dynamics of a Hand-Arm System Coupled with a Tool Exhibiting Non-Smooth Ground Interaction. Paper presented at the International Design Engineering Technical Conferences and Computers and Information in Engineering Conference, Anaheim, California, USA. [Manuscript in preparation for ASME proceedings].

Introduction

Various studies have highlighted the impact of severe vibration exposure on the hand-arm system [27, 39]. Prolonged use of hand-held tools can lead to hand-arm vibration syndrome (HAVS), a disorder characterized by vascular, musculoskeletal, and neurological complications [28–31]. One of the primary symptoms of HAVS is vibration white finger (VWF), which can progress to permanent disability in extreme cases [32–35]. To assess the risk posed by vibration exposure to the hand, this study focuses on a key contributing factor—vibration intensity, as measured by acceleration—by analyzing the nonlinear dynamics that govern the operation of a hand-held impact tool. Understanding the mechanisms through which vibrations are transmitted to the hand is the central aim of this paper. A deeper understanding of these dynamics provides a foundation for selecting appropriate vibration control strategies, thereby reducing the risk of long-term adverse health effects among hand-tool users.

Towards addressing the problem of how vibrations are propagated to the hand, various models have been proposed to accurately capture the tool-hand dynamics. These models aim to assess the transmission of vibrations from the tool to the hand and include lumped parameter linear models as well as models incorporating cubic and piecewise nonlinearities [6–9]. Such nonlinearities are typically introduced through the dynamics of the tool itself. It has been shown that models with piecewise-smooth nonlinearities more effectively capture the physics of repetitive impacts or discontinuous contact events that occur during tool operation [10–12, 14–18]. For instance, in the modeling of rotary oil drilling systems, the combined effects of cutting and frictional interactions between the bit and rock were captured using a nonsmooth model based on Stribeck friction [108]. In efforts to optimize the rate of drilling progression, Pavlovskaia *et al.* showed that nonsmooth models could best predict the static and dynamic forces that produced the most efficient vibroimpact drilling performance [11]. Similarly, to represent the nonlinear interaction between the bit and rock, Liao *et al.* compared linear and nonlinear models capturing loading and unloading force-penetration dynamics and found that both, while piecewise-smooth, could accurately model the dynamics at low excitation frequencies and small amplitudes [109]. Wiercigroch *et al.* also used a piecewise system to predict the material removal rate of an ultrasonic drill under varying static loads [104]. Given the demonstrated ability of lumped parameter models with nonsmooth or vibroimpact dynamics to capture essential features of percussive tools, this work adopts the approach of Alabi *et al.* [110] to investigate how vibrations are transmitted to the hand by modeling the tool as a vibroimpact system. To fully analyze such a system, it is critical to understand the conditions under which the system transitions between different states, and what qualitative behavior emerges during and after those transitions. In particular, we are interested in understanding how these dynamics influence the magnitude of acceleration transmitted to the hand. To this end, we examine grazing phenomena—a hallmark of nonsmooth systems with impacts such as the one considered here [111–114].

Grazing is defined as a phenomenon that occurs when a mass just makes tangential contact with an impact surface. It has been widely recognized that grazing in nonsmooth systems can induce abrupt transitions in the underlying dynamics. These transitions may include the appearance or disappearance of multistable attractors, loss of stability, onset of chaotic behavior, and emergence of vulnerable attractors [60, 63, 66, 115, 116]. Analyzing the post-grazing dynamics is essential, as these changes in steady-state behavior would not arise in the absence of the discontinuities that characterize nonsmooth systems. For instance, in atomic force microscopy, grazing transitions have been linked to the sudden termination of periodic solution branches due to hysteretic force interactions [117]. Moreover, metrology errors have been attributed to the transition from periodic to chaotic responses when microcantilever tips experience grazing in dynamic atomic force microscopy [118]. In the analysis of impact oscillators, grazing has been shown to cause the disappearance of stable periodic motion [64]. Similarly, in an aeroelastic system modeled as a nonsmooth dynamical system, the occurrence of grazing bifurcations was found to induce abrupt jumps in system response [59]. Given the dramatic transitions that grazing can trigger in system behavior, it is imperative to study nonsmooth systems exhibiting grazing using analysis methods that allow these events to be accurately tracked. To this end, we now turn our attention to a review of methods previously used to analyze the dynamics of nonsmooth systems.

Several techniques have been developed to analyze nonsmooth systems, including numerical integration methods and path-following continuation approaches. One of the more common strategies involves smoothing the nonsmooth differential equations, which enables the use of standard numerical tools such as numerical bifurcation analysis. In such formulations, the state space is partitioned into subspaces, each governed by a smooth ordinary differential equation [105, 119]. This technique was used by Savi *et al.* to validate experimentally observed chaos and period-doubling behavior in a nonsmooth system with a discontinuous support [120]. Similarly, smoothed approximations have been employed to study the stability of a single-degree-of-freedom system with a piecewise-linear force–displacement relationship under harmonic excitation [121]. Another powerful method for analyzing nonsmooth dynamics is path-following continuation, which allows for tracking critical behaviors such as bifurcations and limit cycles in parameter space. For example, Zhang *et al.* used the continuation toolbox COCO to compute grazing periodic orbits in a hybrid dynamical system and investigated the effectiveness of time-delayed feedback control in suppressing undesirable dynamics near grazing [122]. Chavez *et al.* also used COCO to track controller parameters that influence the occurrence of grazing in a forced impact oscillator [123].

In this work, due to the hybrid nature of the nonsmooth tool model under investigation, we begin with direct numerical integration of a smoothed set of ODEs using MATLAB's `ODE45` solver. To ensure the numerical solution is set up correctly, we perform an energy balance analysis to verify consistency between input work and system energy dissipation. We then employ COCO to track grazing periodic orbits that arise in the system. A novel contribution of this work lies in exploring whether grazing affects the acceleration transmitted to the hand, and in conducting a parametric study to examine how key variables—such as feed force—influence the onset of grazing in the system. While continuation techniques have been used to analyze grazing in various mechanical and control systems [122, 123], previous studies have not applied such methods to models that include both the vibroimpact dynamics of percussive tools and their coupling to a human hand-arm system. This work is the first to leverage the COCO continuation framework to systematically detect and track grazing bifurcations in a nonsmooth hybrid model of a tool-hand interface. Furthermore, because the vibro-impact model has been validated against experimental findings, we now reevaluate the absorber's effectiveness within this framework, extending the analysis previously conducted in Chapter 4.

To carry out this study, a lumped parameter model adapted from the work of Alabi *et al.* is employed to represent the percussive tool as a two-degree-of-freedom (2-DOF) vibro-impact system, while the hand-arm system is modeled as a separate 2-DOF lumped parameter system [110]. The resulting nonsmooth hybrid system is smoothened using Filippov's method, enabling both qualitative analysis via numerical bifurcation techniques and hybrid orbit continuation using the COCO toolbox.

The remainder of the paper is organized as follows. Section 5.1 presents the mathematical model of the vibro-impact HAS–HHIM system, outlines the smoothing procedure applied to the nonsmooth dynamics, and describes the continuation scheme used to track grazing orbits. Section 5.2 presents the major findings of the study, followed by a discussion of their implications in Section 5.3. Finally, conclusions are summarized in Section 5.3.

5.1 Model Development of HHIM–HAS–NVAI System

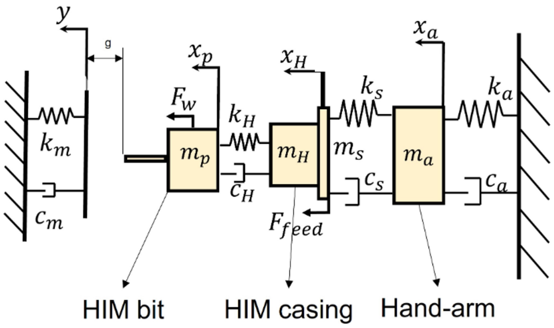

Figure 5.1: Schematic of the combined system of HHIM-HAS system

In this section, we present the reduced-order vibro-impact model of the coupled HAS-HHIM system adapted from [110]. The schematic of the system is shown in Fig.5.1. In the schematic, the bit of the HHIM is modeled as a lumped mass, m_p, whereas the housing of the HHIM is modeled as a lumped mass m_H. The buffer between the HHIM bit and casing is modeled as a visco-elastic connection with parameters k_H and c_H. In this model, we also account for the feed force to press the machine against the material being worked on.

To capture the HHIM dynamics associated with the percussive action of the HHIM piston on the HHIM bit, a nonlinear interaction is specified between the HHIM bit and the ground material. To do so, the ground material is modeled as a linear spring–damper as presented in[79, 103, 104] with the initial separation of g from the HHIM bit. In this model, the ground material is restored before each successive impact, and the process of penetration of material is not taken into consideration. In this work, we consider concrete as the ground material with the stiffness and loss factors adopted from [79].

It is acknowledged that the present model may not capture all aspects of the physical dynamics due to the absence of advanced tool-tip representations such as viscoelastic connections with drift. Drift mechanisms can represent the net penetration of the tool bit into the material over time—an effect not accounted for in this formulation. Future studies could incorporate such features to examine whether the inclusion of drift provides additional insight beyond that offered by the simple viscoelastic contact model employed here.

Similarly, the hand-arm system is modeled as a 2-DOF lumped parameter system, which has been shown to provide an accurate representation of hand-transmitted vibrations at frequencies below 100 Hz [41]. As the operating frequency of the system in this study is approximately 45 Hz, the 2-DOF model is deemed sufficient for capturing the relevant dynamic response.

5.1.1 Non-Smooth Model

As similarly performed by Alabi *et al.* [110], the nonsmooth system is smoothened via the procedure below. In the schematic, x_H, x_a, x_p, and y represent the motion of the HHIM casing, HAS, HHIM bit, and massless support, respectively.

Due to the discontinuous nature of the HAS-HHIM system, the governing equations of motion are defined by two sets of differential equations: one for the contact phase and another for the non-contact phase. Defining f_m as the contact force between m_p and the material, the transition logic is given by:

$$\begin{cases} x_p < g, \quad f_m = 0 \quad : \text{without contact}, \\ x_p \geq g, \quad f_m = -\left(k_m y + c_m \dot{y}\right) < 0 \quad : \text{with contact}. \end{cases} \tag{5.1}$$

Following Leine [105], we assume that the support relaxes rapidly between contact events, and thus its free motion is neglected. The resulting governing equations of motion become:

$$\begin{aligned} (m_H + m_s)\ddot{x}_H = {} & \dot{x}_a c_s + x_a k_s + \dot{x}_p c_H + x_p k_H \\ & - \dot{x}_H(c_H + c_s) - x_H(k_H + k_s) + F_{feed}, \end{aligned} \tag{5.2a}$$

$$m_a\ddot{x}_a = -\dot{x}_a(c_a + c_s) - x_a(k_a + k_s) + \dot{x}_H c_s + x_H k_s, \tag{5.2b}$$

$$m_p\ddot{x}_p = \begin{cases} -\dot{x}_p(c_H + c_m) - (x_p - g)k_m - x_p k_H \\ \qquad +\dot{x}_H c_H + x_H k_H + F_w, \quad \text{with contact}, \\ -\dot{x}_p c_H - x_p k_H + \dot{x}_H c_H + x_H k_H + F_w, \quad \text{without contact}. \end{cases} \tag{5.2c}$$

Here, F_{feed} is the operator-applied feed force and F_w is the piston-induced excitation, defined as:

$$F_w = F_{ref}\left(\frac{\omega}{\omega_{ref}}\right)^2 \sin(\omega t). \tag{5.3}$$

To simulate the nonsmooth dynamics, the system is convexified using Filippov's theory [106].

The state space is split into:

$$\begin{aligned}\mathcal{V}_- &= \{\boldsymbol{x} \in \mathbb{R}^n \mid h(\boldsymbol{x}) < 0\},\\ \Sigma &= \{\boldsymbol{x} \in \mathbb{R}^n \mid h(\boldsymbol{x}) = 0\},\\ \mathcal{V}_+ &= \{\boldsymbol{x} \in \mathbb{R}^n \mid h(\boldsymbol{x}) > 0\}.\end{aligned}$$

The resulting inclusion is:

$$\dot{\boldsymbol{x}}(t) \in \boldsymbol{F}(t, \boldsymbol{x}) = \begin{cases} \boldsymbol{f}_-, & \boldsymbol{x} \in \mathcal{V}_-, \\ \overline{\text{co}}\{\boldsymbol{f}_-, \boldsymbol{f}_+\}, & \boldsymbol{x} \in \Sigma, \\ \boldsymbol{f}_+, & \boldsymbol{x} \in \mathcal{V}_+, \end{cases} \tag{5.4}$$

where the convex combination is:

$$\overline{\text{co}}\left\{\boldsymbol{f}_-, \boldsymbol{f}_+\right\} = \{(1-q)\boldsymbol{f}_- + q\boldsymbol{f}_+,\, q \in [0,1]\}.$$

Switching boundaries are defined by:

$$h_\alpha(x_p, \dot{x}_p) = x_p - g, \tag{5.5}$$

$$h_\beta(x_p, \dot{x}_p) = k_m(x_p - g) + c_m \dot{x}_p. \tag{5.6}$$

The transitions are:

$$\begin{aligned}
\mathcal{V}_- &= \{\boldsymbol{x} \mid h_\alpha < 0 \text{ or } h_\beta < 0\},\\
\mathcal{V}_+ &= \{\boldsymbol{x} \mid h_\alpha > 0 \text{ and } h_\beta > 0\},\\
\Sigma_\alpha &= \{\boldsymbol{x} \mid h_\alpha = 0,\, h_\beta \geq 0\},\\
\Sigma_\beta &= \{\boldsymbol{x} \mid h_\beta = 0,\, h_\alpha \geq 0\}.
\end{aligned}$$

5.1.2 Continuation Segments for COCO

To facilitate the detection and tracking of grazing in the hybrid nonsmooth system using COCO, a periodic orbit is constructed by partitioning the trajectory into two segments, denoted by I_1 and I_2, each governed by a distinct vector field and transition logic. These segments represent two phases of the system's hybrid dynamics.

The angle variable θ is defined as $\theta = \omega t$, where ω is the angular frequency appearing in the excitation term:

$$F_w = F_{ref} \left(\frac{\omega}{\omega_{ref}}\right)^2 \sin(\omega t). \tag{5.7}$$

The transition between segments is implemented using COCO's multi-segment continuation structure. The following defines the event and reset functions used in each segment:

- **Segment I_1: No-Contact Dynamics with Phase-Based Reset**

$$\begin{aligned}
\text{Event function:} \quad & h_1(\boldsymbol{x}) = \pi - \theta = \pi - \omega t,\\
\text{Reset map:} \quad & \boldsymbol{x}^+ = \Big[x_H,\, \dot{x}_H,\, x_a,\, \dot{x}_a,\, x_p,\, \dot{x}_p,\, \theta - 2\pi\Big]^\top .
\end{aligned}$$

This phase reset ensures continuity in the periodic orbit by wrapping the angular phase variable θ.

- **Segment I_2: No-Contact Dynamics with Impact Reset**

$$\begin{aligned} \text{Event function:} \quad & h_2(\boldsymbol{x}) = x_p - g, \\ \text{Reset map:} \quad & \boldsymbol{x}^+ = \boldsymbol{x}. \end{aligned}$$

This reset corresponds to the event of bit contact with the ground. The reset is the identity map, as no discrete jump in the event of grazing.

For direct numerical integration, the differential equation is integrated using the smoothing switch model introduced by Leine [107], with smoothing thickness 2η applied around the switching surface. While for the continuation of the solutions of the system, the *hspo* toolbox COCO is used [124].

Table 5.1: Parameter values of the HHIM-HAS-NLTVA system used for simulations.

Parameter	Value	Unit	Parameter	Value	Unit	Parameter	Value	Unit
m_H	8	kg	k_H	4×10^6	N/m	c_H	500	Ns/m
m_a	1.55	kg	k_a	4279	N/m	c_a	76	Ns/m
m_s	0.049	kg	k_s	62804	N/m	c_s	193	Ns/m
F_{ref}	80	N	ω_{ref}	30	Hz	g	0.02	m
m_p	0.35	kg	F_{feed}	40	N	k_m	3×10^6	N/m
c_m	50	Ns/m	c_N	9.3×10^5	Ns/m	k_{NL}	2.0×10^1	N/m
m_N	$0.8\, m_H$	kg	k_N	2.5	N/m^3	–	–	–

5.2 Results

In this section, we begin by validating the chipping hammer model using its frequency response characteristics. Specifically, system parameters are tuned so that the model reproduces natural frequency peaks observed experimentally in the hand acceleration frequency response function (FRF). To further ensure that the numerical formulation is set up correctly, we perform an energy balance analysis to verify consistency between input work and dissipated energy in the validated model.

Following this verification, we use bifurcation diagrams to identify the presence of grazing phenomena in the system. A two-parameter continuation study is then performed using COCO to examine how variations in operating parameters—namely the excitation amplitude F_{ref} and frequency ω—influence the onset of grazing. Finally, we conduct a parametric study to investigate how changes in the tool's feed force affect the emergence and progression of grazing bifurcations. We also investigate the behavior of the hand-arm in different grazing regimes.

5.2.1 Validation of Chipping Hammer Dynamics

The validation of the chipping hammer model is done by tuning the system parameters so that the resulting hand-arm acceleration frequency response function (FRF), obtained via bifurcation diagrams, exhibits certain natural frequency peaks. These peaks are selected to match those observed experimentally in the FRF of a chipping hammer measured at the tool handle. Validation based on natural frequencies is essential, as it ensures the model accurately captures the frequencies at which vibration intensity at the hand is amplified. Experimental studies have shown that the hand acceleration FRF of a chipping hammer typically exhibits distinct peaks near the dominant operating frequency of the tool [100] and near the natural frequency of the chipping hammer handle [125]. Accordingly, the model parameters presented in Table 5.1 are selected so that the tool exhibits dominant frequency peaks near 45 Hz—corresponding to the tool's operating frequency—and around 600 Hz, which aligns with the resonance of the hammer handle. The resulting hand acceleration

FRF, showing these characteristic peaks, is obtained using MATLAB's `ode45` solver with tight relative and absolute tolerances (10^{-11}) to integrate the system's first-order ODEs. The excitation frequency was swept across a defined range, and for each value, the system was numerically evolved to steady-state through repeated simulations. From the steady-state response, the *peak hand-arm acceleration* was extracted and plotted against frequency to capture the system's resonance behavior and validate the dynamic model as shown in Fig. 5.2.

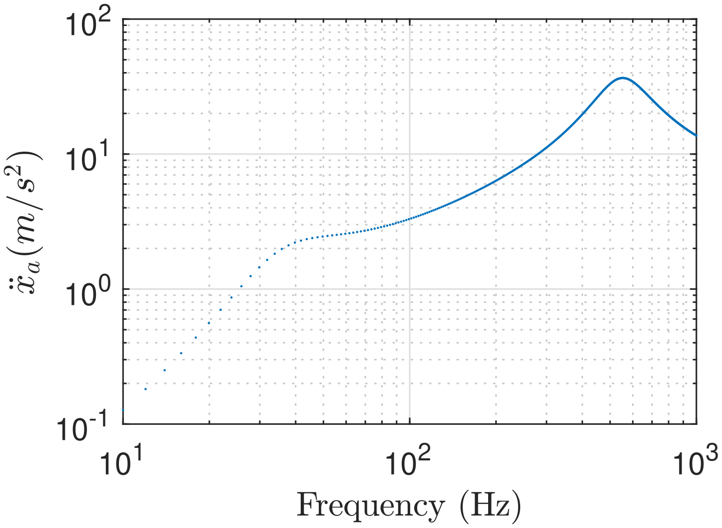

(a)

Figure 5.2: Frequency response function (FRF) of hand acceleration $\ddot{x}_a$ versus excitation frequency, showing resonance peaks at approximately 45 Hz and 600 Hz. These peaks correspond to the natural frequencies of the modeled system and reflect trends typical of the chipping hammer handle experimental vibration data.

5.2.2 Energy Balance Analysis

To verify that the numerical method employed was sufficient to simulate the dynamics of the system, we employed the instantaneous energy balance in order to verify that the rate of change of total stored energy (kinetic plus potential) equals the net mechanical power supplied to the system. The stored energy terms are obtained by differentiating the kinetic and potential energies of each generalized coordinate with respect to time.

The input power consists of two contributions: (i) the feed force acting at the handle, and (ii) the harmonic excitation force acting at the percussive mass. Dissipation arises from viscous damping at each coupling, along with ground damping when contact occurs. The potential energy terms account for linear and nonlinear springs, as well as ground compliance when in contact.

As the full HIM system appended with an absorber will also be evaluated in this work, the energy balance was implemented for the system shown in Fig.4.1 and with parameters defined in table 5.1. In addition, an ω value of 206.7Hz was used. The expressions for the energy balance are as shown below:

Time Derivative of Kinetic Energy:

$$\frac{dT}{dt} = (m_H + m_s)\,\dot{x}_H\,\ddot{x}_H + m_a\,\dot{x}_a\,\ddot{x}_a + m_N\,\dot{x}_N\,\ddot{x}_N + m_p\,\dot{x}_p\,\ddot{x}_p$$

Time Derivative of Potential Energy:

$$\begin{aligned}\frac{dV}{dt} &= k_a\,x_a\,\dot{x}_a + k_s\,(x_H - x_a)(\dot{x}_H - \dot{x}_a)\\ &\quad + k_H\,(x_p - x_H)(\dot{x}_p - \dot{x}_H) + k_{NL}\,(x_N - x_H)(\dot{x}_N - \dot{x}_H)\\ &\quad + k_N\,(x_N - x_H)^3(\dot{x}_N - \dot{x}_H) + \chi(x_p)\,k_m\,(x_p - g)\,\dot{x}_p\end{aligned}$$

with the contact indicator

$$\chi(x_p) = \begin{cases} 1, & x_p \geq g, \\ 0, & x_p < g. \end{cases}$$

Dissipated Power:

$$P_{\text{diss}} \;=\; c_a\,\dot{x}_a^2 + c_s\,(\dot{x}_H - \dot{x}_a)^2 + c_H\,(\dot{x}_p - \dot{x}_H)^2 + c_N\,(\dot{x}_N - \dot{x}_H)^2 + \chi(x_p)\,c_m\,\dot{x}_p^2$$

External Input Power:

$$P_{\text{ext}} \;=\; F_{\text{feed}}\,\dot{x}_H + F_w\,\dot{x}_p,$$

Instantaneous Energy Balance Residual:

$$\text{resid} \;=\; P_{\text{ext}} - \left(\frac{dT}{dt} + \frac{dV}{dt} + P_{\text{diss}}\right)$$

With a properly implemented numerical scheme, the residual of the energy balance should approach zero, up to the error tolerance of the numerical solver. As observed in Fig 5.3. d, the residual remains on the order of 10^{-11}, which matches the solver tolerance and confirms consistency of the energy balance.

5.2.3 Grazing Detection and Orbit Initialization for Continuation

Having selected the system parameters and ensured the accuracy of the numerical scheme, the excitation amplitude of the chipping hammer is varied to generate a frequency response function (FRF) that exhibits grazing behavior. This FRF is constructed by plotting the amplitude of the tool tip in order to identify the points where the tool tip grazes the ground, defined at $\mathrm{x}_p = \mathrm{g} = 0.02 \quad \mathrm{m}$. As shown in Fig. 5.5a, the system exhibits grazing at two distinct points, labeled G_1 and G_2.

To investigate how the system's grazing behavior evolves, we construct an initial solution guess in the form of a periodic orbit corresponding to the grazing point G_2. The resulting orbit is shown in the phase portrait in Fig. 5.5b. This trajectory consists of two segments, $\mathcal{I}_1$ and $\mathcal{I}_2$, corresponding to distinct phases of the hybrid system dynamics, as previously described. The orbit is obtained via direct numerical integration of the smooth vector fields, with event and reset conditions applied at each segment boundary. This trajectory serves as the initial guess for hybrid orbit continuation in COCO.

To enable grazing continuation, a grazing event constraint is appended to the problem. Specifically, grazing is detected when the tool tip reaches the ground with zero normal velocity. This is enforced by monitoring the impact condition $h(\boldsymbol{x}) = x_p - g = 0$ along with the tangency condition $\dot{x}_p = 0$ at the point of contact. A pairwise parameter continuation is then carried out, allowing the chipping hammer's operating parameters to vary while constraining the orbit to remain at the grazing condition.

The resulting continuation curve in the chipping hammer's operating parameter space (ω, F_{ref}) is shown in Fig. 5.6. The continuation begins at the grazing point labeled G_1 and identifies a second grazing point G_2, as previously shown in Fig. 5.5a. The study reveals that for lower values of F_{ref}, the system does not exhibit grazing (labeled region A in the diagram). However, at higher values of F_{ref}, two distinct grazing points emerge (labeled region B). As the excitation amplitude is further increased, one of these grazing points disappears, indicating a boundary in the grazing region (labeled region C). To explore how the system dynamics vary with model parameters, we perform a parametric study by varying the feed force (F_{feed}). This enables us to evaluate the resulting changes in the grazing curve within the (ω, F_{ref}) space, as well as the corresponding effect on the hand-arm system response.

5.2.4 Effect of Feed Force on Grazing Behavior

From Fig. 5.6b, we observe that an increase in F_{feed} leads to a decrease in the excitation amplitude at which grazing first occurs in the system; that is, Region A in Fig. 5.6a becomes wider. The study also reveals that with increasing feed force, the range of frequency values ω at which grazing occurs becomes more spread out. This behavior can be observed by comparing the grazing curves for $F_{\text{feed}} = 20$ N and $F_{\text{feed}} = 40$ N at $F_{\text{ref}} = 85$ N, where the lower and upper bounds of grazing shift apart — the lower grazing frequency decreases while the upper one increases as feed force increases. In addition to this widening of the grazing frequency interval, we also observe a transition in the number of grazing points. At $F_{\text{ref}} = 80$ N for $F_{\text{feed}} = 40$ N, grazing occurs at two distinct frequencies, whereas at $F_{\text{feed}} = 60$ N , only one grazing point is observed.

Based on these observations, it can be concluded that feed force affects both the onset and nature of grazing in the system. Variations in feed force shift the excitation amplitude at which grazing begins and alter the frequency values at which grazing occurs for a given excitation amplitude level. Additionally, feed force influences the number of grazing points observed. In some cases, the system transitions from exhibiting two grazing points to just one as feed force increases.

5.2.5 Effect of Grazing Regimes on Hand–Arm Acceleration Frequency Response

To assess how different grazing regimes influence vibrations at the hand-arm interface, we present acceleration frequency response functions (FRFs) at the hand. As shown in Fig. 5.7, three FRFs are obtained by keeping the feed force constant while varying the excitation force amplitude F_{ref} to position the system in grazing regimes A, B, and C, as defined in Fig. 5.6.

Initial observations indicate that as the excitation amplitude increases—from Region A (no grazing) to Region C (single grazing)—the overall amplitude of the hand-arm acceleration increases accordingly. A closer examination of Fig. 5.7 reveals that at both $\omega = 550$ Hz and the system's operating frequency of 45 Hz, a transition from Region A to B results in a 150% increase in acceleration at the hand, while the transition from Region B to C yields a 20% increase. However, the presence or absence of grazing does not appear to significantly affect the damping ratio or shift the natural frequencies observed in the FRF.

Although the current study, as shown through the FRF in Fig. 5.7, does not explicitly observe bifurcations or chaotic dynamics within Regions B or C with the onset of grazing, it is important to recognize that grazing events often act as precursors to qualitative transitions in nonsmooth systems. Specifically, grazing can lead to the onset of chaotic motion, multistability, or the sudden disappearance of stable periodic orbits [112, 116]. Region B, characterized by two grazing events per cycle, may be particularly susceptible to such transitions under perturbations in the system's parameters. Region C, with a single grazing point, similarly represents a regime near the boundary of qualitative change. While a detailed investigation of these behaviors lies beyond the scope of the present work, future studies could employ tools such as Lyapunov exponent analysis or Poincaré mapping to explore the potential for quasiperiodic or chaotic dynamics in these regimes. Such behaviors, if present, may also correlate with increased variability or amplification in the acceleration transmitted to the hand, further emphasizing the need to characterize grazing-induced transitions.

These results suggest that the observed rise in hand-arm acceleration is likely driven primarily by the increase in excitation force, rather than by grazing phenomena themselves. This raises an important question: does grazing meaningfully influence the hand-arm response, or is its effect negligible compared to excitation amplitude? A more detailed investigation may be required to isolate the role of grazing and determine whether it contributes independently to the vibration intensity perceived at the hand.

5.2.6 Effect of Absorber on Hand–Arm Acceleration Frequency Response

Having examined the effect of grazing on the hand–arm system response, we now turn to the role of the absorber in reducing hand–arm acceleration. To do this, we evaluate the acceleration at the hand in regions where grazing occurs at two different frequencies, with particular attention to the case of $F_{\text{ref}} = 80\,\text{N}$.

The results indicate that the absorber can reduce acceleration at the hand–arm interface. However, for it to be effective, the absorber mass must be greater than that of the tool. This analysis also shows that the absorber does not exert a uniform influence across the different frequency regions. The configuration with $m_N = 1.2\,m_H$ demonstrates some effectiveness and appears to play a more dominant role when the system operates above 500 Hz. .

5.3 Discussion

The results of the parametric study suggest that the onset of grazing in the tool is strongly influenced by the level of feed force applied. Specifically, the findings show that increasing or decreasing the feed force can either eliminate or induce grazing behavior within the system. This sensitivity of grazing to feed force reinforces prior experimental observations that feed force plays a critical role in determining the acceleration output at the handle [100].

Analysis of the hand–arm acceleration across different grazing regimes—including regions of no grazing, single grazing, and dual grazing—reveals that the presence or absence of grazing does not substantially alter the shape or structure of the hand–arm acceleration

FRF. Instead, increases in acceleration amplitude appear to be primarily driven by changes in excitation force. This challenges the original hypothesis that grazing significantly affects the vibrations transmitted to the hand.

Evaluation of the cubic absorber system indicates that the absorber mass must be on the order of the tool mass to achieve a substantial reduction in hand acceleration. This finding suggests the value of formulating an optimization problem to investigate whether alternative absorber parameter choices could yield improved performance. It also highlights the potential of exploring an inerter-based device, which could increase the effective mass of the absorber without increasing its physical mass. The absorber did, however, show a marked improvement in performance beyond the frequency corresponding to the first grazing point. This indicates that absorber performance could be optimized by using grazing points as predictors for frequency ranges where they may be most effective.

These observations highlight the need for experimental validation to determine whether the emergence or disappearance of grazing meaningfully influences hand–arm acceleration in practice. They also motivate further refinement of the vibroimpact model to enhance its predictive fidelity for vibration transmission to the user. In particular, improving how the model captures contact dynamics and its coupling with the hand–arm system could provide better alignment between simulated and experimentally observed behavior.

Conclusion

This study explored the nonlinear dynamics of a chipping hammer system to better understand how grazing behavior influences vibrations transmitted to the hand–arm interface. The effectiveness of a cubic absorber in reducing hand acceleration in the presence of grazing was also investigated. A vibroimpact model was developed to capture the percussive nature of the tool and was coupled to a hand–arm system, with parameters tuned to match experimentally observed natural frequencies of a chipping hammer.

Using numerical continuation via the COCO toolbox, grazing bifurcations were systematically identified in the (ω, F_{ref}) parameter space. The results showed that grazing events appear and disappear depending on excitation amplitude. At low amplitudes, no grazing is observed; at higher amplitudes, two grazing points emerge, which eventually merge into a single grazing point as excitation continues to increase.

A parametric study on feed force revealed that increasing the feed force lowers the excitation amplitude at which grazing begins and broadens the frequency interval over which grazing occurs. In some cases, feed force also altered the number of grazing points from two to one, indicating shifts in the underlying dynamics. Despite these changes in grazing characteristics, their effect on hand–arm acceleration was relatively modest. Analysis of the cubic absorber showed that its mass would need to be on the order of, or greater than, the tool mass to meaningfully reduce acceleration at the hand.

Overall, the findings suggest that while feed force is a useful parameter for modulating the onset and structure of grazing, vibration levels at the hand are not strongly determined by grazing behavior alone. This underscores the need for experimental validation and motivates further refinement of the vibroimpact model to more accurately capture tool–hand interactions. The results also point to promising future directions, such as formulating an optimization problem for absorber design and exploring devices like inerters that could enhance absorber performance without requiring excessive added mass.

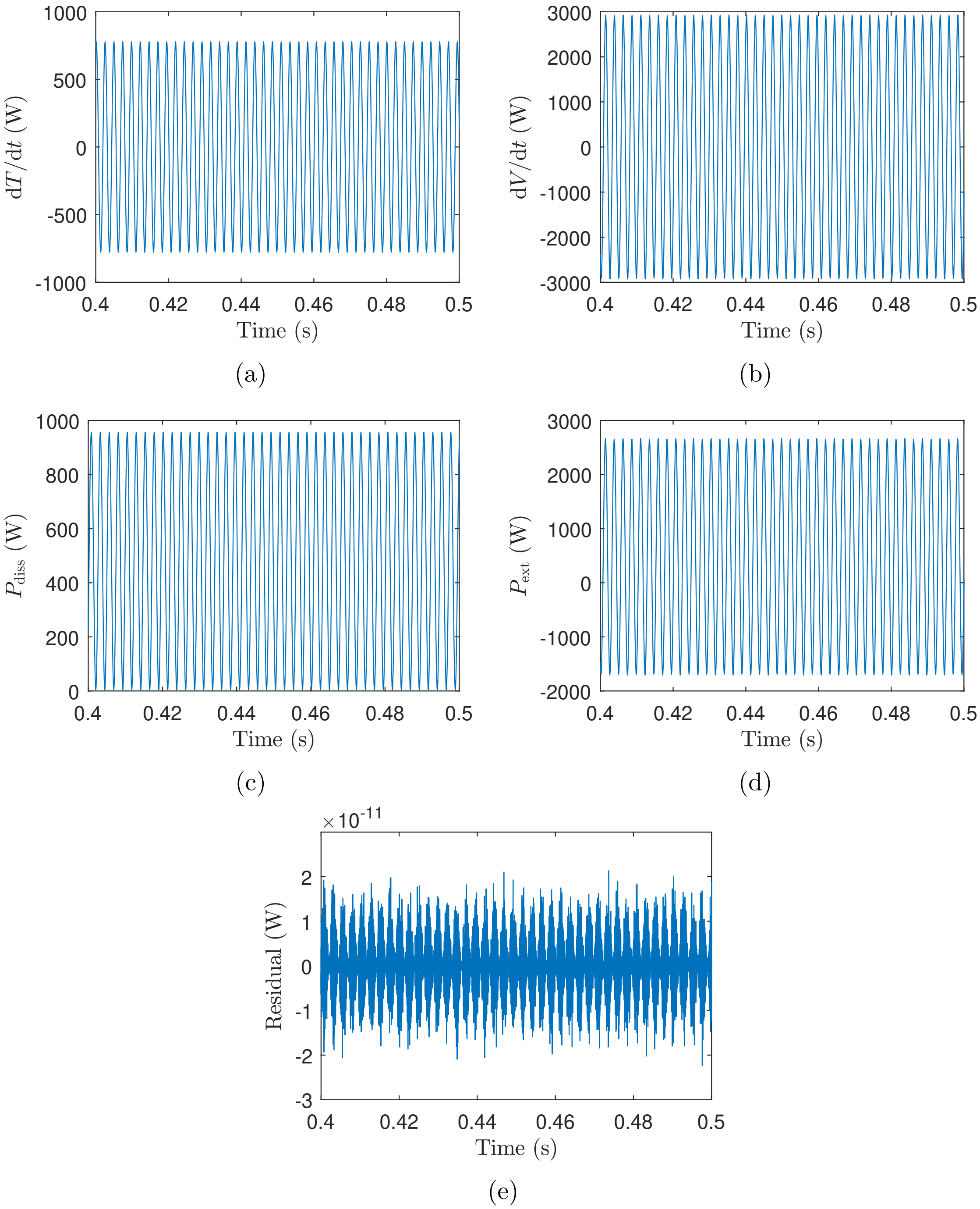

(a) (b) (c) (d) (e)

Figure 5.3: Time histories of (a) the time derivative of kinetic energy, (b) the time derivative of potential energy, (c) dissipated power, and (d) external input power for a representative numerical simulation. These quantities are used to evaluate (e) the residual of the energy balance..

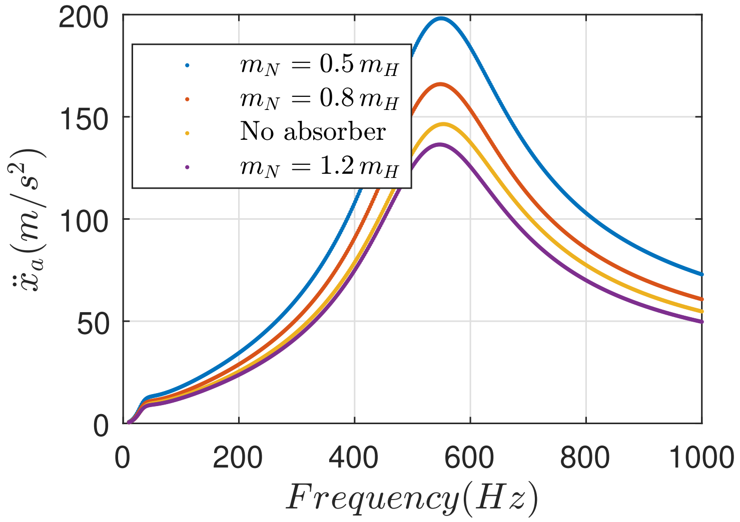

(a)

Figure 5.4: Frequency response function (FRF) of hand acceleration $\ddot{x}_a$ versus excitation frequency, showing performance of various absorber designs vs the system with no absorber.

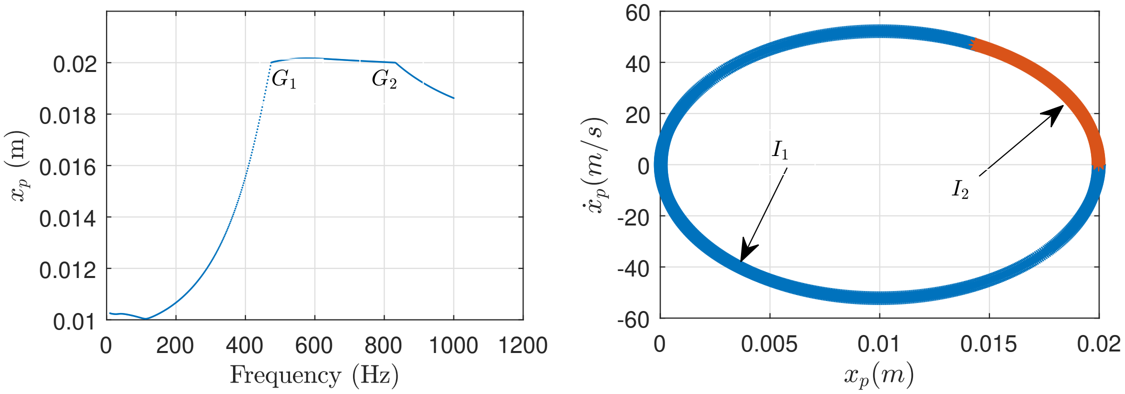

(a) (b)

Figure 5.5: a) Bifurcation diagram showing two points where the system grazes as reflected by the tooltip displacement at xp =0.02. b) The phase portrait which is used as the initial multisegment solution to be fed into COCO's hspo toolbox. Both diagrams are generated using the parameters in Table 5.1.

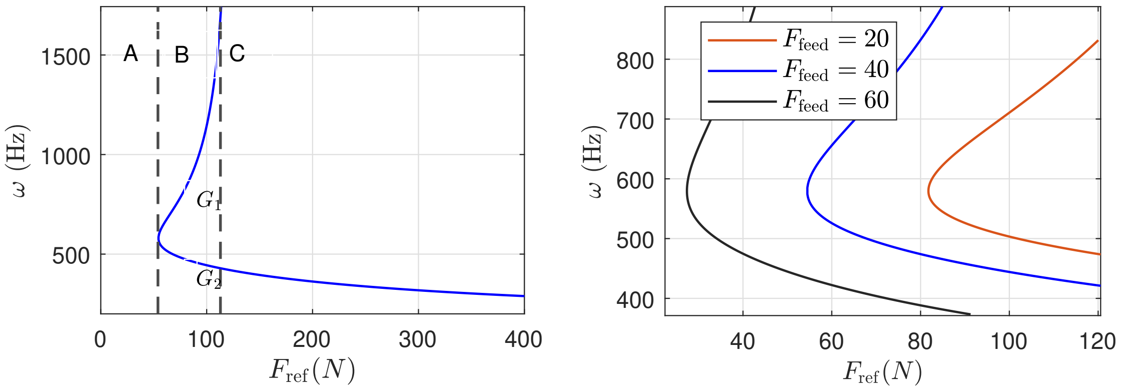

(a) (b)

Figure 5.6: a) Continuation of grazing points in the $(\omega, F_{\mathrm{ref}})$ parametric space. The previously identified grazing points G_1 and G_2 from Fig. 5.5a are marked along the grazing curve. Region A corresponds to parameter values where no grazing occurs, Region B indicates the presence of two distinct grazing points, and Region C marks the boundary beyond which one grazing point disappears. b) Comparison of grazing curves in the $(\omega, F_{\mathrm{ref}})$ space for three different feed force values.

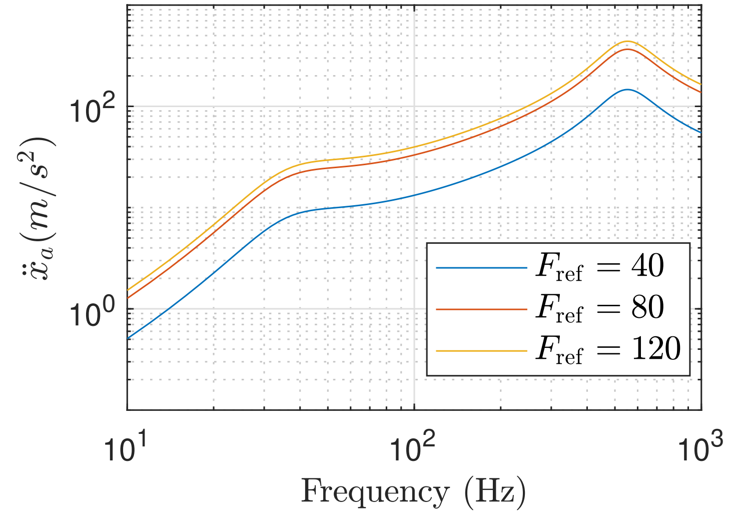

(a)

Figure 5.7: Comparison of hand-arm acceleration across different grazing regimes for $F_{feed} = 40N$. At $F_{\mathrm{ref}} = 40$ N, the system operates in Region A where no grazing occurs, as seen in Fig. 5.6. At $F_{\mathrm{ref}} = 100$ N, the system grazes at two frequencies (Region B), while at $F_{\mathrm{ref}} = 120$ N, grazing occurs at only one frequency (Region C). This figure highlights how transitions between grazing regimes influence the vibration response at the hand-arm interface.

Chapter 6

Conclusion

This dissertation presented an investigation into two models of impact tools: a vibroimpact model and a cubic oscillator model. These models were further coupled to a hand-arm system to study how vibrations are transmitted to the operator. The performance of both linear and cubic absorbers in mitigating hand-transmitted vibrations was then explored using numerical and analytical techniques. Most of the numerical solutions in this work were obtained using MATLAB's ode45 solver.

The first study focused on modeling the tool as a cubic oscillator while evaluating the ability of linear and nonlinear absorbers to reduce vibrations transmitted to the hand. Key results showed that nonlinear absorbers consistently outperformed linear absorbers due to nonlinear phenomena inherent to the cubic model of the impact tool. In particular, at higher excitation force amplitudes, the cubic oscillator exhibited a nonlinear behavior known as hardening resonance. This caused the linear tuned vibration absorber (TVA) to become detuned and thus ineffective. In contrast, the nonlinear vibration absorbers (NVAs) maintained their effectiveness under these conditions, preserving a wide frequency band for vibration suppression. We also observed patterns in how absorber parameters influenced performance, highlighting the potential for identifying optimal absorber parameters tailored to this application.

The second study shifted focus to a cubic oscillator with greater emphasis on nonlinear dynamical tools such as Lyapunov exponents, phase portraits, and Poincaré maps. Results revealed the presence of bifurcation points, limit cycles, and aperiodic solutions. Using bifurcation diagrams and Lyapunov exponents, we identified distinct regions where the system exhibited quasi-periodic and chaotic solutions. These regions were termed unsafe operating regions because the system's frequency response function (FRF) showed dominant frequency components—arising in the presence of quasiperiodicity or chaos—that could be damaging to the hand. Notably, this analysis demonstrated the absorber's ability to control the emergence and suppression of aperiodic motion—an important capability for reducing harmful vibrations at the hand.

The third study examined the dynamics of the chipping hammer when modeled with vibroimpact nonlinearities and coupled to the hand–arm system. Using nonlinear dynamical analysis tools, this work revealed both periodic and aperiodic motion, similar to the findings of the second study. Interestingly, we observed that transitions from periodic to aperiodic motion led to an amplification of vibration magnitude at the hand. Regarding absorber performance, we found that the absorber was more effective in reducing vibrations during periodic motion than in the presence of aperiodic motion. Key parameters, including absorber stiffness and applied feed force, were studied in detail. The analysis showed that the nonlinear tuned vibration absorber (NLTVA) could either attenuate or amplify vibrations transmitted to the hand, depending on the excitation force range of the handheld impact machine (HHIM).

In the fourth study, the vibroimpact model of the tool was validated using experimental frequency response data. Building on this validation, the study explored the influence of grazing dynamics on the coupled tool–hand system and assessed absorber performance under these conditions. The results revealed that the appearance of grazing points in the system was controlled by both the excitation forcing amplitude and the applied feed force. These parameters determined the number of excitation frequency values at which grazing occurred, as well as the spacing between those values when multiple grazing points were present.

Furthermore, the analysis showed that, for the set of system parameters studied, the number of grazing points (0, 1, or 2) did not significantly affect the overall hand–arm response. Finally, it was found that a cubic absorber could still reduce hand–arm acceleration in the presence of grazing.

Collectively, these studies demonstrate the wide range of nonlinear phenomena exhibited by impact tools and their absorbers—phenomena that can be compared with experimental findings for validation. This work provides a framework for selecting appropriate models of impact tools and for making engineering decisions about whether a nonlinear absorber should be incorporated into tool design.

Chapter 7

Future Work

While this dissertation provides a foundation for understanding how impact tools can be modeled and how absorber parameters may be selected, several avenues remain for further exploration.

First, further experimental work is required to verify whether the cubic and vibro-impact models can accurately capture the dynamics of a physical chipping hammer. Direct comparisons between experimental data and the bifurcation and continuation diagrams generated in this study would help validate the models. For this task, it would be helpful to compare qualitative rather than purely quantitative dynamics—for example, examining transitions between periodic and aperiodic motion as presented in this dissertation. Additionally, phenomena such as grazing should be compared between experimental observations and analytical model predictions to further assess model fidelity.

Second, potential expressions in the mathematical model could be refined to improve accuracy. For example, the excitation force acting on the tool body could be better represented, as could the feed force applied during operation. Given that it is difficult to maintain a steady feed force in practice, it would be valuable to develop a mathematical expression that captures its variability rather than employing the static feed force assumption used in this study.

Third, the complexity of the models could be expanded by incorporating additional terms, such as drift, to improve the representation of ground–tool interaction. At the same time, it is important to retain simplicity by keeping the number of terms as small as possible. This balance would support the identification of simplified models that are still capable of replicating experimental results relevant to hand–tool dynamics, particularly in terms of acceleration transfer.

Fourth, the findings from this dissertation suggest a practical step-by-step framework for designing vibration absorbers for new percussive tools:

1. **Model development and validation:** Begin by developing a vibro-impact system model, similar to that presented in this study, to capture the dynamic behavior of the tool. The model should be tuned to reproduce the tool's frequency response function (FRF) under various operating conditions (e.g., different feed forces). In this study, the FRF of the vibro-impact system was validated under one operating condition; however, future work should extend this validation to a wider range of conditions to improve model robustness.

2. **Absorber parameter optimization:** Once validated, append a mass–spring–damper model representing the absorber to the tool. Systematically tune absorber parameters to reduce hand-transmitted acceleration across the operating frequency range. Nonlinear dynamical tools—such as bifurcation diagrams and Lyapunov exponent maps—should be employed to identify parameter combinations that yield stable and effective vibration suppression.

3. **Physical implementation:** Finally, design a physical absorber with parameters matching those determined analytically. The absorber's mass should be selected according to the optimal value identified in simulation, and the spring should be chosen to replicate the corresponding viscoelastic stiffness properties.

This procedure provides a systematic pathway for translating the modeling insights from this dissertation into practical absorber designs for real-world impact tools.

Fifth, the efficacy of the absorber should be further examined experimentally. In particular, various inerter designs could be combined with cubic absorbers in different configurations with the tool to investigate how effectively such designs reduce hand-transmitted acceleration. In some situations, since it has been noted that absorber mass may need to be more than 0.2 times the primary system mass to be effective, it is worth exploring how the addition of an inerter could replicate the benefits of oversized absorbers while remaining practical in design. The use of inerters may therefore enable absorber configurations that achieve strong vibration attenuation without the impracticality of physically large absorber masses.

Finally, to further improve user comfort, absorber designs—either in combination with other vibration control devices or considered independently—should be evaluated not only for their ability to reduce hand-transmitted acceleration but also for their contribution to overall operator comfort.

Appendices

Appendix A

Expressions used in Eqs. (2.2) and (2.3)

$$[\mathbf{M}] = \begin{bmatrix} m_H + m_s & 0 & 0 \\ 0 & m_a & 0 \\ 0 & 0 & b + m_N \end{bmatrix}$$

$$[\mathbf{C}] = \begin{bmatrix} c_H + c_N + c_s & -c_s & -c_N \\ -c_s & c_a + c_s & 0 \\ -c_N & 0 & c_N \end{bmatrix}$$

$$[\mathbf{K}] = \begin{bmatrix} k_H L + k_N L + k_s & -k_s & -k_N L \\ -k_s & k_a + k_s & 0 \\ -k_N & 0 & k_N \end{bmatrix}$$

$$[\mathbf{N}] = \begin{bmatrix} k_H x_H^3 + k_N \left(x_H - x_N\right)^3 \\ 0 \\ k_N \left(x_N - x_H\right)^3 \end{bmatrix}$$

$$[\mathbf{F_{eq}}] = \begin{bmatrix} \frac{\omega^2 F_{\mathrm{ref}} sin(\omega t)}{\omega_{\mathrm{ref}}^2} \\ 0 \\ 0 \end{bmatrix}$$

$$[\mathbf{N_1}] = \begin{bmatrix} k_H \left(a1 \cos\left(\omega t\right) + b1 \sin\left(\omega t\right)\right)^3 \\ 0 \\ k_N \left(x_N - x_H\right)^3 \\ + k_N \left(a1 \cos\left(\omega t\right) + b1 \sin\left(\omega t\right) e1 \cos\left(\omega t\right) - f1 \sin\left(\omega t\right)\ \right)^3 \\ - \\ - \end{bmatrix}$$

Appendix B

Expressions used in Eqs. (3.1), (3.3) and (3.6)

$$[\mathbf{M}] = \begin{bmatrix} m_H + m_s & 0 & 0 \\ 0 & m_a & 0 \\ 0 & 0 & m_N + b \end{bmatrix}$$

$$[\mathbf{C}] = \begin{bmatrix} c_H + c_N + c_s & -c_s & -c_N \\ -c_s & c_a + c_s & 0 \\ -c_N & 0 & c_N \end{bmatrix}$$

$$[\mathbf{K}] = \begin{bmatrix} k_{HL} + k_{NL} + k_s & -k_s & -k_{NL} \\ -k_s & k_a + k_s & 0 \\ -k_{NL} & 0 & k_{NL} \end{bmatrix}$$

$$[\mathbf{f}_{nl}] = \begin{bmatrix} k_N\left(x_H - x_N\right)^3 + k_H x_H^3 \\ 0 \\ k_N\left(x_N - x_H\right)^3 \end{bmatrix}$$

$$[\mathbf{F}_{eq}] = \begin{bmatrix} F_w \\ 0 \\ 0 \end{bmatrix}$$

$$[\mathbf{M1}] = \begin{bmatrix} 1 & 0 & 0 \\ 0 & 1 & 0 \\ 0 & 0 & 1 \end{bmatrix}$$

$$[\mathbf{C1}] = \begin{bmatrix} -2\zeta_1 + 2\zeta_2 + 2\zeta_3 & -2\zeta_2 & -2\zeta_3 \\ -2\zeta_3\alpha & 0 & 2\zeta_3\alpha \\ -2\zeta_2\alpha_2 & 2\zeta_4\alpha_2 + 2\zeta_2\alpha_2 & 0 \end{bmatrix}$$

$$[\mathbf{K1}] = \begin{bmatrix} 1 + k_{r1} + k_{r2} & -k_{r1} & -k_{r2} \\ -k_{r2}\alpha & 0 & k_{r2}\alpha \\ -k_{r1}\alpha_2 & k_{r3}\alpha_2 + k_{r1}\alpha_2 & 0 \end{bmatrix}$$

$$[\mathbf{f1}_{nl}] = \begin{bmatrix} k_{rnl1} y_H^3 + k_{rnl2} \left(y_H - y_N \right)^3 \\ k_{rnl2} \alpha \left(y_N - y_H \right)^3 \\ 0 \end{bmatrix}$$

$$[\mathbf{F1}_{eq}] = \begin{bmatrix} F\, \Omega^2 \sin\left(\Omega \tau \right) \\ 0 \\ 0 \end{bmatrix}$$

$$[\mathbf{A}] = \begin{bmatrix} 0 & -1 & 0 & 0 & 0 & 0 \\ k_{r1} + k_{r2} + 1 & -2\zeta_1 + 2\zeta_2 + 2\zeta_3 & -k_{r1} & -2\zeta_2 & -k_{r2} & -2\zeta_3 \\ 0 & 0 & 0 & -1 & 0 & 0 \\ \alpha(-k_{r2}) & -2\alpha\zeta_3 & 0 & 0 & \alpha k_{r2} & 2\alpha\zeta_3 \\ 0 & 0 & 0 & 0 & 0 & -1 \\ \alpha_2 \left(-k_{r1} \right) & -2\alpha_2\zeta_2 & \alpha_2 k_{r1} + \alpha_2 k_{r3} & 2\alpha_2\zeta_2 + 2\alpha_2\zeta_4 & 0 & 0 \end{bmatrix}$$

$$[\mathbf{N_1}]=$$

$$\left[\begin{array}{c} 0 \\ k_{\mathrm{rnl1}}\left(C_1\cos(\Omega\,\tau)+D_1\sin(\Omega\,\tau)\right)^3+k_{\mathrm{rnl2}}\left((C_1-C_5)\cos(\Omega\,\tau)+(D_1-D_5)\sin(\Omega\,\tau)\right)^3 \\ 0 \\ \alpha k_{\mathrm{rnl2}}\left(\left(C_1\cos(\Omega\,\tau)+D_1\sin(\Omega\,\tau)\right)^3+3\left(C_5\cos(\Omega\,\tau)+D_5\sin(\Omega\,\tau)\right)\left(C_1\cos(\Omega\,\tau)+D_1\sin(\Omega\,\tau)\right)^2\right. \\ 0 \\ 0 \end{array}\right.$$

$$\left.\begin{array}{c} - \\ - \\ - \\ \left.-3\left(C_5\cos(\Omega\,\tau)+D_5\sin(\Omega\,\tau)\right)^2\left(C_1\cos(\Omega\,\tau)+D_1\sin(\Omega\,\tau)\right)+\left(C_5\cos(\Omega\,\tau)+D_5\sin(\Omega\,\tau)\right)^3\right) \\ - \\ - \end{array}\right]$$

$$[\mathbf{F_{eq}}]=\begin{bmatrix} 0 \\ F\Omega^2\sin(\Omega\,\tau) \\ 0 \\ 0 \\ 0 \\ 0 \end{bmatrix}$$

Bibliography

[1] Elsjebe Sampson and Johannes L Van Niekerk. Literature survey on anti-vibration gloves. 2003.

[2] Bibhuti B Mandal and Anup K Srivastava. Risk from vibration in indian mines. *Indian Journal of Occupational and Environmental Medicine*, 10(2):53, 2006.

[3] Keith T Palmer, Michael J Griffin, Holly Syddall, Brian Pannett, Cyrus Cooper, and David Coggon. Risk of hand-arm vibration syndrome according to occupation and sources of exposure to hand-transmitted vibration: A national survey. *American Journal of Industrial Medicine*, 39(4):389–396, 2001.

[4] Alex Burdorf, Guido Govaert, and Leo Elders. Postural load and back pain of workers in the manufacturing of prefabricated concrete elements. *Ergonomics*, 34(7):909–918, 1991.

[5] Silvia Carra, Luigi Monica, and Giuseppe Vignali. Reduction of workers' hand-arm vibration exposure through optimal machine design: Ahp methodology applied to a case study. *Safety Science*, 120:706–727, 2019.

[6] Giovanni Moschioni, Bortolino Saggin, and Marco Tarabini. Prediction of data variability in hand-arm vibration measurements. *Measurement*, 44(9):1679–1690, 2011.

[7] Bortolino Saggin, Diego Scaccabarozzi, and Marco Tarabini. Optimized design of suspension systems for hand–arm transmitted vibration reduction. *Journal of sound and vibration*, 331(11):2671–2684, 2012.

[8] Reiner Jahn and Michael Hesse. Applications of hand-arm models in the investigation of the interaction between man and machine. *Scandinavian journal of work, environment & health*, pages 343–346, 1986.

[9] Michał Śledziński. Proposed model of hand for designing ergonomic vibration isolation systems for hand-held impact tools. *American Journal of Mechanical Engineering*, 2(7):290–294, 2014.

[10] RR Aguiar, EFV d'Almeida, and TG Ritto. Vibro-impact model and validation of the axial dynamics of a vibration-assisted drilling tool. *Journal of the Brazilian Society of Mechanical Sciences and Engineering*, 42:1–16, 2020.

[11] Ekaterina Pavlovskaia, David C Hendry, and Marian Wiercigroch. Modelling of high frequency vibro-impact drilling. *International Journal of Mechanical Sciences*, 91:110–119, 2015.

[12] Ekaterina Pavlovskaia, Marian Wiercigroch, and Celso Grebogi. Modeling of an impact system with a drift. *Physical Review E*, 64(5):056224, 2001.

[13] Oreoluwa Alabi, Sunit Kumar Gupta, and Oumar Barry. Dynamics of a nonlinear absorber and hand-held impact machine. In *International Design Engineering Technical Conferences and Computers and Information in Engineering Conference*, volume 86304, page V009T09A022. American Society of Mechanical Engineers, 2022.

[14] Oreoluwa Alabi, Sunit Kumar Gupta, and Oumar Barry. Vibration analysis of a nonlinear absorber coupled to a hand-held impact machine. *Journal of Computational and Nonlinear Dynamics*, pages 1–18, 2023.

[15] Marian Wiercigroch and Ekaterina Pavlovskaia. Nonlinear dynamics of vibro-impact

systems: theory and experiments. In *Materials science forum*, volume 440, pages 513–520. Trans Tech Publ, 2003.

[16] Qing-Jie Cao, Marian Wiercigroch, Ekaterina Pavlovskaia, and Shao-Pu Yang. Bifurcations and the penetrating rate analysis of a model for percussive drilling. *Acta Mechanica Sinica*, 26(3):467–475, 2010.

[17] Marian Wiercigroch. Applied nonlinear dynamics of non-smooth mechanical systems. *Journal of the Brazilian Society of Mechanical Sciences and Engineering*, 28(4):519–526, 2006.

[18] Jee-Hou Ho, Van-Du Nguyen, and Ko-Choong Woo. Nonlinear dynamics of a new electro-vibro-impact system. *Nonlinear dynamics*, 63(1):35–49, 2011.

[19] Ren G Dong, Jennie H Dong, John Z Wu, and Subhash Rakheja. Modeling of biodynamic responses distributed at the fingers and the palm of the human hand–arm system. *Journal of Biomechanics*, 40(10):2335–2340, 2007.

[20] Jennie H Dong, Ren G Dong, Subhash Rakheja, Daniel E Welcome, Thomas W McDowell, and John Z Wu. A method for analyzing absorbed power distribution in the hand and arm substructures when operating vibrating tools. *Journal of Sound and Vibration*, 311(3-5):1286–1304, 2008.

[21] Ko Ying Hao and Zaidi Mohd Ripin. Nodal control of grass trimmer handle vibration. *International Journal of Industrial Ergonomics*, 43(1):18–30, 2013.

[22] WB Liu, HL Dai, and L Wang. Suppressing wind-induced oscillations of prismatic structures by dynamic vibration absorbers. *International Journal of Structural Stability and Dynamics*, 17(06):1750056, 2017.

[23] Oumar Barry and Mohammad Bukhari. On the modeling and analysis of an energy harvester moving vibration absorber for power lines. In *Dynamic Systems and Control Conference*, volume 58288, page V002T23A005. American Society of Mechanical Engineers, 2017.

[24] Mariano Febbo. Optimal parameters and characteristics of a three degree of freedom dynamic vibration absorber. *Journal of vibration and acoustics*, 134(2), 2012.

[25] Saleh Shakeri and Farhad S Samani. Application of linear and nonlinear vibration absorbers in micro-milling process in order to suppress regenerative chatter. *Nonlinear Dynamics*, 89(2):851–862, 2017.

[26] H Moradi, F Bakhtiari-Nejad, and MR Movahhedy. Tuneable vibration absorber design to suppress vibrations: an application in boring manufacturing process. *Journal of Sound and Vibration*, 318(1-2):93–108, 2008.

[27] N Harada and MH Mahbub. Diagnosis of vascular injuries caused by hand-transmitted vibration. *International archives of occupational and environmental health*, 81(5):507–518, 2008.

[28] Michael J Griffin. *Handbook of human vibration.* Academic press, 2012.

[29] Bruce P Bernard and Vern Putz-Anderson. Musculoskeletal disorders and workplace factors; a critical review of epidemiologic evidence for work-related musculoskeletal disorders of the neck, upper extremity, and low back. 1997.

[30] ISO ISO. 5349-1: Mechanical vibration—measurement and evaluation of human exposure to hand-transmitted vibration—part 1: general requirements. *Geneva, Switzerland: International Organization for Standardization*, 62, 2001.

[31] Per Vihlborg, Liss Bryngelsson, Bernt Lindgren, Lars Gunnar Gunnarsson, and Pål Graff. Association between vibration exposure and hand-arm vibration symptoms in a swedish mechanical industry. *International Journal of Industrial Ergonomics*, 62:77–81, 2017.

[32] MJ Griffin, M Bovenzi, and CM Nelson. Dose-response patterns for vibration-induced white finger. *Occupational and Environmental Medicine*, 60(1):16–26, 2003.

[33] Ren G Dong, John Z Wu, and Daniel E Welcome. Recent advances in biodynamics of human hand-arm system. *Industrial health*, 43(3):449–471, 2005.

[34] L Barregard, L Ehrenström, and K Marcus. Hand-arm vibration syndrome in swedish car mechanics. *Occupational and environmental medicine*, 60(4):287–294, 2003.

[35] American National Standards Institute. *Guide for the Measurement and Evaluation of Human Exposure to Vibration Transmitted to the Hand.* 1986.

[36] Lars E Necking, Göran Lundborg, Ronnie Lundström, Lars-Eric Thornell, and Jan Fridén. Hand muscle pathology after long-term vibration exposure. *Journal of Hand Surgery*, 29(5):431–437, 2004.

[37] Trygve Strömberg, Lars B Dahlin, Arne Brun, and Goran Lundborg. Structural nerve changes at wrist level in workers exposed to vibration. *Occupational and environmental medicine*, 54(5):307–311, 1997.

[38] C Heaver, KS Goonetilleke, H Ferguson, and S Shiralkar. Hand–arm vibration syndrome: a common occupational hazard in industrialized countries. *Journal of Hand Surgery (European Volume)*, 36(5):354–363, 2011.

[39] GHMJ Subashi De Silva and TRST Wijewardana. Preliminary results of hand arm vibration (hav) exposures of chipping hammer operators in tropical weather: Analysis

of exposures and protective gloves. *International Journal of Industrial Ergonomics*, 86:103197, 2021.

[40] Mónica López-Alonso, Rosalía Pacheco-Torres, Ma Dolores Martínez-Aires, and Javier Ordoñez-García. Comparative analysis of exposure limit values of vibrating hand-held tools. *International journal of industrial ergonomics*, 43(3):218–224, 2013.

[41] Ren G Dong, Daniel E Welcome, John Z Wu, and Thomas W McDowell. Development of hand-arm system models for vibrating tool analysis and test rig construction. *Noise Control Engineering Journal*, 56(1):35–44, 2008.

[42] Ren G Dong, Thomas W McDOWELL, and Daniel E Welcome. Biodynamic response at the palm of the human hand subjected to a random vibration. *Industrial Health*, 43(1):241–255, 2005.

[43] Luiz Fernando P Franca and Hans Ingo Weber. Experimental and numerical study of a new resonance hammer drilling model with drift. *Chaos, Solitons & Fractals*, 21(4):789–801, 2004.

[44] Sunit K Gupta, Oreoluwa Alabi, Paul-Camille Kakou, and Oumar Barry. On the modeling and optimization of anti-vibration gloves for hand-arm vibration control. In *ASME 2019 Dynamic Systems and Control Conference*. American Society of Mechanical Engineers Digital Collection.

[45] Oreoluwa Alabi, Sunit K Gupta, and Oumar Barry. Theoretical analysis and optimization of a gloved hand–arm system. *Journal of Biomechanical Engineering*, 143(9), 2021.

[46] Hermann Frahm. Device for damping vibrations of bodies., April 18 1911. US Patent 989,958.

[47] Nakhorn Poovarodom, Sopak Kanchanosot, and Pennung Warnitchai. Application of non-linear multiple tuned mass dampers to suppress man-induced vibrations of a pedestrian bridge. *Earthquake engineering & structural dynamics*, 32(7):1117–1131, 2003.

[48] Walter Lacarbonara and Marek Cetraro. Flutter control of a lifting surface via visco-hysteretic vibration absorbers. *International Journal of Aeronautical and Space Sciences*, 12(4):331–345, 2011.

[49] Min Wang. Feasibility study of nonlinear tuned mass damper for machining chatter suppression. *Journal of Sound and Vibration*, 330(9):1917–1930, 2011.

[50] Hans Lindell, Viktor Berbyuk, MATTIAS JOSEFSSON, and Snævar Leó Grétarsson. Nonlinear dynamic absorber to reduce vibration in hand-held impact machines. In *In Proc. of the International Conference on Engineering Vibration, Ljubljana, 7-10 September;[editors Miha Boltežar, Janko Slavič, Marian Wiercigroch].-EBook.-Ljubljana: Faculty for Mechanical Engineering, 2015*, pages 1530–1539, 2015.

[51] Régis Viguié and Gaëtan Kerschen. Nonlinear vibration absorber coupled to a nonlinear primary system: a tuning methodology. *Journal of sound and Vibration*, 326(3-5):780–793, 2009.

[52] Vladimir I Babitsky. *Theory of vibro-impact systems and applications*. Springer Science & Business Media, 2013.

[53] Giuseppe Habib, Thibaut Detroux, Régis Viguié, and Gaëtan Kerschen. Nonlinear generalization of den hartog s equal-peak method. *Mechanical Systems and Signal Processing*, 52:17–28, 2015.

[54] Steven H Strogatz. Nonlinear dynamics and chaos: with applications to physics, biology, chemistry, and engineering (studies in nonlinearity). *Nonlinear Dynamics and Chaos: With Applications to Physics, Biology, Chemistry, and Engineering (Studies in Nonlinearity)*, 2001.

[55] Cristiano Martinelli, Andrea Coraddu, and Andrea Cammarano. Approximating piecewise nonlinearities in dynamic systems with sigmoid functions: advantages and limitations. *Nonlinear Dynamics*, 111(9):8545–8569, 2023.

[56] Antonio SE Chong, Yuan Yue, Ekaterina Pavlovskaia, and Marian Wiercigroch. Global dynamics of a harmonically excited oscillator with a play: numerical studies. *International Journal of Non-Linear Mechanics*, 94:98–108, 2017.

[57] Keguan Zou and Satish Nagarajaiah. Study of a piecewise linear dynamic system with negative and positive stiffness. *Communications in Nonlinear Science and Numerical Simulation*, 22(1-3):1084–1101, 2015.

[58] James Ing, Ekaterina Pavlovskaia, and Marian Wiercigroch. Complex nonlinear response of a piecewise linear oscillator: Experiment and simulation. In *IUTAM Symposium on Dynamics Modeling and Interaction Control in Virtual and Real Environments: Proceedings of the IUTAM Symposium on Dynamics Modeling and Interaction Control in Virtual and Real Environments, Held in Budapest, Hungary, June 7–11, 2010*, pages 135–143. Springer, 2011.

[59] Rui Vasconcellos, Abdessattar Abdelkefi, Muhammad R Hajj, and Flávio Donizeti Marques. Grazing bifurcation in aeroelastic systems with freeplay nonlinearity. *Communications in Nonlinear Science and Numerical Simulation*, 19(5):1611–1625, 2014.

[60] Shan Yin, Jinchen Ji, and Guilin Wen. Complex near-grazing dynamics in impact oscillators. *International Journal of Mechanical Sciences*, 156:106–122, 2019.

[61] Chun-Pu Tsai and Wei-Chang Li. Micromechanical vibro-impact systems: a review. *Journal of Micromechanics and Microengineering*, 2023.

[62] Lawrence D Zavodney, AH Nayfeh, and NE Sanchez. The response of a single-degree-of-freedom system with quadratic and cubic non-linearities to a principal parametric resonance. *Journal of Sound and Vibration*, 129(3):417–442, 1989.

[63] Joseph Páez Chávez, Piotr Brzeski, and Przemyslaw Perlikowski. Bifurcation analysis of non-linear oscillators interacting via soft impacts. *International Journal of Non-Linear Mechanics*, 92:76–83, 2017.

[64] Steven Wayne Shaw and Philip J Holmes. A periodically forced piecewise linear oscillator. *Journal of sound and vibration*, 90(1):129–155, 1983.

[65] Michael Kleczka, Edwin Kreuzer, and Werner Schiehlen. Local and global stability of a piecewise linear oscillator. *Philosophical Transactions of the Royal Society of London. Series A: Physical and Engineering Sciences*, 338(1651):533–546, 1992.

[66] Shan Yin, Guilin Wen, Jinchen Ji, and Huidong Xu. Novel two-parameter dynamics of impact oscillators near degenerate grazing points. *International Journal of Non-Linear Mechanics*, 120:103403, 2020.

[67] JMT Thompson, AR Bokaian, and R Ghaffari. Subharmonic resonances and chaotic motions of a bilinear oscillator. *IMA Journal of Applied Mathematics*, 31(3):207–234, 1983.

[68] YB Kim and ST Noah. Stability and bifurcation analysis of oscillators with piecewise-linear characteristics: a general approach. 1991.

[69] June-Yule Lee. Motion behavior of impact oscillator. *Journal of Marine Science and Technology*, 13(2):3, 2005.

[70] Ugo Andreaus, Luca Placidi, and Giuseppe Rega. Numerical simulation of the soft contact dynamics of an impacting bilinear oscillator. *Communications in Nonlinear Science and Numerical Simulation*, 15(9):2603–2616, 2010.

[71] James Ing, Ekaterina Pavlovskaia, Marian Wiercigroch, and Soumitro Banerjee. Bifurcation analysis of an impact oscillator with a one-sided elastic constraint near grazing. *Physica D: Nonlinear Phenomena*, 239(6):312–321, 2010.

[72] Marcelo A Savi. Nonlinear dynamics and chaos. *Dynamics of Smart Systems and Structures: Concepts and Applications*, pages 93–117, 2016.

[73] Tousheng Huang, Liming Dai, and Huayong Zhang. An approach combining periodicity ratio and secondary poincaré map for characteristics diagnosis of nonlinear oscillatory systems. *Nonlinear Dynamics*, 84:959–975, 2016.

[74] Francis C Moon. *Chaotic and fractal dynamics: introduction for applied scientists and engineers*. John Wiley & Sons, 2008.

[75] IJ Sokolov, VI Babitsky, and NA Halliwell. Hand-held percussion machines with low emission of hazardous vibration. *Journal of sound and vibration*, 306(1-2):59–73, 2007.

[76] Bini Sam and K Kathirvel. Development and evaluation of vibration isolators for reducing hand transmitted vibration of walking and riding type power tillers. *Biosystems engineering*, 103(4):427–437, 2009.

[77] VK Tewari and KN Dewangan. Effect of vibration isolators in reduction of work stress during field operation of hand tractor. *Biosystems Engineering*, 103(2):146–158, 2009.

[78] Mattias Josefsson and Snævar Leó Grétarsson. Optimisation of a non-linear tuned vibration absorber in a hand-held impact machine. Master's thesis, 2015.

[79] EV Golysheva, VI Babitsky, and AM Veprik. Vibration protection for an operator of a hand-held percussion machine. *Journal of Sound and Vibration*, 274(1-2):351–367, 2004.

[80] Daniel E Welcome, Ren G Dong, Xueyan S Xu, Christopher Warren, and Thomas W McDowell. The effects of vibration-reducing gloves on finger vibration. *International journal of industrial ergonomics*, 44(1):45–59, 2014.

[81] K Hamouda, S Rakheja, KN Dewangan, and P Marcotte. Fingers' vibration transmission and grip strength preservation performance of vibration reducing gloves. *Applied ergonomics*, 66:121–138, 2018.

[82] VI Babitsky. Hand-held percussion machine as discrete non-linear converter. *Journal of Sound and Vibration*, 214(1):165–182, 1998.

[83] Kohju Ikago, Kenji Saito, and Norio Inoue. Seismic control of single-degree-of-freedom structure using tuned viscous mass damper. *Earthquake Engineering & Structural Dynamics*, 41(3):453–474, 2012.

[84] Jason Zheng Jiang, Alejandra Z Matamoros-Sanchez, Roger M Goodall, and Malcolm C Smith. Passive suspensions incorporating inerters for railway vehicles. *Vehicle System Dynamics*, 50(sup1):263–276, 2012.

[85] Fu-Cheng Wang, Min-Kai Liao, Bo-Huai Liao, Wei-Jiun Su, and Hsiang-An Chan. The performance improvements of train suspension systems with mechanical networks employing inerters. *Vehicle System Dynamics*, 47(7):805–830, 2009.

[86] A Giaralis and AA Taflanidis. Optimal tuned mass-damper-inerter (tmdi) design for seismically excited mdof structures with model uncertainties based on reliability criteria. *Structural Control and Health Monitoring*, 25(2):e2082, 2018.

[87] Yinlong Hu, Michael ZQ Chen, and Zhan Shu. Passive vehicle suspensions employing inerters with multiple performance requirements. *Journal of Sound and Vibration*, 333(8):2212–2225, 2014.

[88] Eshagh Farzaneh Joubaneh and Oumar Rafiou Barry. On the improvement of vibration mitigation and energy harvesting using electromagnetic vibration absorber-inerter: Exact h2 optimization. *Journal of Vibration and Acoustics*, 141(6), 2019.

[89] Toshihiko Asami, Osamu Nishihara, and Amr M Baz. Analytical solutions to h∞ and h 2 optimization of dynamic vibration absorbers attached to damped linear systems. *J. Vib. Acoust.*, 124(2):284–295, 2002.

[90] Chiara Grappasonni, Giuseppe Habib, Thibaut Detroux, Fengwen Wang, Gaëtan Kerschen, and Jakob Søndergaard Jensen. Practical design of a nonlinear tuned vibration absorber. In *Proceedings of the ISMA 2014 conference*, 2014.

[91] Laurentiu Marian and Agathoklis Giaralis. The tuned mass-damper-inerter for harmonic vibrations suppression, attached mass reduction, and energy harvesting. *Smart structures and systems*, 19(6):665–678, 2017.

[92] Nam Hoang, Yozo Fujino, and Pennung Warnitchai. Optimal tuned mass damper for seismic applications and practical design formulas. *Engineering structures*, 30(3):707–715, 2008.

[93] Maurizio De Angelis, Salvatore Perno, and Anna Reggio. Dynamic response and optimal design of structures with large mass ratio tmd. *Earthquake Engineering & Structural Dynamics*, 41(1):41–60, 2012.

[94] Oreoluwa Alabi and Oumar Barry. On the nonlinear vibration analysis of a hand-held

impact machine. In *Dynamic Systems and Control Conference*, volume 84287, page V002T29A004. American Society of Mechanical Engineers, 2020.

[95] Malte Krack and Johann Gross. *Harmonic balance for nonlinear vibration problems*, volume 1. Springer, 2019.

[96] Pankaj Wahi. *A study of delay differential equations with applications to machine tool vibrations*. PhD thesis, Ph. D. Thesis, Indian Institute of Science, Bangalore, 2005.

[97] Alan Wolf et al. Quantifying chaos with lyapunov exponents.

[98] Marek Balcerzak, Danylo Pikunov, and Artur Dabrowski. The fastest, simplified method of lyapunov exponents spectrum estimation for continuous-time dynamical systems. *Nonlinear Dynamics*, 94(4):3053–3065, 2018.

[99] Thomas S Parker and Leon Chua. *Practical numerical algorithms for chaotic systems*. Springer Science & Business Media, 2012.

[100] RG Dong, TW McDowell, DE Welcome, C Warren, and AW Schopper. An evaluation of the standardized chipping hammer test specified in iso 8662-2. *Annals of occupational hygiene*, 48(1):39–49, 2004.

[101] Ren G Dong, Daniel E Welcome, Xueyan Xu, Qingsong Chen, Hansheng Lin, Thomas W McDowell, and John Z Wu. A model for simulating vibration responses of grinding machine-workpiece-hand-arm systems. *Journal of Sound and Vibration*, 431:276–294, 2018.

[102] Xiaoai Jiang, D Michael McFarland, Lawrence A Bergman, and Alexander F Vakakis. Steady state passive nonlinear energy pumping in coupled oscillators: theoretical and experimental results. *Nonlinear Dynamics*, 33(1):87–102, 2003.

[103] M Wiercigroch, RD Neilson, and MA Player. Material removal rate prediction for ultrasonic drilling of hard materials using an impact oscillator approach. *Physics Letters A*, 259(2):91–96, 1999.

[104] Marian Wiercigroch, J Wojewoda, and AM Krivtsov. Dynamics of ultrasonic percussive drilling of hard rocks. *Journal of Sound and Vibration*, 280(3-5):739–757, 2005.

[105] Remco I Leine, DH Van Campen, and BL Van de Vrande. Bifurcations in nonlinear discontinuous systems. *Nonlinear dynamics*, 23:105–164, 2000.

[106] Aleksei Fedorovich Filippov. *Differential equations with discontinuous righthand sides: control systems*, volume 18. Springer Science & Business Media, 2013.

[107] Remco I Leine and Henk Nijmeijer. *Dynamics and bifurcations of non-smooth mechanical systems*, volume 18. Springer Science & Business Media, 2013.

[108] Samir Adly and Daniel Goeleven. A nonsmooth approach for the modelling of a mechanical rotary drilling system with friction. *Evolution Equations and Control Theory*, 10, 2020.

[109] Maolin Liao, Yang Liu, Joseph Páez Chávez, Antonio SE Chong, and Marian Wiercigroch. Dynamics of vibro-impact drilling with linear and nonlinear rock models. *International Journal of Mechanical Sciences*, 146:200–210, 2018.

[110] Oreoluwa Alabi, SunitKumar Gupta, and Oumar R Barry. Hand vibration reduction using nonlinear vibration absorber for the vibro-impact hammer model. *Journal of Computational and Nonlinear Dynamics*, 19(7):071005, 2024.

[111] Bappaditya Banerjee, Anil K Bajaj, and Patricia Davies. Resonant dynamics of an autoparametric system: a study using higher-order averaging. *International Journal of Non-Linear Mechanics*, 31(1):21–39, 1996.

[112] Mario Bernardo, Chris Budd, Alan Richard Champneys, and Piotr Kowalczyk. *Piecewise-smooth dynamical systems: theory and applications*, volume 163. Springer Science & Business Media, 2008.

[113] Anindita Ganguli and Soumitro Banerjee. Dangerous bifurcation at border collision: When does it occur? *Physical Review E—Statistical, Nonlinear, and Soft Matter Physics*, 71(5):057202, 2005.

[114] Yue Ma, Manish Agarwal, and Soumitro Banerjee. Border collision bifurcations in a soft impact system. *Physics Letters A*, 354(4):281–287, 2006.

[115] Shan Yin, Jinchen Ji, Shuning Deng, and Guilin Wen. Degenerate grazing bifurcations in a three-degree-of-freedom impact oscillator. *Nonlinear Dynamics*, 97:525–539, 2019.

[116] Arne B Nordmark. Non-periodic motion caused by grazing incidence in an impact oscillator. *Journal of Sound and Vibration*, 145(2):279–297, 1991.

[117] Harry Dankowicz and Mark R Paul. Discontinuity-induced bifurcations in systems with hysteretic force interactions. 2009.

[118] Shuiqing Hu and Arvind Raman. Chaos in atomic force microscopy. *Physical Review Letters*, 96(3):036107, 2006.

[119] M Wiercigroch. Modelling of dynamical systems with motion dependent discontinuities. *Chaos, Solitons & Fractals*, 11(15):2429–2442, 2000.

[120] Marcelo Amorim Savi, Sandor Divenyi, Luiz Fernando Penna Franca, and Hans Ingo Weber. Numerical and experimental investigations of the nonlinear dynamics and chaos in non-smooth systems. *Journal of Sound and Vibration*, 301(1-2):59–73, 2007.

[121] Hinko Wolf, J Kodvanj, and S Bjelovučić-Kopilović. Effect of smoothing piecewise-linear oscillators on their stability predictions. *Journal of sound and vibration*, 270(4-5):917–932, 2004.

[122] Zhi Zhang, Joseph Páez Chávez, Jan Sieber, and Yang Liu. Controlling grazing-induced multistability in a piecewise-smooth impacting system via the time-delayed feedback control. *Nonlinear Dynamics*, 107(2):1595–1610, 2022.

[123] Joseph Páez Chávez, Zhi Zhang, and Yang Liu. A numerical approach for the bifurcation analysis of nonsmooth delay equations. *Communications in Nonlinear Science and Numerical Simulation*, 83:105095, 2020.

[124] Harry Dankowicz and Frank Schilder. *Recipes for continuation.* SIAM, 2013.

[125] Mohammad Reza Monazzam, Ali Khavanin, Omid Sarrafzadeh, Mahbobeh Parsaeian, and Keykāvus Azrah. Handle transmitted vibration of electrical demolition hammers: Frequency and magnitude investigation in field measurements from different bits. *Journal of Low Frequency Noise, Vibration and Active Control*, 42(4):1880–1899, 2023.